INAUGURAL - DISSERTATION

zur
Erlangung der Doktorwürde
der
Naturwissenschaftlich-Mathematischen
Gesamtfakultät
der
Ruprecht-Karls-Universität
Heidelberg

vorgelegt von

M. Sc. Benjamin Flottmann

aus Bielefeld

Tag der Disputation: 17. Juli 2014

Implementation of Multi-Color Super-Resolution Microscopy into a High-Throughput Platform for Quantitative Imaging of Cellular Structures

Gutachter: Prof. Dr. Andriy Mokhir
Apl. Prof. Dr. Dirk-Peter Herten

Summary

In this work, single-molecule super-resolution microscopy with photoswitchable fluorophores was integrated into a multi-component microscopy platform. This platform enabled combined high-throughput widefield/confocal microscopy, in order to first validate relevant target cells, and subsequent sub-diffractional imaging of selected cells via direct stochastic optical reconstruction microscopy (*d*STORM). In a first project, a single-molecule sensitive fluorescence microscope was set up, and equipped for single-molecule localization microscopy. As suitable photoswitchable fluorophores for dual-colour imaging, Alexa Fluor 647/ Cy5 and Alexa Fluor 532 were identified. Software solutions were developed to analyze the raw data of a localization-based experiment and to reconstruct super-resolution images. Strategies to correct for chromatic aberration between two spectrally separate channels were developed by using fiducial markers and a registration software. The achieved localization precision was determined to be $\sigma_{\mathrm{SMLM}} = 12.5\,\mathrm{nm}$ in the image plane. The chromatic aberration could be corrected with a precision of 10 nm.

In order to integrate the super-resolution imaging into the microscopy platform, a workflow was developed that allowed transferring the sample between different microscope setups and relocating identified targets into the field of view. This procedure is based either on external reference markers on the respective cellarray/coverslip, or builds on using a stitched overview image with low resolution. Individual cells were relocated into the field of view with a precision of less than 4 µm.

For validation, widefield low-resolution images of a cis- and a trans-Golgi marker (GalT and Gm130) in cells were recorded and served to select individual cells for further analysis by confocal and super-resolution imaging. Images of representative control cells as well as cells treated with nocodazol (depolymerizes tubul network) and brefeldin A (relocates Golgi into the endosplasmic reticulum (ER)) were analyzed for colocalization using intensity-based colocalization analysis (ICA). The results indicated that nocodazol treatment fragmentizes the Golgi complex by the depolymerization of the tubul network. Contrarily, brefeldin A leads to a relocalization of the Golgi into the ER. The colocalization of GalT and GM130, calculated from confocal images, decreased from 9.6% (control cells) over 7.7% (nocodazol treatment) to 5.5% (brefeldin A treatment). This observation is in accordance with reports in the literature. The same decrease of colocalization was calculated from the super-resolution images (5.5%, 4.2% and 1.6% respectively).

Next to conventional colocalization analysis, single-molecule localization microscopy data can directly be analyzed using the coordinates of individual fluorophores (coordinate-based colocalization (CBC)). This analysis showed that after treatment with nocodazole, the colocalization of GalT and GM130 was not affected compared to the control cell. The Golgi complex disassembled into smaller structures, but the internal membrane structure remained intact. The treatment with brefeldin A degraded the whole Golgi and membrane assembly and therefore changed the colocalization pattern of the cis- and trans-Golgi marker.

In a second project, newly developed and sequence-specific oligonucleotide probes for messenger ribonulceic acid (mRNA) detection (synthesized in the group of professor *Mokhir*, Erlangen) were evaluated at the single-molecule level. This mRNA probe is synthesized to be intrinsically photoactivatable and specific due to a dual-strand design. The probe consists of a first oligonucleotide strand, which is conjugated to a fluorophore and linked to a quencher by a cleavable linker (-CHS=SHC-). The second oligonucleotide strand is conjugated to a photosensitizer, which upon irradiation with light catalytically produces singlet oxygen. Singlet oxygen cleaves the linker between the quencher and the fluorophore, releases the quencher and restores the fluorescence signal.

Single-molecule experiments were performed to validate the functioning of a probe that was designed to specifically bind actin-mRNA. Here, the fluorophore was conjugated to the first oligonucleotide strand by the cleavable linker. Illumination with light leads to the production of singlet oxygen, subsequent cleavage of the linker and release of the fluorophore.

The experiments showed that the cleavage reaction is highly specific and is not triggered if no activation light is applied, nor the strand of the photosensitizer includes a mismatching sequence to the target sequence. If the fluorophore was conjugated to the first oligonucleotide strand without a cleavable linker, the singlet oxygen for cleavage did not induce a release of the fluorophore.

Zusammenfassung

In dieser Arbeit wurde die direkte stochastisch-optische Rekonstruktionsmikroskopie (direct stochastic optical reconstruction microscopy (*d*STORM)) als höchstauflösende Mikroskopietechnik in eine Plattform aus Weitfeld und Konfokalmikroskop integriert. Die Plattform ermöglicht so ein kombiniertes Hochdurchsatzexperiment, mit dem zunächst Proteinverteilugen in relevanten Zellen durch eine schnelle Weitfeldaufnahme identifiziert werden. Diese Verteilungen können anschließend mit höherer Auflösung durch Konfokalmikroskopie und sogar auf molekularer Ebene mit *d*STORM visualisiert werden. In dieser Arbeit wird ein für diese Plattform entwickelter Arbeitsablauf beschrieben, um ein kombiniertes Hochdurchsatz-höchstauflösendes Experiment durchzuführen. Dabei liegt der Fokus auf der implementierten höchstauflösenden Mikroskopie und den Ergebnissen eines Validierungsexperiments, in dem die Verteilung und Kolokalisierung von zwei Proteinen des Golgi-Komplexes untersucht wurde.

Ein neues Lokalisierungsmikroskop wurde aufgebaut und die Farbstoffe Alexa Fluor 647/ Cy5 und Alexa Fluor 532 als ideales Paar für die Markierung von Proteinen in zwei Farben identifiziert. Algorithmen zur Analyse der Rohdaten von Lokalisationsexperimenten wurden entwickelt, um höchstaufgelöste Bilder zu rekonstruieren und zusätzlich die chromatischen Aberration zu korrigieren. Die mit dem neuen Mikroskop erreichten Lokalisationsgenauigkeiten liegen lateral bei $\sigma_{\mathrm{SMLM}} = 12.5\,\mathrm{nm}$, die Präzision in der Korrektur der chromatischen Aberration bei 10 nm.

Da die integrierte Mikroskopieplattform auf unterschiedlichen Mikroskopen realisiert wurde, wurde eine Routine für das Wiederfinden einzeln ausgewählter Zellen entwickelt. Dabei werden entweder extern hinzugefügte Marker auf dem Probenglas selbst, oder ein aus einzelnen Bildern mit geringer Auflösung zusammengefügtes Übersichtsbild als Referenz verwendet. Die Präzision der Relokalisierung von aufgewählten Zellen in das Gesichtsfeld der verwendeten Weitfeld- und konfokalen Mikroskopen liegt bei 4 µm.

Um die kombinierte Mikroskopieplattform zu evaluieren, wurde die Kolokalisierung eines cis- und eines trans-Golgiproteins (GalT und GM130) in Zellen unter verschiedenen Bedingungen mittels konfokaler und höchstauflösender Mikroskopie untersucht. Zu den Bedingungen zählten neben der Kontrolle die Zugabe von Nocodazol, welches das Tubulinnetzwerk depolymerisiert, sowie von Brefeldin A, durch welche der Golgi in das ER relokalisiert wird. Die intensitätsbasierende Kolokalisation (engl.: intensity-based colocalization analysis (ICA)) eines ausgewählten Bereichs ergab für die konfokalen Aufnahmen eine Abnahme der Kolokalisation von 9.6% (Kontrolle) über 7.7% (Nocodazol) zu 5.5% (Brefeldin A). Diese Ergebnisse entsprechen den in der Literatur beschriebenen Erwartungen. Die gleiche Reihenfolge in der Abnahme der Kolokalisation wurde für die selben Bereiche in den höchstauflösenden Daten beobachtet (5.5%, 4.2% und 1.6%). Die im Vergleich zu den konfokalen Daten geringeren Werte, können mit der höheren Auflösung der letzteren Technik erklärt werden: Strukturen, die in beugungsbegrenzten

Bildern zu kolokalisieren scheinen, können tatsächlich über 100 nm voneinander entfernt liegen.
Die Lokalisationsdaten der höchstauflösenden Mikroskopie können zusätzlich mit der koordinatenbasierten Kolokalisation (engl.: coordinate-based colocalization (CBC)) direkt ausgewertet werden. Im Vergleich zu ICA wurden im Fall der Zugabe von Nocodazol jedoch keine Veränderung in der Kolokalisation beobachtet. Obwohl Nocodazol den Golgikomplex fragmentiert, führt es demnach zu keiner Perturbation des Membrannetzwerks. Durch die Zugabe von Brefeldin A wurde der gesamte Golgikomplex und die damit verbundene Membranverteilung degradiert, was durch in einer Veränderung in den Kolokalisationsdaten erkennbar wurde.

Diese Arbeit behandelt weiterhin die Einzelmolekülexperimente zur Evaluation einer neuen mRNA-Sonde (synthetisiert in der Gruppe von Professor *Mokhir*, Erlangen). Die Sonde wurde so entworfen, dass sie intrinsisch photoaktivierbar und durch ihre zwei Sondenstränge spezifisch ist. In der entgültigen Version ist ein Strang chemisch an einen Fluorophor gebunden, welcher an einen abspaltbaren Quencher verknüpft ist. Die Spaltstelle ist hierbei eine (-CHS=SHC-) Gruppe. Der zweite Strang enthält einen Metallkomplex, welcher durch Photoaktivierung katalytisch Singulettsauerstoff produziert. Der Singulettsauerstoff spaltet die Verbindung zwischen Fluorophor und Quencher.
Mit den Einzelmolekülexperimenten konnte der Spaltmechanismus an einer vereinfachten Form der Sonde auf Einzelmolekülebene bestätigt werden. Bei der vereinfachten Form wurde nur der erste Strang verändert, sodass der Fluorophor durch Singulettsauerstoff vom Sondenstrang abgespalten wurde, die Sonde ist sequenzspezifisch gegen Actin-mRNA.
Die Experimente ergaben, dass die Abspaltung durch Singulettsauerstoff hochspezifisch ist und nicht spontan ohne Photoaktivierung eintritt. Desweiteren ist die Sonde sequenzspezifisch für eine einzige Mutation im Zielstrang der Sonde. Es konnte ebenfalls gezeigt werden, dass der katalytisch generierte Singulettsauerstoff zu keiner permanenten Photobleichung des Fluorophores führt.

Contents

1 Introduction

Most biological processes occur in confined compartments of a cell, which may vary between different cell types. The visualization and localization of these processes is essential to understand the life of a cell. Fluorescence microscopy is a powerful tool to investigate complex cellular processes of a biological sample in a non-invasive way. Virtually any target protein or substance within a cell can be labelled with a fluorophore and the position can be determined with high spatiotemporal resolution to explore protein-protein interactions or steady-state protein dynamics[1][2].

Image-based analysis of cells can be carried out in various ways. In a very basic approach the total cellular fluorescence intensity of antibody-labelled proteins or fusion protein constructs is determined. This has been done for example to investigate the virus entry into cells[3][4] or lipoprotein uptake[5]. Fluorescence morphology features are used to analyze cell division phenotypes[6] or cell cycle progression[7]. Modified versions of fluorescent proteins like split-GFP and its variants can be used to visualize protein-protein interactions[8].

In the recent past, automated widefield and confocal microscopes and robotic devices for sample preparation were developed and allow large scale fluorescence imaging on a screening microscopy platform[9]. For instance, a robot prepares a microwell cell array for parallel transfection of mammalian cells by printing a mixture of small interfering ribonucleic acid (siRNA), transfection reagent and a gelatine solution on defined spots on the array[10][11]. These arrays are dried and can be stored as 'ready-to-use' for several months. Plated cells are fixed after a defined time and imaged on an automated microscopy platform. The data is then analyzed for the up- and down-regulation of the targeted genes. These automated screening can be performed even to analyze a whole genome RNAi assay (MitoCheck[12]).

These kinds of microscopy platforms to record high-content data are usually workstations, that perform a programmed workflow. For instance, a low-resolution image is recorded and a number of randomly selected cells are imaged with higher resolution. As a result, large numbers of data accumulate, which might be of low quality as only a fraction of images shows the phenotypes. Additionally, not all images show cells with phenotypes: artefacts produced by for example dirt can interfere with routines for image analysis. Out-of-focus images cannot be analyzed either. With a rigid work-flow, the acquisition and storage of these unprofitable images happens, which can slow down follow-up processes like phenotype recognition and target identification for further analysis. Therefore, algorithms like *Micropilot*[13] or *KNIME*[14] were developed to directly validate the recorded data and in case of a positive hit, launch follow-up data acquisition by the microscope. This procedure accelerates the total imaging routine, as only validated targets are recorded. In addition, data containing artefacts or non-phenotypic cells are not kept.

Classification of cells into phenotypes is based on features such as brightness, size, and homogeneity or edge information. New approaches for automated classification were developed and can be realized by supervised machine-learning algorithms[15][16][6][17]. This machine-assisted classification can outperform the manual assignation[18].

Although being very powerful, common fluorescence microscopy is still limited by diffraction to a resolution down to 200 nm. A revolution in sub-diffraction fluorescence microscopy of the last years has evolved a new class of techniques which enable the acquisition of protein distributions within cells at the near-molecular level. This new kind of data is of special interest in systems biology, as complex processes can be analyzed and described on a more detailed level than before.

One of the first methods to record images below the diffraction limit was stimulated emission depletion (STED) in 1994[19], which is a point scanning technique. In addition to a standard confocal microscope, a donut-shaped depletion laser is overlaid on the excitation laser. Stimulated depletion of photons in the excitation volume of the depletion laser leads to a diffraction limited spot in the center of the donut beam, where fluorescence occurs. The resolution-limit in biological samples is reported to be at 30 nm[20].

In 2006 photoactivated localization microscopy (PALM)[21] and stochastic optical reconstruction microscopy (STORM)[22] were presented, which both rely on the localization of individually photoswitching fluorophores recorded in a widefield image series (fluorescent proteins in PALM; activator-reporter pair of organic fluorophores in STORM). Two years later direct STORM[23] was evolved from STORM, the lateral resolution was reported to be at 10-20 nm in biological samples. *d*STORM is the technique, used in this work.

Despite their sub-diffraction resolution, super-resolution microscopy techniques based on the localization of single molecules show limited performance in terms of throughput due to a limited field of view and relatively long image acquisition times.

So far, there is no solution to implement sub-diffraction microscopy into screening microscopy platforms, or to increase the throughput of localization-based microscopy techniques. The aim of this work is to develop a (semi-) automated microscopy platform, which combines low-resolution widefield screening, high-resolution confocal and super-resolution localization-based microscopy. This platform is highly modular, so that automated image acquisition and processing can be incorporated and that different microscopy techniques are combined to gain the maximum information from a sample.

The visualization of the distribution of mRNA is quite challenging, but essential to understand the life-cycle of a cell. mRNAs are transcribed from deoxyribonuleic acid (DNA) in the cell nucleus and transported to the place, where they are translated into proteins. Processes like cell division are dependent on the up- and down-regulation of protein levels during the different phases of the cell cycle. The regulation is affected by the amount of protein synthesis and the number of mRNA present within a cell.

Many approaches to label and visualize mRNAs in cells are available. A common way is to use small oligodeoxyribonucleotides (ODN) which are chemically bound to a dye (fluorescence *in-situ* hybridization (FISH))[24][25]. Molecular beacons are ODNs with a loop, where one end is labelled with the fluorophore, the other is chemically bound to a quencher[26]. Only in the open form, which is expected to be present after the hybridization to the target sequence, this probe exhibits fluorescence.

Still, there is no internal evidence for the amount of unspecific labelling during a certain experiment, which might vary from experiment to experiment and from cell to cell. High specificity of the probe is crucial in super-resolution microscopy, which relies on the distribution on detected fluorophores.

Spectral bar-coding of mRNA by the hybridization of a unique combination of ODNs, where each ODN is labelled with another dye, allowed a strategy for an internal proof of specificity[27]. However, this technique necessitates the linearization of mRNA for the identification of the barcode itself, and the usage of at least three dyes for distinct differentiation shrinks the number of dyes available to label other structures.

In this work, a new probe is introduced, which designed to be highly specific due to its double-strand approach, intrinsically photoactivatable, and in addition, does not need any special buffer conditions for super-resolution imaging.

2 Theory

Within this chapter the fundamental basics of fluorescence microscopy are presented. In the beginning, a short summary on absorption and fluorescence is given in addition to important processes associated with this. An introduction into the function and development of early microscope techniques to the state of the art is given, followed by a section on fluorescence reporters and their photochemical properties required for single-molecule localization microscopy.

2.1 Absorption and Fluorescence

This work employs fluorescence microscopy. The underlying physical processes are absorption and fluorescence and will be introduced in the following chapter [28]. Subsequent, a short history of fluorescence microscopy is given.

2.1.1 Absorption

By absorption of a photon, an atom or a molecule can be promoted from its electronical ground state S_0 to its first excited state S_1. Hereby, an electron gets promoted from the highest occupied molecular orbital (HOMO) to the lowest unoccupied molecular orbital (LUMO), or higher. The energy of the absorbed photon must match the energy difference ΔE between the two electronic states. ΔE can be calculated by *Planck's equation* (formula 2.1), where h stands for the *Planck* constant, c for the speed of light, ν for the frequency and λ for the wavelength of the photon.

$$\Delta E = E_{\mathrm{S}_1} - E_{\mathrm{S}_0} = h\nu = \frac{h\mathrm{c}}{\lambda} \tag{2.1}$$

Typically the energy for an electronic transition lies in the range of 1-10 eV. Photons with this energy are in the ultra violet (UV) and visible spectrum of light. In atoms,

only electronic transitions are possible, the absorption spectrum is a line spectrum. Molecules show a broad spectrum as they also have vibrational and rotational transitions. The energies of these transitions are in the range of 0.1 - 0.5 eV and 10^{-3} eV, respectively.
The occupation of the individual states can by calculated with the *Boltzmann distribution* as given in equation 2.2.

$$\frac{N_1}{N_0} = \mathrm{e}^{-\Delta E/k_B T} \tag{2.2}$$

Here, N_0 and N_1 represent the number of molecules in the S_0 and S_1 states, k_B is the Boltzmann constant and T is the temperature. At room temperature, $k_b \cdot T$ is 0.025 eV. At this temperature, a green-light absorbing dye ($\lambda_{\text{abs}} = 532\,\text{nm}$; $\Delta E = 2.3\,\text{eV}$) has a ratio of $N_1/N_0 = 4 \cdot 10^{-44}$.

Promotion of an electron from the ground to an excited state occurs within femto seconds, and is thus faster than the movement of the nuclei (*Born-Oppenheimer* approximation). The transition also occurs into an orbital with the largest overlap of the two involved wave functions (*Frank-Condon* principle). Transitions are termed vertical and occur into a higher vibrational level of the excited state S_1. Similar considerations are valid for the system relaxing back into the ground state (figure 2.1).

When light of a certain wavelength λ passes an absorbing specimen, the initial intensity I_0 will drop to a lower value I. The decrease is proportional to the travelled distance d and the concentration c of the absorbing specimen and its specific extinction coefficient ϵ_λ. This is quantitatively described by *Lambert-Beer*'s law (equation 2.3).

$$A = -\lg\left(\frac{I}{I_0}\right) = \epsilon_\lambda \cdot c \cdot d \tag{2.3}$$

2.1.2 Fluorescence

A chromophore is a molecule, that is capable to absorb a photon. A lumophore is a chromophore, which emits a photon when relaxing from the excited to the ground state. Depending on the property of the excited state, the luminescence is defined as either fluorescence or phosphorescence. The difference between these two can be explained by the *Jabłoński* diagram (figure 2.1). Here, S_0 and S_1 are the electronic ground and first excited state. T_1 represent the first triplet state. The different vibrational states are denoted with v, v' and v''. All states were ordered along the y-axis according to their respective energy.

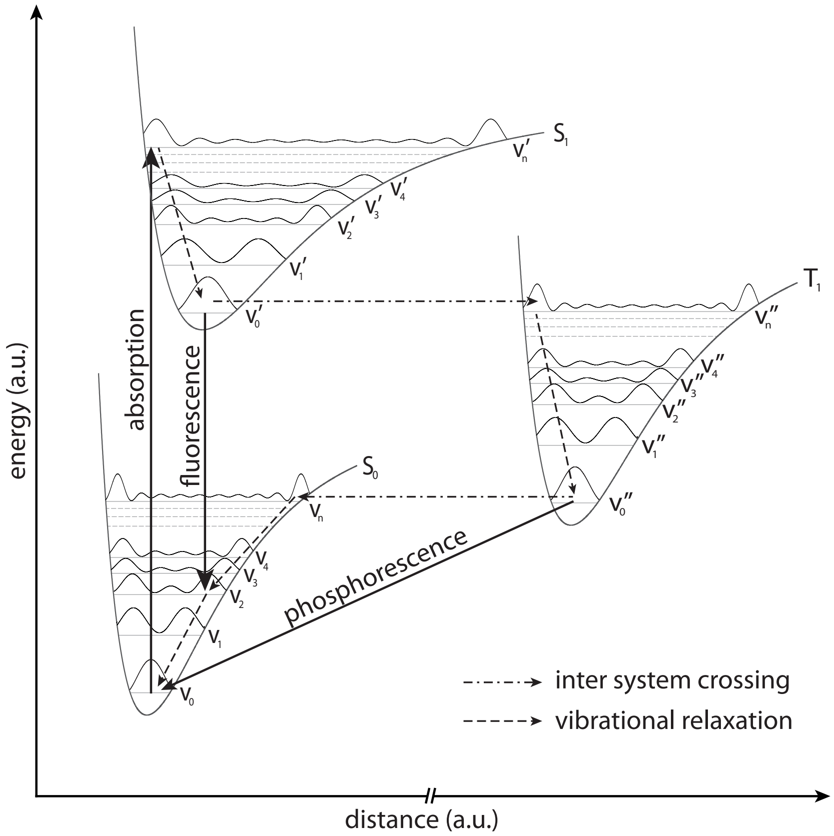

Figure 2.1: *Jabłoński* diagram. Some relevant transitions between different energetic states of a molecule are shown exemplarily. The *Franck-Condon* principle states that the most likely transition occurs from one level into another level with the highest overlap in the probability density. Following the *Born-Oppenheimer* approximation, the movement of an electron is faster by magnitudes than the movement of the nucleus so that the nucleus-nucleus distance does not change during transitions between S_0 and S_1.

Absorption into a higher vibrational level of the excitated state S_n takes place within femto seconds. Within 10 fs to 100 ps the system will relax from higher S_n states to the S_1 state via internal conversion (IC). Processes like solvent relaxation will promote a transition into the vibrational ground state of S_1 at a timescale of 1 - 100 ps. From this meta-stable state, slower processes like inter-system crossing (ISC) or fluorescence occurs. The fluorescence lifetime is the time between absorption and the emission of a photon, which will be explained in more detail later.

From S_1 the electrons can recombine in radiative and non-radiative processes. Recombination by emitting a photon from S_1 is called fluorescence and occurs according to *Frank-Condon* and *Born-Oppenheimer* into a higher vibrational state of S_0 at a timescale of 1 -100 ns. From there, the molecule relaxes to the lowest vibrational state of the ground state, with the energy being transferred to the solvent. Because of this, absorption and emission energies are shifted. The fluorescence spectrum is red shifted (*Stokes-Shift*, see figure 2.2) and mirrored in comparison to the absorption spectrum. However, the major contribution for the *Stokes-shift* is solvent relaxation, which is not explained here in detail[28].

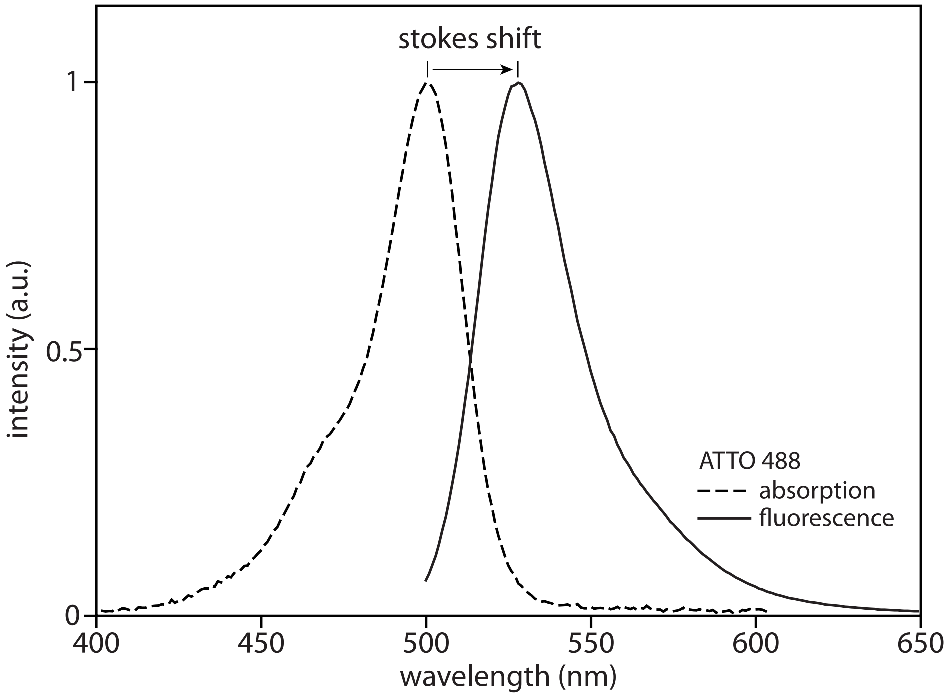

Figure 2.2: *Stokes-Shift.* The difference between absorption and emission maxima is shown here for the dye ATTO488 in PBS at pH 7.4.

If the system undergoes ISC, the spin of the electron is flipped and enters in the T_1 state (100 ps - 10 ns). The relaxation from T_1 to S_0 is forbidden by quantum mechanics and therefore a rather slow process (1 ms - 1 h). If a photon is emitted during this transmission, the process is called phosphorescence. If no more information is available, this process cannot be separated from fluorescence spectrally. Though, in comparison to the fluorescence spectrum, the phosphorescence spectrum is red shifted. Non-radiative relaxation processes from the S_1 state that reduce the rate of photon emission, are called fluorescence quenching.

The time-scales of all described processes are summarized in table 2.1[28][29].

Table 2.1: Tabel of typical time-scales of various transitions shown in figure 2.1[29].

transition	Typical Timescale
Absorption	$\sim 1\,\mathrm{fs}$
Internal Conversion	10 fs - 100 ps
Vibrational Relaxation	1 ps - 100 ps
Fluorescence	1 ns - 100 ns
Intersystem Crossing	100 ps - 10 ns
Phosphorescence	1 ms - 1 h

2.1.3 Quantum Yield and Fluorescence Lifetime

The fluorscence quantum yield Q quantifies the fraction of the number of photons which were emitted to the number of photons which were absorbed. It depends on the photon emission rate k_F and the radiationless decay rate k_nr and can be calculated by equation 2.4.

$$Q = \frac{k_\mathrm{F}}{k_\mathrm{F} + k_\mathrm{nr}} \tag{2.4}$$

The quantum yield spans values between 0 and 1. Dyes with a quantum yield of 0 show no fluorescence (nonradiative processes are predominant). If for all absorbed photons, a fluorescence photon is emitted, the quantum yield has a value of 1[28].

In the literature, the term of relative brightness ϕ is frequently used, which is a product of the extinction coefficient and the quantum yield (equation 2.5). The higher ϕ is, the more photons can be observed for fluorophores under comparable illumination conditions.

$$\phi = Q \cdot \epsilon_\lambda \tag{2.5}$$

The fluorescence lifetime τ_0 is the average time a fluorophore stays in the excited state and is given by equation 2.6.

$$\tau_0 = \frac{1}{k_\mathrm{F} + k_\mathrm{nr}} \tag{2.6}$$

The fluorescence lifetime τ_0 in absence of non-radiative processes k_nr is called natural fluorescence lifetime τ_n (equation 2.7).

$$\tau_n = \frac{1}{k_\mathrm{F}} \tag{2.7}$$

The natural lifetime τ_n can be calculated from τ and Q by equation 2.8.[28]

$$\tau_n = \frac{\tau_0}{Q} \tag{2.8}$$

2.1.4 Fluorescence Quenching

Fluorescence quenching includes all processes which lead to a decrease of fluorescence intensity. These processes are divided into two categories, dynamic and static quenching[28].

Dynamic quenching Dynamic quenching or collisional quenching occurs if a fluorophore collides with a second molecule, and its excited state is depopulated. The intensity of fluorescence depends on the concentration of excited fluorophores $[F^*]$ and the excitation rate $f(t)$. If $f(t)$ is constant, $d[F^*]/dt$ is 0. With the decay rate of fluorescence without quencher $\gamma = \tau_0^{-1}$ the change of $[F^*]$ is given as (equation 2.9):

$$\frac{d[F^*]}{dt} = f(t) - \gamma[F^*]_0 = 0 \tag{2.9}$$

In the presence of a quencher, an additional decay rate $k_q[Q]$ appears (equation 2.10).

$$\frac{d[F^*]}{dt} = f(t) - (\gamma + k_q[Q])\,[F^*]_0 = 0 \tag{2.10}$$

Solving equation 2.10 yields the *Stern-Volmer* equation[30]. The solution can be written in two ways, which are shown in equation 2.11 and equation 2.12.

$$\frac{F_0}{F} = \frac{\gamma + k_q[Q]}{\gamma} = 1 + k_q\tau_0[Q] \tag{2.11}$$

$$\frac{F}{F_0} = \frac{\gamma}{\gamma + k_q[Q]} = \frac{1}{1 + K_D[Q]} \tag{2.12}$$

Important to note is, that dynamic quenching leads to a decrease of the fluorescence life-time $\tau = (\gamma + k_q[Q])^{-1}$ as well as is the fluorescence intensity (equation 2.13).

$$\frac{F_0}{F} = \frac{\tau_0}{\tau} = 1 + k_q\tau_0[Q] \tag{2.13}$$

Static quenching Static quenching is usually based on the formation of a complex of a quencher Q and the fluorophore F. The complex FQ itself is not fluorescent. Therefore the ratio of F_0/F is only dependent on the association constant K_S of complex formation (equation 2.14).

$$K_S = \frac{[FQ]}{[F][Q]} \tag{2.14}$$

The total concentration of fluorophores given by $[F]_0 = [F] + [FQ]$. By the substitution of the concentration of a fluorophore $[F]$ with the fluorescence intensity F, equation 2.14 can be rewritten as (equation 2.15):

$$\frac{F_0}{F} = K_S[Q] \tag{2.15}$$

In a *Stern-Volmer* (F_0/F vs. $[Q]$) plot, F_0/F depends linearly on $[Q]$ for both dynamic and static quenching. To determine whether static or dynamic quenching occurs, fluorescence lifetime measurements in presence and absence of a quencher have to be made. If a change in fluorescence lifetime is observed, quenching occurs from dynamic quenching, otherwise from static quenching.

Combined Static and Dynamic Quenching In practise, often a combination of both, static and dynamic quenching is observed. In such circumstances the *Stern-Volmer* plot shows a curvature towards the y-axis. The modified *Stern-Volmer* equation for this case is second order in $[Q]$ and given by equation 2.16.

$$\frac{F_0}{F} = (1 + K_D[Q])\,(1 + K_S[Q]) \tag{2.16}$$

In figure 2.3 dynamic and static quenching mechanisms are outlined.

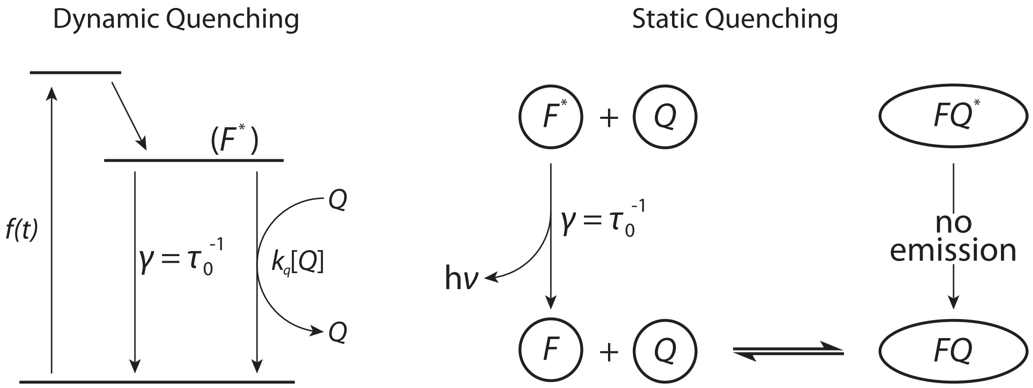

Figure 2.3: Two mechanisms of quenching are shown schematically. Dynamic quenching occurs when a quencher Q collides with a fluorophore F^* in its excited state and depopulates this state. In static quenching the quencher forms a complex with the fluorophore, which shows no fluorescence anymore. Only dynamic quenching affects the fluorescence lifetime τ_0. (Figure adopted from *Lakowicz*[28].)

2.2 Geometrical Optics

The basics of an optical microscope can be described by geometrical optics. A short introduction into geometrical optics is given in the following section[31].
A punctual light source P emits light in spherical waves. The *Poynting vector* gives the direction of light beams, which is the direction of energy flux. All light beams originating from P are divergent. In the ideal case, an infinite number of the emission beams can be collected by optical elements and focussed on a point Q. Without absorption, reflection or scattering, no energy is lost and Q is a perfect image of P. As optical systems are reversible, a punctual light source in Q has a perfect image in P. Therefore, P and Q are called conjugated. Each point of a three-dimensional object can be described as a punctual light source. Having a perfect optical system, the three-dimensional object in the object space creates a perfect image in the image space.
In a real optical system only a cone-shaped part of the spherical wave front of the emitted light is captured by optical systems, due to a limited opening angle of the optical components (figure 2.4).

Wavefronts do not travel linearly through interfaces of two homogenious media but are diffracted depending on the wavelength of the light. Instead of generating a punctual image of a punctual light source, the energy is blurred in a spot. However, geometrical optics is well suited to describe expansion of light beams in optical systems like a microscope. As long as objects are larger than the wavelength of light, errors can be neglected.

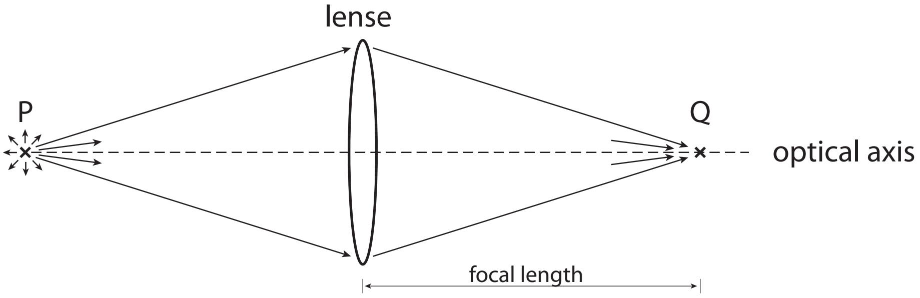

Figure 2.4: Geometrical optics. The puncutal light source P emits light in all directions. The lens collects a part of the emitted light beams and focuses them onto the point Q. This also works contrariwise for a punctual light source in Q being focussed onto P.

2.3 Microscopy Techniques

This section covers the principles of microscopy techniques and how they were developed over time. It will start with early light and fluorescence microscopy and end with the super-resolution microscopy techniques including direct stochastic optical reconstruction microscopy (*d*STORM)[23] and PALM[21].

2.3.1 Conventional Light and Fluorescence Microscopy

The human eye is able to resolve structures down to the micrometer range. To visualize smaller objects, optical systems like magnifying glasses and microscopes have been used. The basic principle of a microscope is shown in figure 2.5.

The specimen of interest is placed in the focal plane of the objective. Light beams originating from the sample (fluorescence) or transmitted through the sample (brightfield) are collected by the objective and focussed onto the image plane. The eye-piece (or ocular) then collects the light beams, and in combination with the lens in the eye the image is projected onto the retina. If a camera is used to record the image, it is commonly placed in the image plane of the microscope.

The described detection pathway is valid in general for light and fluorescence microscopes. In a transmission light microscope, the sample is illuminated by a bright light source from the opposite side of the objective. Light passing the sample is absorbed and/or scattered depending on the characteristics of the sample. The remaining light is then collected by the objective and projected to form the image. The sample is positioned in between the light source and the objective.

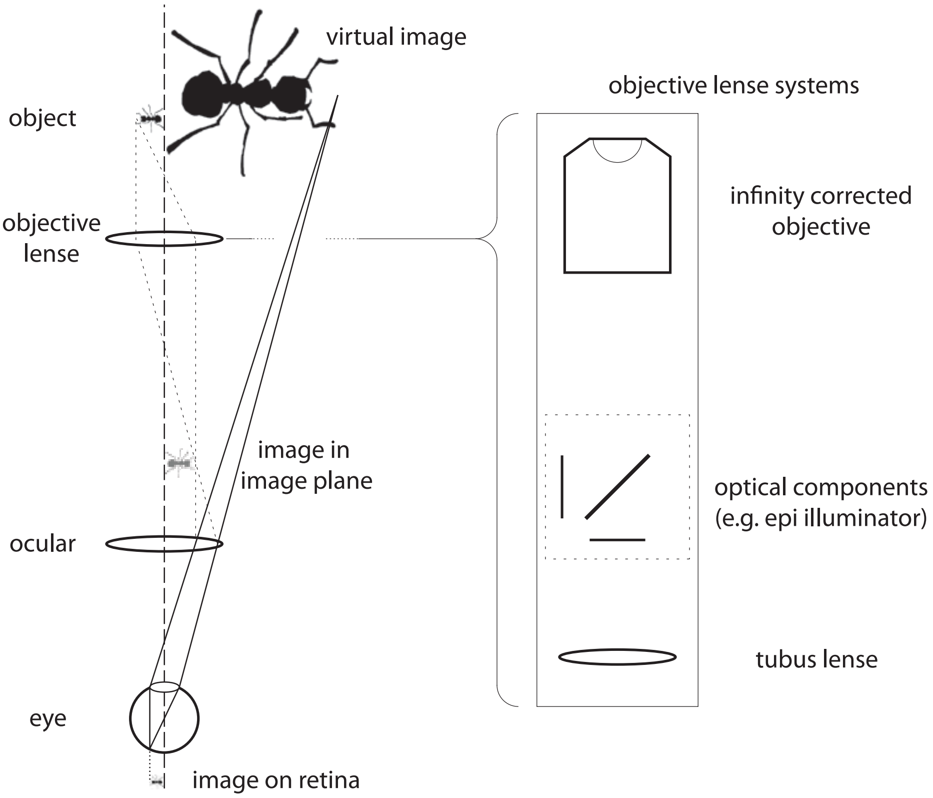

Figure 2.5: Scheme of a simple microscope. A small object is virtually enlarged by a system of two lenses - the objective lens and the eye piece. In modern microscopes the objective lens consists of an infinity corrected objective and a tube lens. Optical elements like filters can be placed in between the objective and tube lens without distorting the image.

2.3.2 Widefield Fluorescence Microscopy

In fluorescence microscopy, monochromatic light from a lamp or a laser is used to illuminate the sample. Fluorophores are tagged to target molecules, particles or molecules of interest. The fluorophores are excited and emit photons. The emitted light is then collected by the objective and focussed by the tube lens to generate the image. Compared to the emitted light, the intensity of excitation light is orders of magnitudes higher and severely decreases contrast because of high background. Emission filters are used within the detection pathway after the objective to filter out the excitation light. However, illuminating the sample from the same side as collecting the emitted light, is the simplest way to decrease background caused by excitation light; excitation and emission light has to pass the same objective. To separate excitation and emission light, more optical elements have to be placed into the light pathway. If objects like dichroic mirrors are directly placed anywhere between the objective and camera or eye piece of a setup, distortions of the image can occur. In modern fluorescence microscopes the objective as a single lens is replaced by a system consisting of an infinity-corrected objective and tube lens (figure 2.5). The infinity-corrected objective parallelizes the collected light beams and the tube lens then focuses the parallized beams onto the image plane. Dichroic mirrors and filters placed in the parallel light beam do not distort the image. The dichroic mirror is used to overlay the emission and excitation pathway, while it reflects the excitation light and emission light is transmitted. The combination of dichroic mirror, excitation and emission filter is also called epi-illuminator, the arrangement of excitation and emission pathway epi-illumination (figure 2.6).

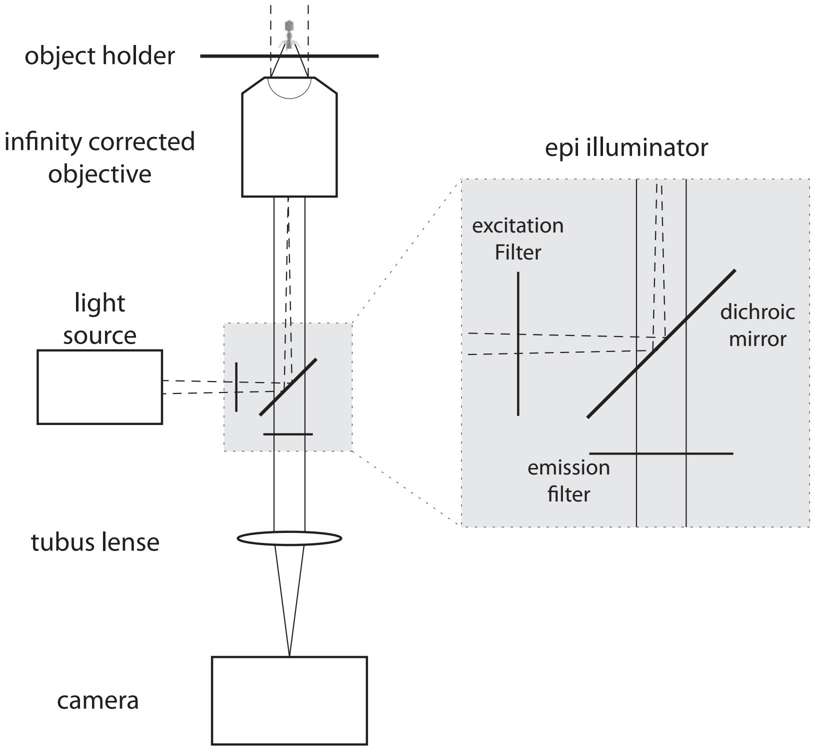

Figure 2.6: Widefield fluorescence microscope. The sample is illuminated by a light source. An epi-illuminator is placed between the infinity corrected objective and the tube lens and consists of three parts. The excitation filter transmits only excitation light and blocks any other light deriving from the light source. The dichroic mirror reflects excitation light and transmits emitted light - excitation and emission light are separated. The emission filter blocks any wavelength not being in the desired range of the fluorescence of the dye. The camera is placed into the image plane of the microscope (compare to figure 2.5).

Wide field fluorscence microscopy allows recording a whole field of view in one image. The illumination scheme is realized by focussing the excitation light onto the back focal plane of the objective so that parallel light exits the objective at the side of the sample. As for the illumination there is no restriction along the optical axis, the whole specimen is illuminated. Fluorophores which are not in the focal plane of the objective will also be excited and fluoresce, which will increase the background signal and reduce the contrast. A solution in some cases is total internal reflection (TIR), which is realized by coupling the excitation beam into the objective (by moving the beam to the outer rim of the objective lens system) with an angle of total reflection at the interface that induces an evanescent electromagnetic field. This field decays exponentionally with distance to the interface. Fluorophores will only be excited within 100 - 200 nm into the sample (TIR). Imaging of this area is not severely affected by background of fluorescence deeper into the specimen; the signal-to-noise ratio is higher (figure 2.7).
By moving the excitation beam into a position within the objective between TIR and epi-illumination ends in an about 4 µm thin inclined light sheet passing the sample within the field of view. This illumination scheme is also called higly inclined and laminated optical sheet (highly inclined and laminated optical sheet (HILO), figure 2.7)[32]. Compared to epi-illumination, the background is reduced due to less out-of-focus excitation and the signal intensity is enhanced due to higher excitation intensities (the excitation beam diameter reduced from about 60 µm in epi to about 4 µm in HILO illumination).

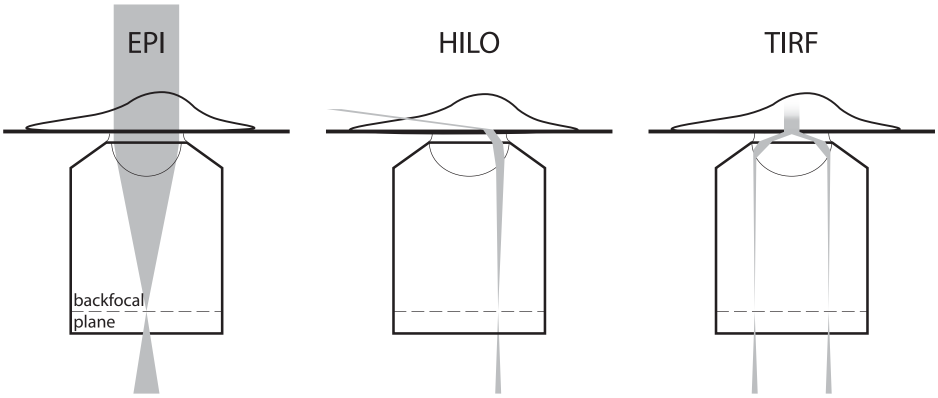

Figure 2.7: Illustration of epi, HILO and TIR illumination. In epi-illumination the whole specimen is illuminated by the excitation beam. Total internal reflection leads to a evanescent field, where the sample is illuminated within 100 - 200 nm at the specimen. A thin and inclined light sheet illuminates the sample in HILO excitation. The light sheet is achieved by moving the excitation beam to an angle close to total internal reflection[32].

2.3.3 Confocal Microscopy

In contrast to the homogeneous illumination of a specimen in widefield or TIRF microscopy, confocal microscopy is a point-scanning technique. The excitation light is focussed onto the sample. Within the excitation volume, fluorophores are excited and fluoresce. The fluorescence is captured by the objective and focussed onto an aperture to restrict detection only to the focal plane, as still some fluorophores within the illumination cone and outside of the focal volume can fluoresce. As the fluorescence originates from a single spot, a point detector is used. The passing light is detected by a photomultiplier tube (PMT) or avalanche photodiode (APD). The lateral and axial information come with the position of the focus, which can be scanned over the sample in three dimensions to reconstruct an image (figure 2.8).

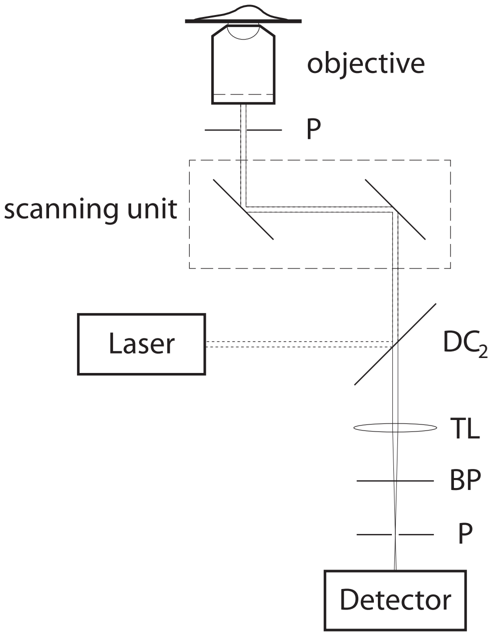

Figure 2.8: Schematic of a confocal microscope. The excitation laser is coupled into the objective and focused onto the sample. The scanning unit moves the focus through the sample. Fluorescence is collected by the objective, separated from the excitation beam by a dichroic mirror and focussed onto a detector (e.g. PMT). A pinhole P ensures that only fluorescence originating from the excitation volume passes onto the detector. Background light originating from above or below the focal plane is blocked.

Compared to widefield illumination, confocal microscopy shows a higher signal-to-noise ratio. Also, three-dimensional information of fluorophore distributions can be gathered using confocal microscopy. However, widefield microscopy is usually faster in recording a complete image of a specimen. Also fast movements can create artefacts during the scanning process of confocal microscopy, which will appear as distortions of the fast moving structure[33].

2.3.4 Resolution Limit

A fluorescent dye can be regarded as a punctual light source and generates a blurred spot on the camera detector and an image with an intensity distribution is generated. The intensity distribution described by a point-spread function (PSF). This phenomenon is caused by the diffraction of light. Within the focal plane, the intensity is described by the *Airy*-distribution(equation 2.17). The *Airy*-disc is the area between the maximum center of the distribution until the first minimum.

$$I\left(\nu\right) = \left(\pi N^2\right) \cdot \left[\frac{2J_1\left(\nu\right)}{\nu}\right]^2 \tag{2.17}$$

The *fresnel* number N and the radial optical coordinate $\nu(r)$ are given with equation 2.18 and equation 2.19 respectively, λ is the wavelength of light and J_1 is the *Bessel*-function of first order and first kind.

$$\nu\left(r\right) = \frac{2\pi \mathrm{NA}}{\lambda} \cdot r \tag{2.18}$$

$$\mathrm{N} = \frac{\left(\mathrm{NA}\right)^2}{f\lambda} \tag{2.19}$$

Hereby, f is the focal length and NA is the NA of the medium and can be calculated by equation 2.20 with the refractive index of the objective n and the half opening angle α.

$$\mathrm{NA} = n \cdot \mathrm{sin}\alpha \tag{2.20}$$

The refractive index reaches values of 1.0, 1.33 or 1.51 for air, water or oil, respectively. If two point objects are very close, their PSFs start to overlap. At smaller distance, the objects cannot be resolved with light microscopy, as their individual centers become indistinguishable. End of the 19's century *Ernst Abbe* and *Sir Rayleigh* described this phenomenon and discussed a resolution limit for optical microscopes[34][35][36]. *Sir Rayleigh* defined that two objects can be distinguished until the maximum of the *Airy* disc of one objects falls onto the first minimum of the *Airy* disc of the other object (figure 2.9).

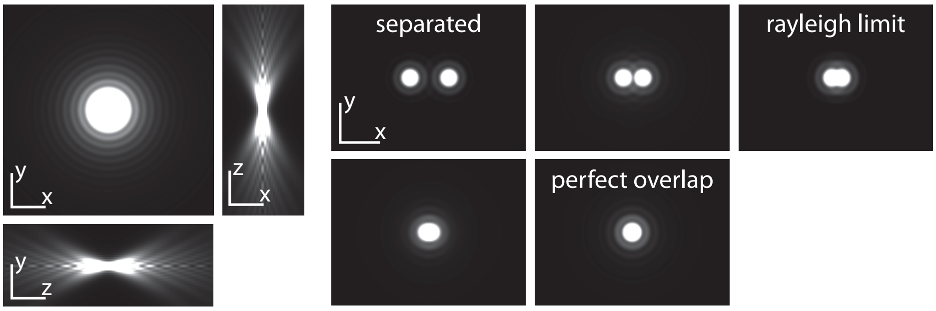

Figure 2.9: Point spread function. Due to diffraction, a punctual light source leads to a so called *Airy-distribution*. Following the *Rayleigh* criterion, two objects can be resolved until the first minimum of one *Airy* distribution hits the maximum of the other *Airy* distribution.

Depending on the objective's NA and the wavelength λ, the minimum distance d of these objects can be calculated by equation 2.21 (*Rayleigh* criterion).

$$d = 0.61 \frac{\lambda}{\mathrm{NA}} \tag{2.21}$$

Increasing the NA would result in a smaller distances, at which objects can still be resolved. The maximum opening angle α of an objective lens is physically limited to 73° and cannot easily be extended. However, instead of air with a refractive index of $n = 1$ using immersion oil with a refractive index close to that of the glass ($n = 1.515$) will increase the NA by about 47 %. Effectively the cone of collected light from the spherical light waves (chapter 2.2) is enlarged. When monochromic light of 568 nm is used to illuminate the structure of interest, the resolution limit is at 270 nm[36] (figure 2.10).

2.4 Advanced Fluorescence Microscopy Techniques

For many years, electron microscopy was the method of choice for imaging of (biological) targets below the optical diffraction limit[37]. However, it could not replace light microscopy entirely as labelling/identifying of specific targets is difficult and live cell experiments are impractical. Instead, a major part of microscopic questions has still

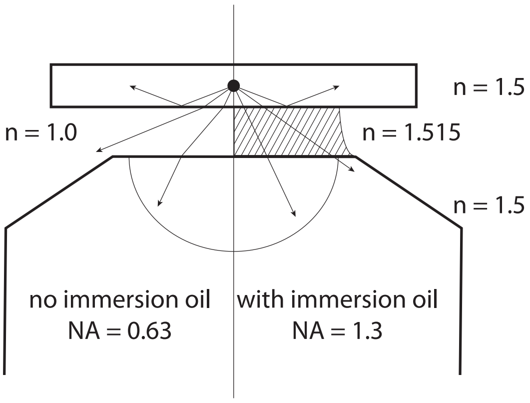

Figure 2.10: Increasing of the NA by use of immersion oil. The difference in refraction between air and glass causes a decrease in NA. Using immersion oil with a comparable refractive index to glass avoids index mismatch and therefore the decrease in NA.

been addressed with standard, diffraction-limited light microscopy[38]. Due to a rapid development in the field of single-molecule fluorescence and fluorescence microscopy within the last ten years, many techniques evolved that surpass the diffraction limit.

The diffraction limit only occurs for light which has propagated a significant larger distance than its wavelength. Using an excitation and detection tip with a size of a few nanometer in close proximity to an object, diffraction is only limited by the aperture of the tip. By scanning the surface with this tip, a resolution down to 20 nm can be achieved. This technique is called nearfield scanning optical microscopy (NSOM)[39]. A limit of this technique is that, like in related atomic force microscopy (AFM)[40], only the surface of objects can be imaged but not the inside of, for instance, intact cells.

The first super-resolution microscopy technique of its kind has been developed by *Stephan W. Hell* in 1994. The STED[38][41][19] is a confocal approach, in which a excitation laser excites fluorophores just as in a conventional microscope. A second laser at longer wavelengths is modified for instance by a phase plate to have a donut shape and it is overlaid to the excitation laser. After excitation by the first laser, the second laser causes stimulated emission of photons ("depletion") within the excited volume but only where the intensity is high enough. In the center, where the intensity of the depletion laser is zero due to its donut shape, no stimulated emission occurs. The resulting image has a resolution below the diffraction limit. Depending on the fluorophore and with the knowledge of the minimum of the depletion beam, images with a lateral resolution down to 30 nm in biological can be recorded[20].

In structured illumination microscopy (SIM)[42] from *Gustafsson et al.* in 2000 and saturated structured illumination microscopy (SSIM) (*Heintzmann et al.* in 2002[43]), the sample is illuminated with a series of translating and rotating light patterns so that moiré fringes appear. With a series of light images recorded with different orientations and phase patterns, an image can be reconstructed with a two-fold increase in resolution. Another group of techniques is based on single-molecule detection. Photoactivated localization microscopy (PALM)[21], fluorescence photoactivation localization microscopy (FPALM)[44], PALM with independently running acquisition (PALMIRA)[45], spectral precision distance microscopy (SPDM)[46], STORM[22], direct STORM (*d*STORM)[23] and ground state depletion followed by individual molecule return (GSDIM)[47] are all widefield approaches, where an image series of stochastically photoswitching fluorophores is recorded in widefield mode. The centers (localizations) of single fluorophores are then determined and listed in a file of coordinates. A super-resolved image is reconstructed from this coordinates.

Some improvements in conventional far-field microscopy can be adapted in the super-resolution microscopy. For instance, a general attempt to increase the resolution was to increase the NA. This was achieved by two opposing objectives with the sample in between (called 4PI for confocal[48][19][49] and I^{5}M for widefield[50]). The approach of two opposing objectives was realized as for example isoSTED[51] and dual-objective STORM[52]. For *d*STORM and PALM, a variety of optical configurations allow 3D imaging. This includes interference of beam paths[53], double-helical PSF[54], astigmatism[55] and biplane alignment[56].

Localization-based microscopy techniques mostly differ in the way of how photoswitching is induced. In this work, *d*STORM and PALM have been used and are described in more detail later (chapter 2.5.3).

2.5 Localization-based Super-Resolution Microscopy

As the super-resolution technique used within this work is based on single-molecule localization, the basic principles are introduced in the following section.

2.5.1 Theoretical Localization Precision

Two punctual light sources cannot be discerned, if they are closer than $\sim \frac{\lambda}{2}$ (chapter 2.3.4). However, the position of just one single point emitter can be determined with high precision[57][58]. The more photons N are recorded by the camera detector, the more the localization error Δx decreases. With the standard deviation s of the recorded PSF, Δx can be approximated by following equation 2.22.

$$\left\langle (\Delta x)^2 \right\rangle \approx \frac{s^2}{N} \tag{2.22}$$

The ideal case is described by equation 2.22, when no background or noise occurs during image acquisition. Considering the pixilation of the image with a pixel size of $a < s$ and additional background b, Δx is defined as described in equation 2.23[57].

$$\left\langle (\Delta x)^2 \right\rangle = \frac{s^2 + a^2/12}{N} + \frac{8\pi s^4 b^2}{a^2 N^2} \tag{2.23}$$

In a typical single-molecule super-resolution experiment, the localization precision is approximately 5-10 nm in the xy-plane. Two approaches to determine the center of a PSF are described in chapter 3.1.5.

Endesfelder et al. developed a simple method to estimate the average localization precision of a localization-based microscopy image using the nearest neighbor distances of localizations[59]. This approach was also used within this work to determine the localization precision. The assumption relies on fluorophores, which were localized in consecutive frames. Here, the experimental localization precision σ_SMLM is calculated based on the probability for a positional displacement $p\left(d\right)$ of a single molecule. It can be calculated by equation 2.24, where the distance d is calculated between a specific localization $\mathrm{loc}_i\left(r_i, t_i\right)$ in one image frame and its nearest neighbor localization $\mathrm{NN}_i\left(\mathrm{nn}_{r_i}, t_{i+1}\right)$ in the next imaging frame t_{i+1} $\left(d = \mathrm{loc}_i\left(r_i, t_i\right) - \mathrm{NN}_i\left(\mathrm{nn}_{r_i}, t_{i+1}\right)\right)$, σ_SMLM is the standard *Gaussian* deviation characterizing the localization precision, and A_1, A_2 and A_3 are the amplitudes of each term. ω is the Gaussian standard deviation, which characterizes the short-range correction term centering at d_C.

$$p\left(d\right) = \mathrm{A}_1 \cdot \left(\frac{d}{2\sigma^2_\mathrm{SMLM}} \cdot e^{\frac{-d^2}{4\sigma^2_\mathrm{SMLM}}} \right) + \mathrm{A}_2 \cdot \left(\frac{1}{\sqrt{2\pi\omega^2}} \cdot e^{\frac{-d-d_c}{2\omega^2}} \right) + \mathrm{A}_3 \cdot d_\mathrm{c} \tag{2.24}$$

2.5.2 Fluorescence Reporters

A system of conjugated π electrons forms the backbone of every fluorescent (organic) molecule. Within this system, an electron of the highest occupied molecular orbital (HOMO) can be promoted to the lowest unoccupied molecular orbital (LUMO) by absorption of light. This electron can be described as a particle in the box. In polyenes, the energy E_n of this electron can be calculated as shown in equation 2.25[60].

$$E_\mathrm{n} = \frac{n^2 h^2}{8 m_\mathrm{e} L^2} \tag{2.25}$$

Here, n is the quantum number, h is the *Planck* constant, m_e is the mass of the electron and L is the length of the box, which corresponds to the length of the conjugated π electron system. The longest wavelength λ of the emitted/absorbed photon can be theoretically calculated for a molecule in the gas phase via the energy difference between two states using equation 2.26. Although this calculation is based on molecules in the gas phase, it can be seen as an approximation for dye molecules in solution.

$$\lambda = \frac{hc}{E_\mathrm{HOMO} - E_\mathrm{LUMO}} = \frac{8 m_\mathrm{e} L^2 c}{(N+1)\, h} \tag{2.26}$$

2.5.3 *d*STORM and PALM

The position of two fluorophores can be determined with nanometer precision, if they are separated well enough from the others (chapter 2.5.1). In cells, fluorophore-labelled proteins usually appear in distances below the diffraction limit and cannot be distinguished. By recording only a small fraction of all fluorophores, which are spatially separated to a distance larger than $\langle(\Delta x)\rangle$, these fluorophores' centers can be determined. Repeating this step with a further subset of fluorophores until all or the major part is detected will result in a localization table with information to reconstruct a super-resolved image. The key to realize this temporal separation of individual fluorophores is switching the fluorophores between an ON and an OFF state.

*d*STORM and PALM both use the procedure of switching dyes between ON and OFF states (chapter 2.5.2 and chapter 2.5.4), but differ in the type of fluorophores. Where for *d*STORM organic fluorophores are used (see chapter 2.5.2 and chapter 3.1.1), PALM makes use of photoswitchable fluorescent proteins.

3D-dSTORM by Astigmatism In 1994, *Kao* and *Verkman* showed a new approach for single particle tracking in 3D by using a cylindrical lens with a large focal length in the detection pathway of an epi-fluorescence microscope to induce asymmetry in to the PSF along the z-axis[61]. Based on this work, *Bo Huang et al.* demonstrated in 2008 the first 3D-STORM data on the microtubule network and clathrin-coated pits in a cell[55]. In figure 2.11, the principle of the detection of single molecules in 3D is demonstrated. Depending on the width in x and y of the PSF, a z-value can be assigned to the localization.

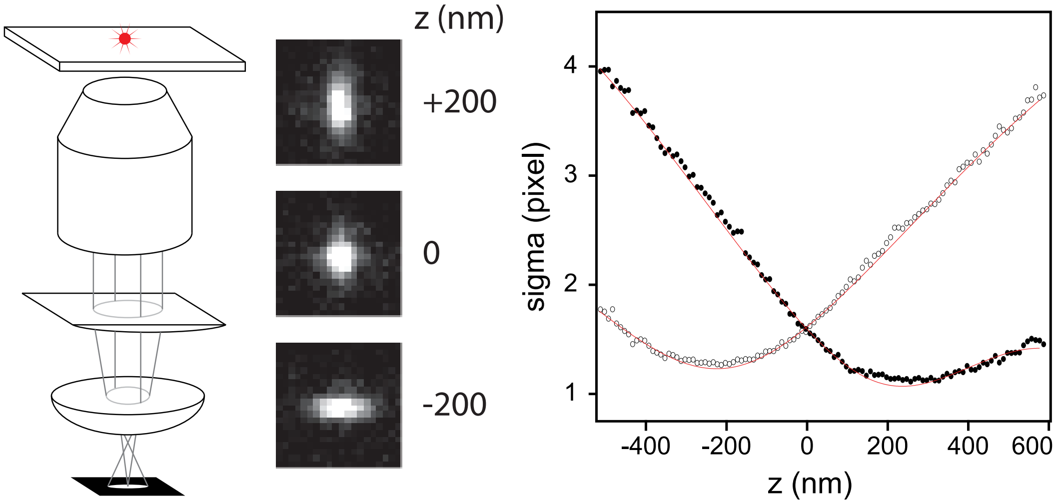

Figure 2.11: Principle of 3D-(d)STORM via astigmatism[55]. A cylindrical lens with a large focal length is placed between the objective and the image plane (at the left; here shown in the order of objective, cylindrical lens, tube lens, image plane). Due to the cylindrical lens, the focus along the x-axis (or y-axis, depending on the direction of the cylindrical lens) distorted, but remains the same in the other direction. As a consequence the PSF of a point emitter is distorted depending on the distance to the focal plane (middle). By plotting the width in x and y direction for various z-values, a calibration curve can be generated (right).

The width can be calculated with an elliptical *Gaussian* function (equation 2.27, where h is the peak height, b is the background, x_0 and y_0 is the center of the peak and w_x and w_y stands for the widths of the PSF in the x and y directions, respectively:

$$G\left(x,y\right) = h \cdot e^{\left(-2\frac{(x-x_0)^2}{w_x^2} - 2\frac{(y-y_0)^2}{w_y^2}\right)} + b \tag{2.27}$$

Organic Dyes

Organic dyes have an extended π-electron system and show bright fluorescence. Prominent classes of organic dyes are rhodamines, oxazines, carbocyanines and bora-diaza-indacenes (figure 2.12). These dyes have been designed for a high relative brightness and photostability and can be tagged to target molecules by a variety of coupling groups (e.g. iso-thio-cyanate, azide, N-hydroxysuccinimide). In their fluorescence emission wavelength, they cover the whole visible spectrum[62][63].

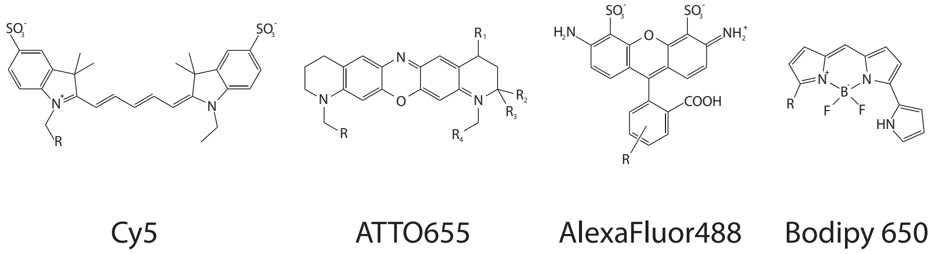

Figure 2.12: Organic dyes. Four examples of organic dyes, with Cy5 as a carbocyanine, ATTO655 as an oxazine, AlexaFluor488 as a rhodamine and Bodipy650 as bora-diazo-indacene.

To use organic dyes in super-resolution microscopy techniques like *d*STORM, they have to exhibit photoswitching behaviour, which is achieved by high illumination intensities and reducing buffer conditions. So far, potential photoswitching mechanisms have been reported for carbocyanines[64], rhodamines[65] and oxazines[66]. Common of all is the use of a switching buffer, which consist of millimolar concentrations of thiols like β-mercaptoethylamine (MEA) or β-mercaptoethanol (β-ME) in a phosphate buffer (PBS)[63][67]. In case of carbocyanines, oxygen removal is advised. As these dyes are known to photobleach more easily, oxygen removal extends the lifetime of the triplet state, which is supposed to be the reactive species to form the OFF state[68].

Carbocyanines have been shown to reversibly form an encounter complex with the thiol anion that forms an adduct, after excitation with red light. The formation of an adduct has been proven with mass spectrometry[64]. By irradiation with UV-light, the adduct will decompose and the carbocyanine is recovered.

Rhodamines and **oxazines**, however, are reduced by the thiol acting as a reducing agent (see figure 2.13). When the fluorophore enters the triplet state by ISC, it can either react with oxygen to repopulate the S_0 state, or react with the thiol to enter a non-fluorescent radical state. The radical state was shown by electron paramagnetic resonance (EPR) spectroscopy for rhodamines[65]. The absorption maximum of the radical state is blue shifted. By reaction with oxygen of illumination with blue light, the radical is oxidized to the S_0 state[65].

Oxazines are reduced twice into the leuco-form, as it has been shown by *Kottke et al.*[66] by infra-red spectroscopy and theoretical calculations. As for the rhodamines and carbocyanines, both oxidation and illumination with blue light triggers the recovery of the S_0 state from the OFF state.

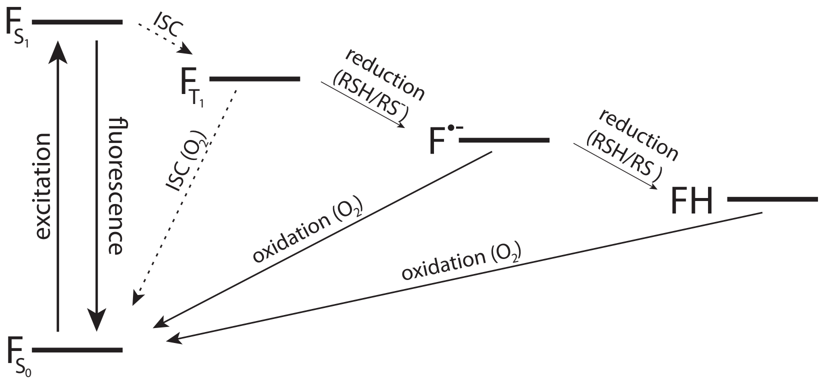

Figure 2.13: Reaction scheme for reversible photoswitching of organic dyes. The fluorophore F is excited from its ground state S_0 to the excited state S_1. By emitting a photon, it returns into the S_0 state. Via ISC, the system enters the triplet state T_1. By reaction with oxygen, the system relaxes back into the S_0 under formation of singlet oxygen. The reaction of T_1 with thiols leads to the radical ion form of the dye. This state has been confirmed for the rhodamine AlexaFluor488 by *van de Linde et al.*[65]. Oxazines are reduced twiced by thiols as shown in *Kottke et al.*[66]. The reaction of the reduced dyes with oxygen recovers the S_0 state of the fluorophore. (Figure adapted from *Endesfelder*[33].)

Fluorescent Proteins

The green fluorescent protein (GFP)[69] is an eleven-stranded β-barrel with one α-helix and has been found as the first fluorescent protein in the jelly fish *Aequora Victoria*[70][71] (figure 2.14). The chromophore (in case of GFP: 4-(p-hydroxybenzyliden)-5-imidazol inone) is formed autocatalytically from the tripeptide Ser65-Tyr66-Gly67 and is positioned at the center of the β-barrel[72][73][74]. In general, fluorescent proteins have a lower relative brightness compared to organic dyes. Most of the fluorescent proteins also have their emission maximum in the green to orange range[75]. The shift in the fluorescence spectrum is achieved by changing the environment of the chromophore within the protein. This leads to different configurations of the chromophore, might distort it and changes in the hydrogen bond network around the chromophore. The chromophore or the environment can also be mutated to change the absorption and emission properties. Although fluorescent protein like GFP may show photoswitching characteristics which can be used for localization microscopy[76][77], there are proteins which are more suitable as their photoswitching mechanisms have been optimized to be controllable and at high signal to noise ratios. In 2002 *Patterson et al.* developed a photoactivatable form of GFP (photoactivatable green fluorescent protein (paGFP))[78]. Due to a mutation of the wild type GFP, the autocatalytical formation of the chromophore is interrupted.

Illumination with UV-light induces a decarboxylation and converts the dark protein into its fluorescent form[79][80].

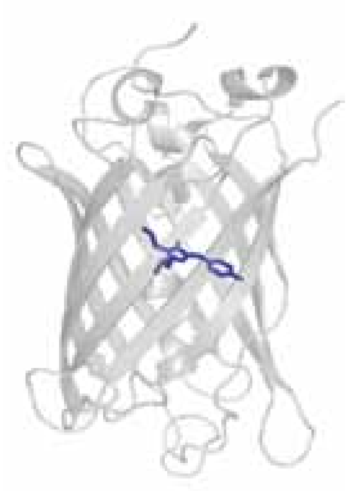

Figure 2.14: Green fluorescent protein. All fluorescent proteins like GFP show a similar structure. A fluorophore is formed by a tripeptide and located in the center of a barrel formed by eleven β-strands. (PDB: 1GFL)

Many other fluorescent proteins were synthesized, which show different fluorescent properties before and after illumination with UV-light. They originate from several wild type fluorescent proteins derived from jelly fishes like *Aequorea Victoria*, *Aequorea Coerlenscens* or from corals like *Lobophyllia Hemprichii*, *Discosoma sp.* and *Dendronephthya sp.* All these proteins have the structure of the β-barrel and the chromophore tripeptide in common, but differ in their photoswitching mechanisms[81].
Depending on their photoswitching mechanism, fluorescent proteins can be divided into three classes: reversible photoswitching, photoactivation and photoconversion (see figure 2.15).

Reversible Photoswitching Reversibly photoswitching proteins such as Dronpa switch between a bright fluorescent and a dark off state[85]. Illumination with light of 488 nm both excites and simultaneously switches off the fluorescence. 405 nm illumination will lead the chromophore back to the fluorescent state. The chromophore consists of the tripeptide Cys-Tyr-Gly. The light-driven isomerization of the tyrosyl side chain from a deprotonated cis to a protonated trans form is reversible. The cis form is fluorescent, whereas the trans form is not. After isomerization into trans, the chromophore absorbs UV-light, which induces the back reaction to the deprotonated cis form. This isomerization makes Dronpa a reversible photoswitching fluorescent protein[83][84].

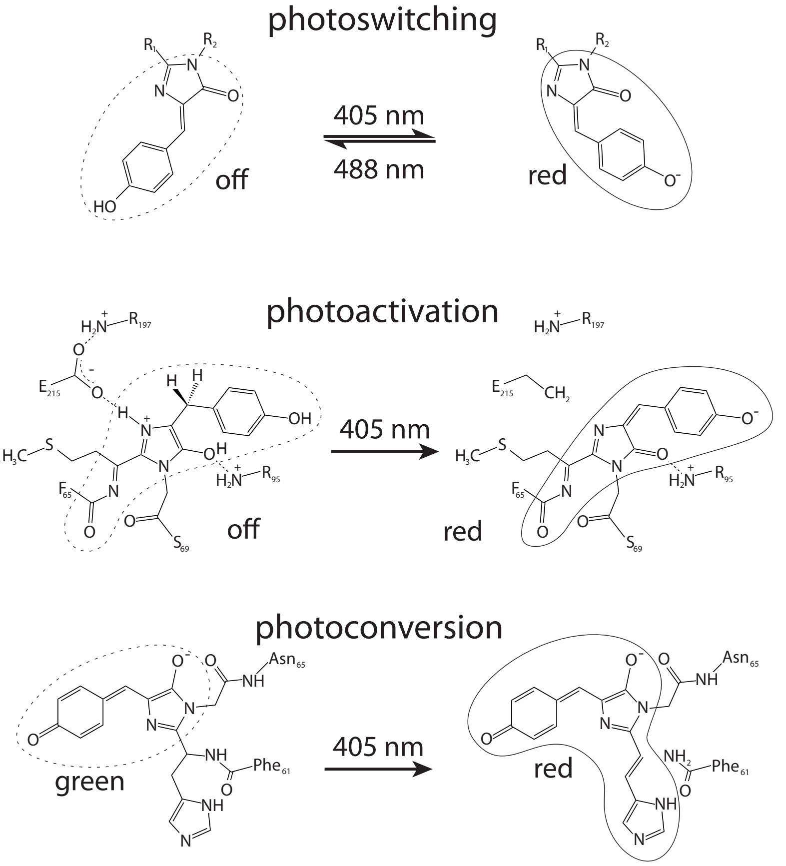

Figure 2.15: Photomanipulation of fluorescent proteins. Photoconversion usually extends the π-system of the fluorophore so that an initial green fluorescent fluorophore becomes red fluorescent. Example shows the backbone cleavage of Kaede[81]. In photoactivation, an initially dark chromophore becomes fluorescent, due to an extended π-system after a photoreaction (example shows PAmCherry1[82]). Reversible photoswitching is based on a photoinduced cis-to-trans isomerization of the chromophore (example for Dronpa[83][84]).

The fluorescent proteins mTFP0.7[86] and KFP1[87] are reported to switch in similar ways[88].

Photoactivation Photoactivatable fluorescent proteins are non-fluorescent in the beginning. After illumination with UV-light, they became fluorescent. Examples for photoactivated fluorescent proteins are paGFP[78], psCFP[89], psCFP2[90] and PAmCherry(1, 2 and 3)[91]. In contrast to reversibly photoswitching fluorescent proteins, photoconversion occurs only once.

Two underlying mechanisms are known so far. In the first mechanism, three amino acids undergo a photoinduced conversion from a neutral (protonated) to a anionic (deprotonated) state of the chromophor. Only the later one shows fluorescence. Crystal

structures proof the following mechanism for paGFP[79][80]: within the photoreaction, a decarboxylation of a glutamic acid residue takes places. This induces a reorganisation of the hydrogen bond network around the chromophore and its deprotonation.
The second mechanism was found for PAmCherry1[82]. After several mutations of the wild type protein DsRed from the coral *Discosoma sp.*, the monomeric red fluorescent protein mCherry was obtained[92][93][94]. The mutation Lys70Asn stops the autocatalytic maturation of the protein. The reaction will carry on only after irradiation with UV-light[91][82]. The first step of chromophor maturation is the cyclization of the tripeptide Met66-Tyr67-Gly68 and the formation of an N-acylimine-containing chromophore. This chromophore absorbes UV-light but does not fluoresce. In the wild type, Lys70 acts as a base and abstracts a proton of the β-carbon of Tyr67. This induces the formation of a double bond between the α- and β-carbon of Tyr67. The extension of the π-system leads to the formation of a fluorophore. With mutation of Lys70Asn, the base for the autocatalytic reaction is missing and the chromophore maturation stops at this point. However, after illumination with UV-light the excited chromophore reacts as an oxidizing reagent. An electron transfer from the deprotonated Glu215 to the excited chromophore induces a decarboxylation of the Glu215-residue. The emerging radical residue binds dioxygen which is now sufficiently reactive to abstract the proton of the β-carbon of Tyr67 in the chromophore. A second dioxygen molecule oxidizes the chromophore to its final form (N-[(E)-(5-hydroxy-1H-imidazol-2-yl)methylidene]acetamide[82].

Photoconversion: mEos2[95], Kaede[96], KikGR[97] and Dendra2[98] with a His-Tyr-Gly tripeptide as chromophore share the same photochemical conversion mechanism. A photoinduced β-elimination of the amino acid backbone at the chromophore leads to a cleavage of the peptide chain[99][100]. In the case of mEos2, Glu212 acts as a base and abstracts one of the two protons at the β-carbon of His62 (amino acid of the chromophore). A hydroxy imine residue leaves in trans-position in a type-E2-β-elimination, which undergoes rapid tautomerism to a thermodynamically more stable carbon acid amide. The tautomerism makes the reaction irreversible as it is unlikely to go into the reverse direction[81]. In addition, to the extension of the π-system of the chromophore, the backbone of the protein is cleaved.
Photoconversion usually occurs from a fluorophore and shifts the absorption and emission wavelength to longer wavelengths as the chromophor system gets extended by the photochemical reaction.

IrisFP was the first fluorescent protein which combined both the reversible photoswitching via cis-trans isomerization and irreversible photoconversion by backbone cleavage. Therefore, it is capable to switch between a fluorescent green and a non-fluorescent dark state and after the irreversible photoconversion between a red fluorescent on and dark state[88]. Later, monomeric NijiFP was developed. This fluorescent protein exhibits comparable photoswitching and photoconversion[101].

2.5.4 Photoswitching Kinetics

All photoswitching fluorophores switch between a detectable fluorescent state A and a non-fluorescent (or not detected (blue shifted) fluorescent) state D. Some fluorophores can switch between these two states several times (reversible). Other fluorophores start in a dark state, then switch to the fluorescent state and back again into a final dark state P, which is different from the initial dark state. Depending on the underlying mechanism, photoswitching occurs with different kinetics. All possible transitions between the states are shown in figure 2.16. Reversibly switching fluorophores often start in the active state A and oscillate between A and the D. With a certain probability they will irreversibly photobleach to the final product P. Irreversible switching fluorophores start in the dark state D, are activated into the state A and photobleached to the product P. D' denotes a possible second dark state, as some fluorophores (although noted as being irreversible switching) show multiple photoswitching events. For simplicity, the state D' and direct photobleaching from D to P have not been considered in the following argumentations.

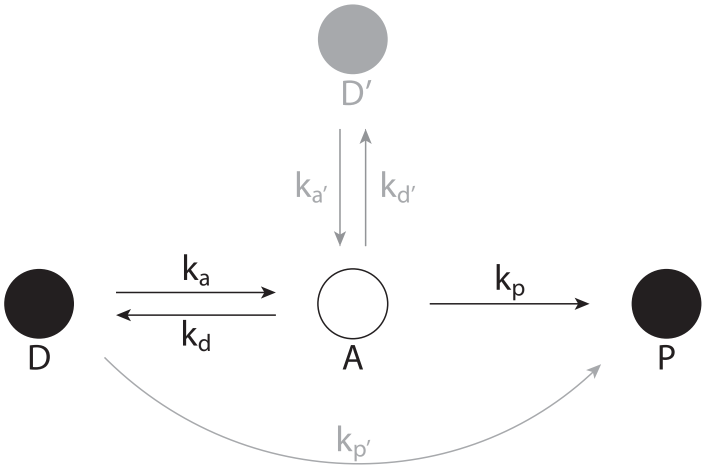

Figure 2.16: Reaction scheme of photoswitching kinetics. A denotes the fluorescent state, D the dark state and P the photobleached product. All transitions are described in the text.

Irreversible Photoswitching

The fluorophore has to be activated from the dark state, if irreversible photoswitching occurs. This happens for example by illuminating the photoconverting fluorescent protein mEos2 with UV-light. Despite the green fluorescence, the protein will not be detected in the red channel - it is in the dark state D. After the photoconversion to the fluorescent state A at a rate k_a, it is red-fluorescent. The fluorophore will bleach to the dark state P at a rate of k_p. From P it will not recover fluorescence again.

$$\mathrm{D} \xrightarrow{k_\mathrm{a}} \mathrm{A} \xrightarrow{k_\mathrm{p}} \mathrm{P}$$

Initially, all fluorophores are in D, which will be depopulated by UV-light at the kinetics described in equation 2.28.

$$\frac{dN_\mathrm{D}}{dt} = -k_\mathrm{a} N_\mathrm{D} \tag{2.28}$$

N_D denotes the number of fluorophores in state D. For $N_\mathrm{D}(t=0) = N_{\mathrm{D}_0}$ as the total number of activatable fluorophores, the differential equation can be solved as (equation 2.29):

$$N_\mathrm{D}(t) = N_{\mathrm{D}_0} \mathrm{e}^{-k_\mathrm{a} t} \tag{2.29}$$

The number of fluorophores in the activated state A changes by photobleaching at rates as given in equation 2.30.

$$\frac{dN_\mathrm{A}}{dt} = k_\mathrm{a} N_\mathrm{D} - k_\mathrm{p} N_\mathrm{A}, \tag{2.30}$$

which, for $N_\mathrm{A}(t=0) = 0$ and $k_\mathrm{a} \neq k_\mathrm{p}$, can be solved as (equation 2.31).

$$N_\mathrm{A}\left(t\right) = N_{\mathrm{D}_0} \frac{k_\mathrm{a}}{k_\mathrm{p} - k_\mathrm{a}} \left(\mathrm{e}^{-k_\mathrm{a} t} - \mathrm{e}^{-k_\mathrm{p} t}\right) \tag{2.31}$$

The number of bleached fluorophores N_P is given by equation 2.32.

$$N_{\mathrm{P}}\left(t\right) = N_{\mathrm{D}_0} + \frac{N_{\mathrm{D}_0}}{k_{\mathrm{a}} - k_{\mathrm{p}}}\left(k_{\mathrm{p}}\mathrm{e}^{-k_{\mathrm{a}}t} - k_{\mathrm{a}}\mathrm{e}^{-k_{\mathrm{p}}t}\right) \tag{2.32}$$

This leads to the limit of

$$\lim_{t\to\infty} N_{\mathrm{P}} = N_{\mathrm{t}_0}. \tag{2.33}$$

In single-molecule super-resolution microscopy, fluorophores of a densely labelled area have to be temporally separated. This can be achieved with long off times compared to short on times of the fluorophore. Therefore, the ratio r of k_a over k_0 (equation 2.34) is crucial for localization microscopy experiments. If r becomes too high, the PSFs of the fluorophores start to overlap in densely labelled areas and multiple emitters are detected as one in a diffraction-limited area (see figure 2.9). With increasing time, the number of fluorophores in the fluorescent state N_{A} decreases. To keep N_{A} constant and to decrease imaging time until all fluorophores were detected, the activation rate k_{a} can be increased by a higher UV illumination power.

$$r = \frac{k_{\mathrm{a}}}{k_{\mathrm{p}}} \tag{2.34}$$

Reversible Photoswitching

Reversible photoswitching is usually observed for all organic fluorophores and for some fluorescent proteins (e.g. Dronpa). In contrast to irreversible photoswitching fluorophores, reversible photoswitching fluorophores start in the fluorescent state A. Under constant activation, perfect reversible switching fluorophores will stay in equilibrium between the dark state D and the active state A.

$$\mathrm{A} \underset{k_{\mathrm{d}}}{\overset{k_{\mathrm{a}}}{\rightleftharpoons}} \mathrm{D}$$

The number of molecules residing in the state A (N_{A}; equation 2.35) and D (N_{D}; equation 2.36) can be described by:

$$N_{\mathrm{A}}\left(t\right) = N_{t_0}\left(\frac{k_{\mathrm{a}}}{k_{\mathrm{d}} + k_{\mathrm{a}}} + \frac{k_{\mathrm{d}}}{k_{\mathrm{a}} + k_{\mathrm{d}}}\mathrm{e}^{-(k_{\mathrm{d}}+k_{\mathrm{a}})t}\right) \tag{2.35}$$

$$N_{\mathrm{D}}(t) = N_{t_0} \frac{k_{\mathrm{d}}}{k_{\mathrm{d}} + k_{\mathrm{a}}} \left(1 - e^{-(k_{\mathrm{d}} + k_{\mathrm{a}})t}\right) \tag{2.36}$$

Like the rate r for irreversible photoswitching, the ratio r' (equation 2.37) is crucial for localization microscopy and should be well adjusted to avoid the density of PSFs.

$$r' = \frac{k_{\mathrm{a}}}{k_{\mathrm{d}}} \tag{2.37}$$

2.5.5 Colocalization Analysis

Standard colocalization approaches determine the spatial overlap in intensity of two fluorescently labelled proteins of interest. Various algorithms to quantitatively describe colocalization have been developed[102]. One of the standard measures in pattern recognition of two channels is the *Pearson's correlation coefficient* R_r which can be calculated as (equation 2.38)[102][103]:

$$R_r = \frac{\sum\limits_{i \in \mathrm{Img}} \left(\left(A_i - \bar{A}\right) \cdot \left(B_i - \bar{B}\right)\right)}{\sqrt{\sum\limits_{i \in \mathrm{Img}} \left(A_i - \bar{A}\right)^2 \cdot \sum\limits_{i \in \mathrm{Img}} \left(B_i - \bar{B}\right)^2}} \tag{2.38}$$

Here, i is the number of pixels of the image pair (Img). A_i represents the intensity of one pixel in channel A, B_i the intensity of the corresponding pixel in channel B. $\bar{A}$ and $\bar{B}$ are the average pixel intensity in channel A and B, respectively. This correlation coefficient considers the shape of intensity signals while ignoring the intensities. The values range between -1.0 and +1.0. where +1.0 represents complete colocalization and -1.0 complete anti-colocalization[102].

As the divisor in equation 2.38 is constant for every pixel in a given image set, a new image can be generated with the single summand values of the dividend as intensity. The resulting image shows areas of colocalization in positive pixel values. An example of this representation is shown in figure 4.8 of chapter 4.3. This type of colocalization analysis is named ICA[103].

ICA analysis works well on standard fluorescence microscopy images. However, localization microscopy is different as the raw data are lists of coordinates instead of intensity values. Images have to be reconstructed from these lists. Depending on the reconstruction type (see chapter 3.1.5 or *Baddeley et al.*[104]), ICA algorithms might produce artefacts in colocalization analysis. Alternatively, the obtained coordinates themselves can be used for colocalization analysis. The analysis hereby is based on distances between detected fluorophores. *Gunkel et al.* analyzed localization microscopy data based on coordinates first[76]. Later *Malkusch et al.* published a coordinate-based colocalization analysis (CBC), which also focuses on coordinate distributions and distances[105]. The CBC method also provides colocaliztation values for both analyzed channels. By comparison of the colocalization of both respective proteins in the channels, information can be drawn on which protein recruits the other (protein A completely colocalizes with protein B, but not vice versa: protein B might recruit protein A to form a protein complex).

To calculate the colocalization value C_{A_i} for a single localization A_i in channel A, first the rank correlation coefficient after *Spearman* S_{A_i} has to be evaluated (see equation 2.39)[105].

$$S_{A_i} = \frac{\sum_{r_j=0}^{R_{max}} \left(O_{D_{A_i,\mathrm{A}}}(r_j) - \bar{O}_{D_{A_i,\mathrm{A}}}\right)\left(O_{D_{A_i,\mathrm{B}}}(r_j) - \bar{O}_{D_{A_i,\mathrm{B}}}\right)}{\sqrt{\sum_{r_j=0}^{R_{max}} \left(O_{D_{A_i,\mathrm{A}}}(r_j) - \bar{O}_{D_{A_i,\mathrm{A}}}\right)^2}\sqrt{\sum_{r_j=0}^{R_{max}} \left(O_{D_{A_i,\mathrm{B}}}(r_j) - \bar{O}_{D_{A_i,\mathrm{B}}}\right)^2}} \tag{2.39}$$

Here, $O_{D_{A_i,\mathrm{A}}}(r_j)$ is the rank of $D_{A_i,\mathrm{A}}(r_j)$ calculated after *Spearman*. $\bar{O}_{D_{A_i,\mathrm{A}}}(r_j)$ is the arithmetic average of $O_{D_{A_i,\mathrm{A}}}(r_j)$.
$D_{A_i,\mathrm{A}}(r_j)$ is the distribution of localizations of channel A around the localization A_i in dependence of the distance r around A_i (see equation 2.40). $N_{A_i,\mathrm{A}}(r)$ stands for the number of localizations of species A around A_i within the distance r. The distribution is corrected for the area πr^2 and normalized by the number of localizations within the largest observed distance R_{max}. The same distribution is calculated but for molecules B surrounding localization A_i (see equation 2.41).

$$D_{A_i,\mathrm{A}}(r) = \frac{N_{A_i,\mathrm{A}}(r)}{\pi r^2} \cdot \frac{\pi R_{\mathrm{max}}^2}{N_{A_i,\mathrm{A}}(R_{\mathrm{max}})} = \frac{N_{A_i,\mathrm{A}}(r)}{N_{A_i,\mathrm{A}}(R_{\mathrm{max}})} \cdot \frac{R_{\mathrm{max}}^2}{r^2} \tag{2.40}$$

$$D_{A_i,\mathrm{B}}(r) = \frac{N_{A_i,\mathrm{B}}(r)}{N_{A_i,\mathrm{B}}(R_{\mathrm{max}})} \cdot \frac{R_{\mathrm{max}}^2}{r^2} \tag{2.41}$$

The final colocalization value C_{A_i} for every single localization of channel A_i is then calculated by equation 2.42.

$$C_{A_i} = S_{A_i} \cdot \mathrm{e}^{\left(-\frac{E_{A_i,B}}{R_{\max}}\right)} \tag{2.42}$$

C_{A_i} can reach values between -1 and 1. A perfect colocalization will yield a value of 1.

2.5.6 General Labelling of Target Proteins

In microscopy below the diffraction limit the labelling density becomes an important parameter. To resolve a structure of a certain size, its labelling density has to match the *Shannon-Nyquist* criterion. The *Shannon-Nyquist* criterion and several different approaches to label the protein of interest with a fluorophore, are described in the following paragraphs.

Shannon-Nyquist Criterion

In fluorescence microscopy, the target protein itself is not imaged, but its label. While imaging a structure, the labelling density has to be sufficiently high to resolve the structure. The Shannon-Nyquist Criterion says, that the sampling interval has to be at least twice as small as the desired resolution[106].

Labelling Strategies

There are various ways to label a protein of interest with fluorescent dye. Two well-established techniques are immunolabelling and fusions with fluorescent proteins.

In immunolabelling, a pair of primary and secondary antibody is used to label the protein of interest. The primary antibody is derived from a certain species like mouse or rabbit, which is different from the species of the investigated cell. They bind to the antigen of the protein of interest with their antigen-binding-site. The secondary antibody is specific against the specimen of the primary antibody and will bind to the primary antibody. Tagged to a fluorescent dye, the secondary antibody is observed when imaged on a fluorescence microscope. As antibodies can also bind unspecifically, there is always the risk of background signal.

When imaging the labelled protein with a localization-based microscopy technique with sub-diffraction resolution, the size of the label has to be taken into account. A drawback of all fluorescent labels is, that the observed dye might be up to 15 nm apart from the (original) protein of interest. However, as the organic dye is designed to have a high relative brightness, they will produce localizations with more photons than fluorescent proteins, which will finally end in higher resolution (see chapter 2.5.1).

Tagging a fluorescent protein to the protein of interest is another way of fluorescence labelling. Here, either a stable cell line is generated, which expresses the fusion protein as the construct is inserted into the cell's genome, or the fusion protein is expressed after transient transfection with the (cyclic) deoxyribonucleic acid (c)DNA of the fusion protein.

The labelling is stoichiometric, that is each protein carries one fluorophore, and no unspecific labelling occurs. However, the fluorescent proteins have a lower relative brightness, which leads to slightly lower localization precision compared to organic dyes. In contrast to immunolabelling this technique is suitable for live cell imaging, as antibodies affect living cells and cannot easily transfected into living cells. Important features for time lapse and quantitative experiments are the maturation time and the misfolding rate of fluorescent protein (FP)s.

A hybrid labelling approach is to use protein tags such as the CLIP-tag or SNAP-tag. Here, a mutant of the O^6-alkylguanine-DNA alkyltransferase (AGT) is fused to the protein of interest. AGT covalently binds O^6-benzylguanine (BG) derivatives. The BG derivatives themselves are tagged to a fluorescent dye of choice[107].

Many more labelling strategies are reported, which are based on for instance HALO-tag[108], TMP-tag[109] or CLICK-chemistry[110].

For the HALO-tag a chloroalkane is linked to a fluorescent dye. A mutated form of a dehalogenase (DhlA) from *Rhodococcus* is fused to the protein of interest. The chloroalkane forms an stable ester bond within the binding pocket of DhlA and labels the protein.

CLICK-chemistry for example, is based on a azide-alkyne cycloaddition[110]. The dye is conjugated to an azide group. A protein of interest can for instance be tagged with an unnatural amino acid containing an alkyne group[111] or in case of labelling DNA, oligonucleotides are alkyne-functionalized[112].

In figure 2.17 the size of some specific labels are shown with respect to the size of proteins[113].

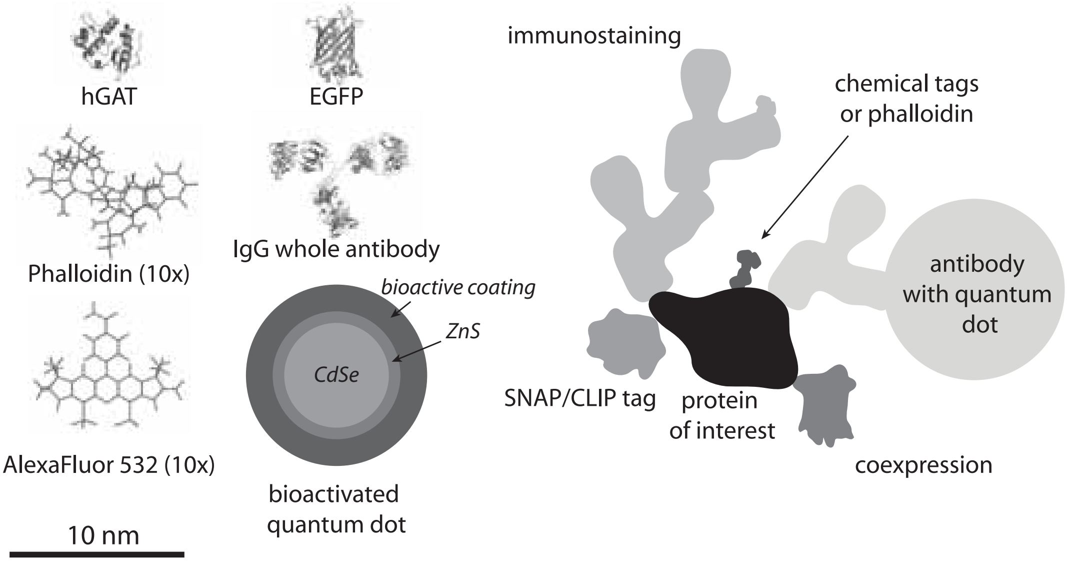

Figure 2.17: The size of a fluorescent label compared to the size of the protein of interest (adapted from *Finan et al.*)[113].

2.5.7 Dual-Color Single-Molecule Super-Resolution Experiments

Dual- (and multiple-) color localization microscopy experiments can be generally divided into two approaches. First, the fluorophores are separated according to their different spectral activation wavelength. Second, the fluorophores are discriminated by their emission wavelength.

Using only paFPs for dual color experiments does not need a buffer change to achieve reducing conditions. Aqueous buffers (like PBS) or immobilization media can be used during data acquisition. In contrast, the challenge of dual-color experiments with organic dyes is to find matching buffer conditions, under which the two used fluorophores still show optimal photoswitching. Without optimized redox conditions, thiols interfere with photoswitchable proteins and can induce blinking as well as permanent bleaching of the fluorophores[114]. In the following, some examples are described of how dual-color experiments were realized in theory.

The first mentioned approach has been realized by *Bates et al.* in 2007[115], where Cy5 and additionally Cy2 or Cy3 were conjugated to secondary antibodies. Cy5 is the reporter dye, Cy2 and Cy3 function as activator dye. In the experiment all Cy5 dyes were brought into the dark state by high excitation power and at millimolar concentrations of thiols. Activation of Cy5 from the dark state is realized by excitation of the activator dyes which will then transfer the absorbed energy to the dark state Cy5 for reactivation. Low powers and an alternated pulsed excitation of the activator dyes controls which of the Cy5 conjugates are activated from the dark state. The low activation power is crucial as it decreases the amount of crosstalk due to direct activation of the dark state. The crosstalk between both channels can reach values up to 35%[115]. An advantage of this technique is that no chromatic aberration occurs, the buffer conditions only have to match the reporter dye and no fiducial markers are required for chromatic aberration correction.

The second approach is using different dyes and separates them by their emission spectrum. This benefits from the very low to no crosstalk due to spectral separation. However, chromatic aberration occours and has to be corrected for. Usually fiducial markers (like fluorescently labelled microspheres (Tetraspeck, Invitrogen)) act as reference for these corrections. Using fluorophores which differ in their emission spectra enables parallel imaging, if excitation and activation wavelengths do not significantly overlap or interfere. A non-suitable dye pair for example is Cy5 and Alexa Fluor 532, as the activation wavelength of Cy5 is similar to the excitation wavelength of Alexa Fluor 532. Parallel imaging results in a high r' value for Cy5, which makes the distribution of active fluorophores too dense to analyze. In this case sequential imaging is preferable. Sequential imaging should be carried out with far-red dyes first, as high excitation powers at lower wavelengths were observed to bleach the fluorescence of the fluorophores at further wavelengths. A suitable dye pair was Alexa Fluor 647 (or Cy5) and mEos2 at 50 mM MEA and a pH of 7.2[114]. Another promising dye pair was Alexa Fluor 647 (or Cy5) and Alexa Fluor 532 at 100 mM MEA and a pH of 8.0[116]. Also paFPs have been used for dual-color localization microscopy[117]. This was the reversible paFP Dendra[118] and the irreversible paFP EosFP (a parent of mEos2). First EosFP has been imaged. After every EosFP had been photoconverted and read out (EosFP in the "dark" state shows fluorescence in the same spectral region as Dendra in its active state), the reversible switching FP Dendra was imaged.

Another approach for dual-color experiments is called spectral demixing *d*STORM (SD-*d*STORM)[119]. Here, two fluorophores with overlapping fluorescence spectra (Alexa Fluor 647 and AlexaFluor700) are used. The fluorophores cannot be directly distinguished by their spectra. A dichroic mirror is introduced into the emission pathways which splits the emitted light in the middle of the two emission maxima. The two channels are merged and imaged simultaneously. Each fluorophore is detected in both channels and generates one PSF in each channel, with a certain intensity ratio. This intensity ratio is specific depending on the fluoroscence spectrum of the dye and can be used for differentiation. The crosstalk in fluorophore identification is below 5%. No fiducial markers have to be used to align the channels, as each fluorophore can directly be localized from one of the two channels without any achromatic shifts.

3 Materials and Methods

This chapter covers the principal ideas and flow of work of localization-based super-resolution microscopy and its data analysis. The used setups and protocols are described generally.

3.1 Basics for *d*STORM/PALM Experiments

The quality of the final image of a localization-based microscopy experiment depends on various parameters during the data acquisition or sample preparation, for instance labelling density, photoswitching, signal-to-noise ratio and image reconstruction. Various adjustments for optimizations can be made and are described in the following sections. In appendix A, two examples of an image series with acceptable photoswitching and non-acceptable photoswitching are shown.

3.1.1 Imaging Buffer and Acquisition Settings

As every fluorophore is different in its chemical properties and in this case especially the redox potential, each fluorophore has different buffer conditions to make the fluorophore photoswitch. Most easy to use are photoactivatable fluorescent protein (paFP) as they can be switched in plain PBS. A reasonable high excitation power saturates the circle of absorption and emission and therefore enhances the rate of photon emission and the probability of entering the triplet state. From this state photobleaching occurs. The number of emitted photons stays constant; however they are emitted in a shorter time period. This allows for shorter acquisition times.

Organic dyes need a redox buffer, typically a mM-concentration of thiols and a certain pH. Thiol concentrations usually range between 10-100 mM, the pH varies between 7.2 and 8.0. For the carbo cyanine Cy5 and the structurally similar Alexa Fluor 647 it is also advised to lower the oxygen concentration (chapter 2.5.3). Out of all dyes, Cy5 and

Alexa Fluor 647 showed the highest signal-to-noise ratio and well separated signals even in densely labelled samples (appendix A shows examples of suitable and non-suitable photoswitching). These dyes can serve as reference when testing for the performance of other dyes.
In the following, the exact conditions are listed for different dyes tested within this work.

Imaging Buffers

The imaging buffer differs depending on the imaged fluorophores. Three stock solutions have to be prepared in advance.

(1) Glucose Solution
100 mg glucose
900 µL PBS
100 µL glycerin

(2) Enzyme Solution
1 mg glucose oxidase (Sigma G2133-50KU)
20 µL Tris-HCl pH 7.5 (1 M Stock)
25 µL KCL (1 M Stock)
2 µL katalase from bovine liver (C100-50MG)
4 µL TCEP (1 M Stock) or use DTT same concentration.
0,5 mL glycerin
0,45 mL water

(3) MEA/PBS
1 M stock solution (freshly prepared from salt stock; MEA: cysteamine hydrochloride (Sigma M6500-25G))

The volume of a sample chamber is filled with the respective buffer.

Alexa647/Cy5 and **mEos2**
950 µL of PBS
50 µL of (3)
5 µL of 1 M NaOH

Alexa647/Cy5 and **Alexa532**
900 µL of PBS
100 µL of (3)
15 µL of 1 M NaOH

STORM buffer mix with low Alexa647/Cy5 labelling

Alexa647/Cy5 and **mEos2**
400 µL of (1)
50 µL of (2)
50 µL of (3)
450 µL of PBS
5 µL of 1 M NaOH

Alexa647/Cy5 and **Alexa532**
400 µL of (1)
50 µL of (2)
100 µL of (3)
400 µL of PBS
15 µL of 1 M NaOH

Small structures or sparsely distributed proteins have to be imaged under oxygen removal, as oxygen photobleaches Alexa Fluor 647/Cy5 very efficiently[68]. The sample chamber has to be sealed with for example with an additional coverslip or a silicon sheet.

3.1.2 Illumination Mode

Changing the angle of illumination between epi, HILO and TIR helps to reduce background excitation and increases excitation intensity on the illuminated plane[32]. Therefore, the signal-to-noise ratio can be adapted, as well as the photoswitching rate is changed to faster off switching rates.

3.1.3 Image Acquisition

The integration time of the camera should be chosen as such that a blinking event can be captured on one to two frames on average (usually the integration time ranges between

10 - 200 ms). This was, the number of photons per molecule per frame and with this the signal-to-noise ratio is maximized, which allows more precise detection of the center of the fluorophore (chapter 2.5.1). For a high signal to noise ratio, also signal amplification should be used, such as the electromagnetic (em) gain of an electron-multiplied charge coupled device (EMCCD). By this the maximum possible dynamic range of the camera is used and the observed signals show finer binning by the analogue-to-digital conversion. This enhanced binning of the signal allows for higher accuracy in the fitting process for the determination of the center of a PSF. Some cameras offer a frame transfer option. Enabling this option reduces the dead time of the camera (the acquired photon distribution is shifted onto a second array for read-out, so that the detector array is free to acquire new signal). As the number of fluorophores should not exceed a level, at which the PSFs start to overlap (chapter 2.5.4). However, a very low number of detected PSFs might just increase imaging time. The optimization is done by adjusting the rate r or r' respectively. Increasing $r(r')$ means more detected fluorophores per frame, decreasing $r(r')$ means less detected fluorophores per frame.

The integration time of the camera should be chosen as such that a blinking event can be captured on one to two frames on average (usually the integration time ranges between 10 - 200 ms). This was, the number of photons per molecule per frame and with this the signal-to-noise ratio is maximized, which allows more precise detection of the center of the fluorophore (chapter 2.5.1). For a high signal to noise ratio, also signal amplification should be used, such as the em gain of an EMCCD. By this the maximum possible dynamic range of the camera is used and the observed signals show finer binning by the analog-to-digital conversion. This enhanced binning of the signal allows for higher accuracy in the fitting process for the determination of the center of a PSF. Some cameras offer a frame transfer option. Enabling this option reduces the dead time of the camera (the aquired photon distribution is shifted onto a second array for read-out, so that the detector array is free to aquire new signal). As the number of fluorophores should not exceed a level, at which the PSFs start to overlap (chapter 2.5.4). However, a very low number of detected PSFs might just increase imaging time. The optimization is done by adjusting the rate r or r' respectively. Increasing $r(r')$ means more detected fluorophores per frame, decreasing $r(r')$ means less detected fluorophores per frame.

Increasing the rate $r(r')$ is usually more simple than contrariwise, as in most cases the activation rate k_a can directly be controlled by the power of the activation laser.

For irreversible switching, the bleaching rate k_p can be increased by using a higher excitation power. By this means r is decreased. The same is valid for the deactivation rate k_d at reversible switching, as the probability for a fluorophore to enter the triplet

state is getting higher.
However, for some reversible blinking fluorophores, k_a cannot be controlled and/or is comparably high. If this is the case, r' may not be decreased to an unsuited value, which is required for single molecule detection. In this case, the fluorophore is not suited for localization-based microscopy.

3.1.4 Camera and Laser Settings

Dual (or triple) color experiments were carried out sequentially with imaging starting at the red channel. The following camera settings were used:

- Integration time: 30 - 50 ms (Alexa Fluor 647/Cy5, Alexa Fluor 532), 100 - 200 ms (mEos2)
- Pre amplifier gain: 1
- EM gain: 200
- Frame transfer: on
- Read out rate: 10 MHz at 14 bit
- Number of images: 5000 - 15000 frames

Custom built setup (chapter 3.3.1, excitation powers were measured after the objective. The laser is a argon/krypton ion laser (Innova70C, Coherent, Germany))

- Alexa Fluor 647/Cy5: 647 nm at 35 - 50 mW (ca. 5 kW/cm^2)
- mEos2: 568 nm at 25 - 30 mW (ca. 3 kW/cm^2)
- Alexa Fluor 532: 514 nm at 100 mW (ca. 10 kW/cm^2)

Olympus setup (chapter 3.3.2, excitation powers were measured after the objective.)

- AlexaFluor640/Cy5: 647 nm at 35 mW (ca. 4 kW/cm^2) (LAS/491, Olympus, Japan)
- mEos2: 561 nm at 60 mW (ca. 5 kW/cm^2) (Sapphire561-FP, Coherent, Germany)
- Alexa Fluor 532: 532 nm at 300 mW (ca. 20 kW/cm^2) (LAS/640, Olympus, Japan)

Reactivation of Alexa Fluor 647/Cy5 in the absence of mEos2 and Alexa Fluor 532 was realized by low excitation powers of 514(532) nm in the µW regime. Same excitation powers are valid for photoactivation of mEos2 at an activation wavelength of 405 nm.

3.1.5 Image Reconstruction

PSFs of single fluorophores appear as Airy patterns (chapter 2.3.4). The analysis software has to detect and identify this PSFs and determine their center positions.

The intensity pattern of a single fluorophore is described by a Bessel function. Aproximating a PSF by fitting Bessel functions is time consuming, as the functions are rather complex in computation[120]. However, if the PSFs are fitted with a two-dimensional Gaussian function, the resulting error is negligible[57][121][122]. Identifying the center of fluorophores by two-dimensional Gaussian fitting is done by software like rapidSTORM[123] or QuickPALM[124] (Plug-in for ImageJ/FIJI[125]).
A second way to determine the center of the PSF has been realized in the software called *SimpleSTORM*, which was developed in collaboration with the group of *Fred Hamprecht*[126][127]. First, the pixel with the maximum intensity of the according PSF is determined. A region of this image with a size of 9 x 9 pixel and the maximum pixel in the center is chosen and a spline interpolation is applied, where the step size (corresponds to the pixel size of the reconstructed image) is defined by the user. In the interpolated image, the new pixel with maximum intensity is defined as center of the PSF, its coordinate is stored at subpixel resolution of the original image.

Thus the single fluorophore data of a localization-based microscopy experiment is not an intensity image, but a list of coordinates with additional information like frame number, symmetry of the PSF, total intensity and/or signal-to-noise ratio. Images can be generated from the list of localizations in various ways. The most straight forward way is to use a scatter plot. Every localization is displayed as a symbol which can vary in shape or color to denote any characteristics of the localization itself (like intensity or frame number). However this representation is not suitable for dense structures when localizations start to overlap. Here, the data is represented in two different ways. The software *SimpleSTORM*[126][127] resizes the raw data image size by up-sampling one pixel into 10 x 10 pixels. The localizations are displayed in one pixel of the up-scaled image with an intensity based on the signal to noise ratio. rapidSTORM[123] allocates a square of four pixels to each localization to moderate pixilation effects.
Further information on displaying localization microscopy data can be found for example in *Endesfelder*[33], *Baddeley et al.* [104] or *Gunkel*[128] .

3.2 Experimental and Protocols

This section covers the protocols used to prepare the samples which were analyzed within this work. Additionally the microscope and camera settings are described, which were applied to record the microscopy data.

3.2.1 General Sample Preparation

The described procedure is a general protocol which eventually required some adaptation for individual experiments.

Cell Seeding, Fixation, Histochemistry and Transfection
All volumes and amounts in the described steps refer to the preparation of a single well of a 8-well chambered coverslip (LabtekI, Thermo Scientific Inc.).

Surface Cleaning
NaOH (200 µL, 2 M, AppliChem) was pipetted into the chamber and incubated for 20 minutes. After washing with PBS (3 x 5 minutes, 200 µL, AppliChem) poly-L-lysine (150 µL, Sigma) was added and incubated for 10 minutes and washed with PBS (3 x, 200 µL).

Seeding of HeLa cells
Following steps were performed under sterile conditions.
The growth medium was taken off the cell culture stock (HeLa) and the culture flask was washed once with PBS (1 mL). Trypsin (1.5 mL, Sigma) was added and the cell culture flask was swung for an equal distribution. The trypsin was taken off again and the cell culture flask was incubated for two minutes at 37 ℃ and 5% CO_2 in the incubator (Nuaire DHD Autoflow, IBS Integra BioScience). The detached cells were taken up in growth medium (5 mL, DMEM, 10% FCS, 5% PenStrep, 5% L-glutamine) and diluted to a concentration of 37.5 cells per micro liter. The diluted cell solution (400 µL) was pipetted onto the previously prepared sample chamber (15000 cells total). The cells were incubated for 24 hours at 37 ℃ and 5% CO_2.

Transfection with actin-mEos2
The plasmid (0.12 µL, 857 ng/L, actin-mEos2) was pipetted into serum-free medium (39.7 µL, DMEM, 5% PenStrep, 5% L-glutamine). Transfection reagent (0.2 µL, TurboFect, Fermentas) was added and the mixture was incubated for 15 minutes at room temperature. The transfection mixture was added onto the growth medium in the cham-

ber of the cell culture. The chamber was swung carefully and incubated for 12-24 hours at 37 °C and 5% CO_2.

Fixation and Immunostaining
Growth medium was removed from the sample chamber and an aqueous para-formaldehyde solution (200 µL, 3 v/v% in PBS, Polyscience) was added. After 15 min of incubation at room temperature, the solution was removed and the chamber was washed with PBS (3 x 200 µL, 5 min). A solution of fluorescent fiducial markers (200 µL, TetraSpeck, Invitrogen, 0.1 µm in diameter, diluted 1:500 in PBS containing 5% BSA) was added and incubated for 30 minutes (optionally; or 1:1000 dilution within the *d*STORMimaging buffer). After washing with PBS (3 x 200 µL, 5 min), a solution with primary antibody (150 µL, 2 µg/mL, see table B.1) was added and incubated for 60 minutes at room temperature. The cells were washed with PBS (3 x 200 µL, 5 min) and a solution of secondary antibody (150 µL, 5 µg/mL, see table B.1) was added. After 60 minutes of incubation at room temperature, the cells were washed with PBS (3 x 200 µL, 5min) and post fixed with PFA (200 µL, 3 v/v% in PBS, Polyscience) for 15 minutes at room temperature. After a last washing with PBS (3 x 200 µL, 5 min) cells are ready to image or can be stored at 4 °C for later imaging.

3.2.2 Sample Preparation for a Small-Scale Screen

The sample preparation protocol is adopted from *Flottmann et al.*[116].

NRK (normal rat kidney, CRL-6509; ATCC, Manassas, VA) cells were stably transfected with GalT tagged to CFP (NRK-GalT-CFP) and cultured in DMEM (GIBCO/ Invitrogen, CA) containing 5% fetal bovine serum (FBS), 1% non-essential amino acids (GIBCO/Invitrogen), 2 mM glutamine, 100 U/mL penicillin and 100 µg/mL streptomycin. Poly-L-lysine (Sigma-Aldrich, M0) was applied to µ-Slides for 15 min before cell plating. Cells were plated on µ-slides (IBIDI, Martinsried, Germany) at densities of 15,000 cells/well 24 h before drug treatment. Brefeldin A and nocodazole (Calbiochem/Merck Chemicals, Darmstadt, Germany) treatment was performed by adding 5 µg/mL and 1 µg/mL respectively for 20 min. Cycloheximide (0.1 mg/mL; Sigma-Aldrich) was added to stop protein synthesis.

Immunostaining
Cells were fixed incubating in 3% PFA for 20 min. TetraSpeck microspheres (0.1 µm; Invitrogen) were applied for 15 min, and cells were permeabilized by incubation with 0.1% Triton-X-100 for 5 min. GalT-CFP was counter-stained with anti-GFP (6556, polyclonal rabbit; Abcam, Camebridge, UK) and anti-rabbit Alexa Fluor 532 (Invit-

rogen). GM130 was stained with anti-GM130 (monoclonal mouse; BD Biosciences, Franklin Lakes, NJ) and anti-mouse Alexa Fluor 647 (Invitrogen).

CFP-emission does spectrally overlap with Alexa Fluor 532. However, excitation with 514(532) nm does not excite fluorescence of CFP. Therefore, no additional background signal was observed.

3.2.3 Widefield and Confocal Image Acquisition

Widefield Microscopy
Widefield images were acquired with an Olympus IX81 microscope with a 10 x objective lens (Olympus UPlanSApo, NA 0.4, Japan) and a field of view of 866 µm x 660 µm. The sample was illuminated by an 150 W Hg/Xe mixed gas arc burner together with appropriate filter combinations for DAPI, Alexa Fluor 532, and Alexa Fluor 647, respectively. Integration times were set to 200 ms (20 ms for DAPI staining), which were the best match to the dynamic range of the CCD camera. In total, 50 fields of view were recorded for each condition to select the cells of interest (adopted from *Flottmann et al.*[116]).

Confocal Microscopy
The confocal microscope (SP5, Leica, Mannheim, Germany) is equipped with a 63 x objective lens (Leica HCX PL APO, NA 1.40, Mannheim, Germany), a scan speed of 400 Hz at 512 x 512 pixels and with a pixel size of 69 nm, resulting in a field of view of 49 µm x 49 µm (pinhole diameter of 96 µm). For each cell, 47 image planes with an axial distance of 0.2 µm were acquired. Selected cells were initially positioned in the center of the z-stack by an autofocus routine before acquisition. Image acquisition took 196 s at each position, subsequent positions could be acquired every 212 s including positioning of the stage and autofocus routines. In total, confocal multicolor 3-D stacks were imaged at 796 single positions within 46.9 h. (adopted from *Flottmann et al.*[116]).

Super-resolution Imaging
Localization-based microscopy was performed on selected cells as described before (chapter 3.1.4).

3.2.4 Preparation of mRNA Probe Samples and Single-Molecule Imaging

The target DNA strand for the probe was modified with biotin at the 5'-terminus and attached to a surface via BSA-Biotin streptavidin at single molecule concentration. To investigate whether photoactivation is selective, various combinations of ODN1 and ODN2 and control ODNs were analyzed.

Sample Preparation

Between each preparation step, the sample chamber was washed three times with deoxygenated PBS containing 1 M NaCl (phosphate-buffered saline; + 1 M NaCl; oxygen removed (PBS*)). Oxygen was removed from all solutions to avoid any activation before the experiment was started. The higher salt concentration increases binding efficiency of the ODN probes to the target DNA. All reactions were performed at room temperature.

To clean the surface, NaOH (200 µL, 2 M) was added into a chamber of an 8-well-chambered coverslip (LabTekII, Nunc) and incubated for 15 min. After washing with PBS*, a solution of BSA/BSA-Biotin (200 µL, 100:1, 5 mg/mL in PBS*) was pipetted into the chamber and incubated for one hour. The chamber was washed and a solution of streptavidin (200 µL, 2 mg/mL in PBS*) was added. After 15 minutes the chamber was washed and the surface was incubated with the target DNA (200 µL, 0.36 µM in PBS*) for 15 min. After washing, ODN1 (200 µL, 0.36 µM in PBS*) was added and incubated for 90 min. The sample was washed and ODN2 (200 µL, 0.12 µM in PBS*) was pipetted into the chamber. After 90 min incubation, the sample was washed and transferred to the microscope for data acquisition. Right before the start of the experiment, deoxygenated PBS* was replaced by oxygenated PBS* to enable photoinduced cleavage.

Data Acquisition

For image acquisition, 1500 frames were recorded at an integration time of 100 ms, a preamplifier gain of 1, EM-gain of 200 and in frame transfer mode. A 580/60 bandpass and a 532 longpass filter were used to block any background light from the emitted light. A dichroic mirror (DC1 at the custom-built setup; see table 3.1) was used to separate excitation from emission light. The excitation was performed under TIR illumination to only excite and observe molecules, which are in close proximity to the surface. The excitation power of 514 nm was kept at 0.5-1 kW/cm^2, which was the lowest level to record signals and avoid photobleaching. Photoactivation with 647 nm excitation was performed at a power of 1-2 kW/cm^2 to ensure a high activation rate.

When data acquisition was started the 514 nm laser line was switched on. Directly after 40 s (400 frames) the 647 nm laser line was also switched on.

3.3 Microscopy Systems

In principle, a microscope suitable for localization-based microscopy ((d)STORM, PALM, PALMIRA, FPALM, GSDIM) is a standard widefield TIR fluorescence microscope with additional capabilities. Essential elements are a strong laser source, an objective with a high numerical aperture capable for TIR/HILO illumination, and a single-photon sensitive camera with an EMCCD) or a scientific complementary metal oxyde semiconductor (sCMOS) chip. In this work, two different setups were built and are described in more detail below. The software Andor SOLIS for Imaging (version 4.13.3, Andor Technology, Ireland) is used for image acquisition.

3.3.1 Custom-Built Localization Microscope

The microscope body is based on an inverted microscope (Olympus IX71,Olympus, Japan) and placed on an air damped optical table (see figure 3.1). The system is equipped with an immersion oil objective suitable for TIR/HILO imaging (Plan ApoN 60x / 1.45 oil, Olympus, Japan). The implemented filters and dichroic mirrors are listed in table 3.1.

The excitation light is provided by a multi-line Ar/Kr-ion laser (InnovaI70C, Coherent, USA). An acousto-optical tunable filter (AOTF) (Pegasus) selects the desired excitation wavelength. A clean-up filter is used to block any other wavelengths. A second laser generates light of 405 nm (Cube, Coherent, USA). Both lasers are overlaid by dichroic and silver coated mirrors (suitable for the visible spectrum of light). The combined lasers are focused onto the back-focal plane of the objective via a lens telescope. A manually movable mirror can be used to direct the beam into TIR/HILO illumination. Emission light is collected by the objective and separated from the excitation light by a dichroic mirror. A pair of long path and band path filter is used to filter out any (non emission) background light. The emitted light is then focussed by the tube lens and a telescope (2.5 x magnification) onto the chip of an EMCCD camera (iXon DV 887, Andor, Ireland). The physical pixel size of 16 x 16 μm^2 corresponds to 107 x 107 nm^2 in the image. A cylindrical lens (CL) can be placed in between the tube lens and the camera by a custom-built adapter.

3.3.2 Enhanced OlympusIX81 TIRF Microscope

The OlympusIX81 (Olympus, Japan) is a fully-automated widefield fluorescence microscope, equipped with an oil immersion objective (UApo N 150 x 1.45, Olympus, Japan)

Table 3.1: List of dichroic mirrors, filters and lenss used in the custom built localization microscope.

lens	Focal Length
Custom Built Setup	
L_1	30 mm
L_2	120 mm
L_3	160 mm
L_4	270 mm
Enhanced OlympusIX81 TIRF	
L_1	-10 mm
L_2	200 mm
CL	1000 mm
Filter	Name
Custom Built Setup	
CU (1)	ZET 514/10
CU (2)	ZET 568/10
BP (1)	550/80 Brightline HC
BP (2)	580/60 Brightline HC
BP (3)	610/60 ET Bandpass
BP (4)	775/75 ET Bandpass
Enhanced OlympusIX81 TIRF	
BP (1)	ZET 532/640
BP (2)	532/50 ET Bandpass
BP (3)	605/70 ET Bandpass
Dichroic Mirror	Name
Custom Built Setup	
DC_1	BSR405
DC_2 (1)	FF560/659
DC_2 (2)	FF73-866
Enhanced OlympusIX81 TIRF	
DC (1)	620 DCXR
DC (2)	HC Quadband R405/488/561/635

and an EMCCD camera (iXon DV897DC, Andor, Ireland) as shown schematically in figure 3.2. A pixel in a recorded image has a size of 107 x 107 nm. The microscope is placed on an air damped table. The system is equipped with 405, 491, 532, 561 and 640 nm excitation lasers (405 nm: Cube, Coherent, Germany; 488 nm: LAS/491, Olympus, Japan; 561 nm: Sapphire561-FP, Coherent, Germany; 647 nm: Las/640, Olympus, Japan). Except for the 532 nm laser (EO-PS-II, Eksma Optics, Lithuania), all other lasers are coupled into the fully-automated TIRF unit via optical fibres (cell^TIRF motorized multicolor TIRF, Olympus, Japan). The TIRF unit enables motorized adjustment of the illumination angle (widefield or TIR/HILO). The 532 nm laser is freely coupled into the microscope via a port of the TIRF unit, which was originally designed for only widefield epi-fluorescence imaging with a metal halide lamp. A telescope focuses the beam onto the back focal plane of the objective. A manual switch at the TIRF unit can change between epi (532 nm) and TIR/HILO (405, 491, 561, 640 nm) illumination.

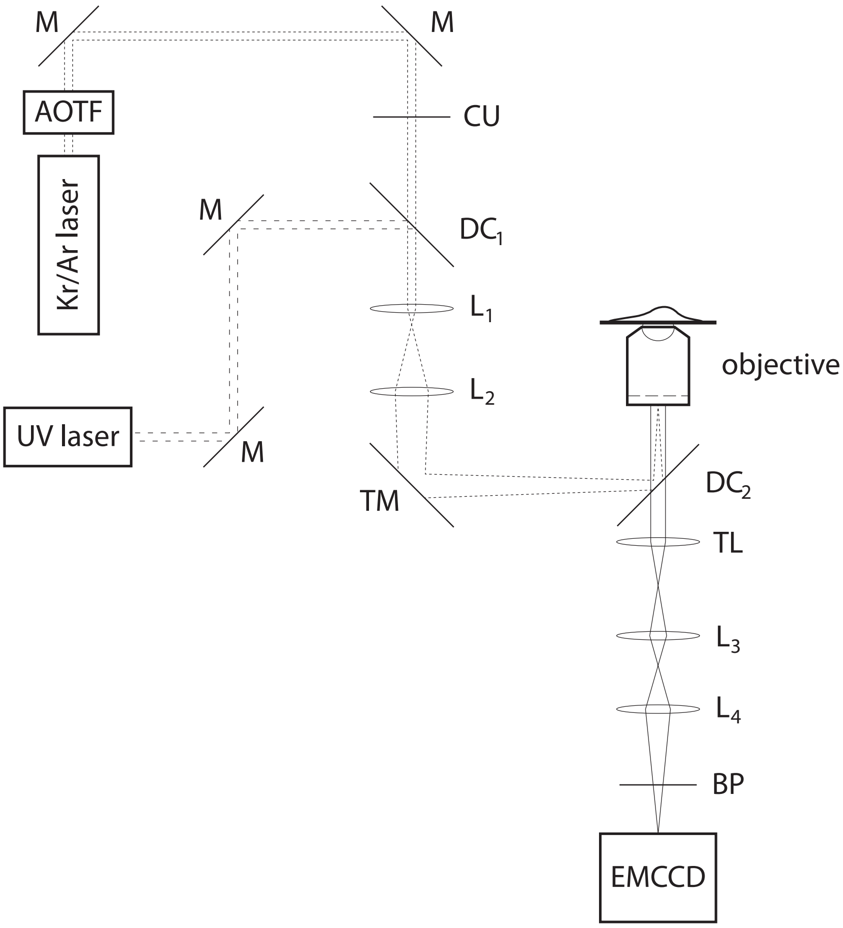

Figure 3.1: Scheme of the custom built *d*STORM/PALM setup. The excitation laser is generated by an argon/krypton ion laser (Innova70C, Coherent, Germany). The AOTF filters the desired excitation wavelength. The beam is combined with an UV-laser beam used for photoactivation by a dichroic mirror (DC_1). The combined beam is focussed onto the backfocal plane of the objective of the microscope by a telescope ($L_1 + L_2$). A second dichroic mirror (DC_2) separates the emission from the excitation wavelength. The emitted light is focussed onto the camera by a tube lens (TL) and post-magnified by a telescope ($L_3 + L_4$). A band pass filter (BP) blocks any background light. A movable mirror (TM) is used to adjust the illumination between widefield, HILO and TIR (see figure 2.7). lenss and filters are listed in table 3.1

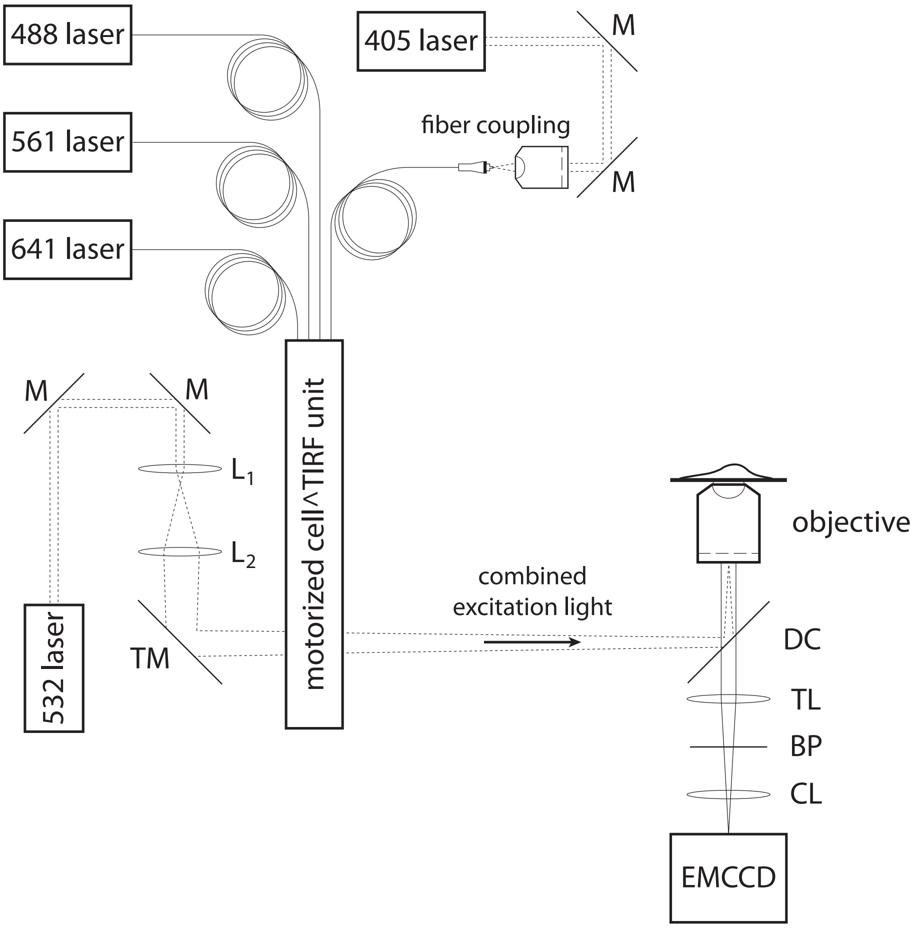

Figure 3.2: The 488 nm, 561 nm and 641 nm lasers are directly, a 405 nm diode laser (Cube, Coherent, Germany) freely coupled into optical fibers and connected to a motorized Olympus cell^TIRF unit. This unit focuses the light onto the backfocal plane of the objective. A 532 nm laser is freely focussed onto the backfocal plane of the objective with a telescope ($L_1 + L_2$) by using the entry of the TIRF unit designed for widefield epi-fluorescence with a metal halide lamp. A movable mirror (TM) enables for widefield, HILO and TIR illumination (see figure 2.7). A dichroic mirror (DC_1) separates emission from excitation light. A band pass filter (BP) blocks any background light, the tube lens (TL) focuses the emitted light onto the camera. A cylindrical lens (CL) can be placed into the beam path for 3D-*d*STORM via astigmatism. lenss and filters are listed in table 3.1.

4 A High-Throughput High-Resolution Microscopy Platform

Systems biology aims to map processes in a living organism and single cells. The holistic perspective of systems biology shall describe the life of cells, tissues and organisms as wholes and not as a collection of parts. To understand the interconnection in signalling pathways or metabolic networks, a large amount of data is required. Screening methods are crucial to gather a sufficiently high quantity of data within a reasonable amount of time.

One approach to visualize cellular processes is high-throughput screening microscopy. By using microwell cell arrays, several thousands of experiments can be carried out and imaged on a screening microscope[11]. Screening microscopy already offers a lot of information on the response of cells under different conditions, like it has been shown for a genome-wide screen of fluorescently labelled chromosomes with phenotypic profiling[12]. Here, time-resolved profiles of RNAi-induced loss-of-function phenotypes resulting from siRNAs targeting the entire human genome where acquired. However, as screening microscopy is based on conventional widefield and confocal read-out, the information is limited by diffraction. In contrast, super-resolution microscopy techniques offer nanoscale information on protein organization, but are limited in acquisition time and field of view. Thus they hardly give a holistic overview on large samples or sample numbers and they are very labor-intensive and time consuming in recording.

To fill this gap, a new technology platform was developed. An integrated microscopy platform for correlative light microscopy of high-content screens has been built to combine widefield screening, confocal and localization-based microscopy techniques in one system[116]. By using the *Konstanz Information Miner* (KNIME)[14], the platform was automated to allow for microwell cell array in a fast widefield screening mode and furthermore select cells of interest for further investigation by automated confocal and/or localization-based microscopy. The platform has the ability to add information on molecular distribution of proteins within a single pre-selected cell to the overall statistical overview of screening microscopy.

4.1 Microscopic Setup and Workflow

The platform is a combination of three microscopes: an Olympus IX81 widefield screening microscope equipped with the scan^R software (Olympus, Japan); the confocal microscope Leica TCS SP5 II (Leica, Germany); and the custom-built localization microscope equipped with a motorized stage (Märzhäuser, Germany). The overall workflow of the imaging routine is as follows (see also figure 4.1):

1. Record images of reference markers on widefield setup.
2. Record low-magnification screen on widefield setup.
3. Manual / automatic identification of target cells and their positions.

4. Transfer sample onto confocal setup and record reference markers.
5. Coordinate transformation of cell positions.
6. Record images of target cells on confocal setup.

7. Transfer sample onto *d*STORM microscope and record reference markers.
8. Coordinate transformation of cell positions.
9. Record localization-based microscopy data of target cells.

Instead of external reference markers, single cells can also be taken as reference. Depending on the desired level of detail, it can be chosen between the confocal (continue with step 4) and localization-based mode (continue with step 7). If both was desired, the given order was followed.

4.2 Integration of a Localization Microscopy into a Screening Microscopy Platform

The following section covers the description and characterization of the microscopy platform. This includes the identification of suitable dye pairs for combined dual-color microscopy in the widefield, confocal and super-resolution mode, the correction for chromatic aberration and the relocalization of individually selected cells on various setups, which are part of the microscopy platform.

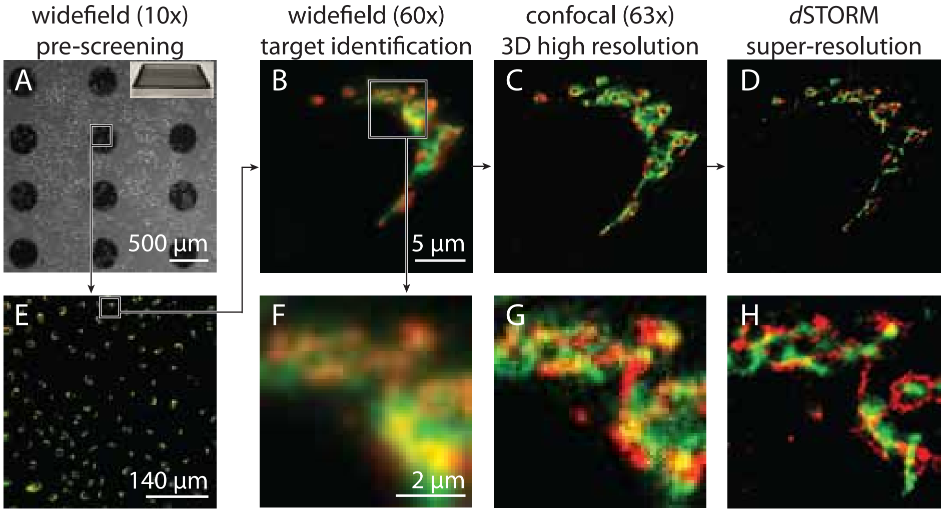

Figure 4.1: In general, the cell array with the sample cells ((A) here: NRK cells with GalT-Alexa Fluor 647 (red) and GM130-Alexa Fluor 532 (green)) is imaged on a widefield screening microscope with low magnification (E). Cells and structures of interest are selected automatically or manually and further imaged with different optical settings (B) or at different microscopes (confocal (C), *d*STORM(D)) for further information. (F), (G), and (H) show enlarged regions of the respective image as indicated in (B). (Image taken from *Flottmann et al.* [116]; Image shows GalT (red) and GM130 (green) of NRK cells.)

4.2.1 Fluorophores for *d*STORM Imaging

Several different dyes were tested, to be suitable for widefield and confocal imaging, as well as subsequent localization-based microscopy. Three dyes and one paFP turned out to show suitable characteristics for single-color localization-based microscopy. They revealed a high signal-to-noise and suitable blinking ratios r and r' (see chapter 2.5.4 and appendix A). In figure 4.2, super-resolution images of Alexa Fluor 647/Cy5, Alexa Fluor 532, Alexa Fluor488 and the paFP mEos2 are illustrated. As mentioned before, Alexa Fluor488 only showed suitable characteristics when used as conjugate to phalloidin.

The used labelling and imaging protocols can be found in the chapter 3.2.1 and chapter 3.1.4.

The achieved resolutions for the two dyes used in the high-throughput high-resolution platform (figure 4.3) were determined to $\sigma_{\mathrm{SMLM}} = 12.5\,\mathrm{nm}$ for Alexa Fluor 532 and $\sigma_{\mathrm{SMLM}} = 7.0\,\mathrm{nm}$ for Alexa Fluor 647. These calculations are based on pair-wise displacement distributions as described in *Endesfelder et al.* in 2014 (chapter 2.5.1)[59].

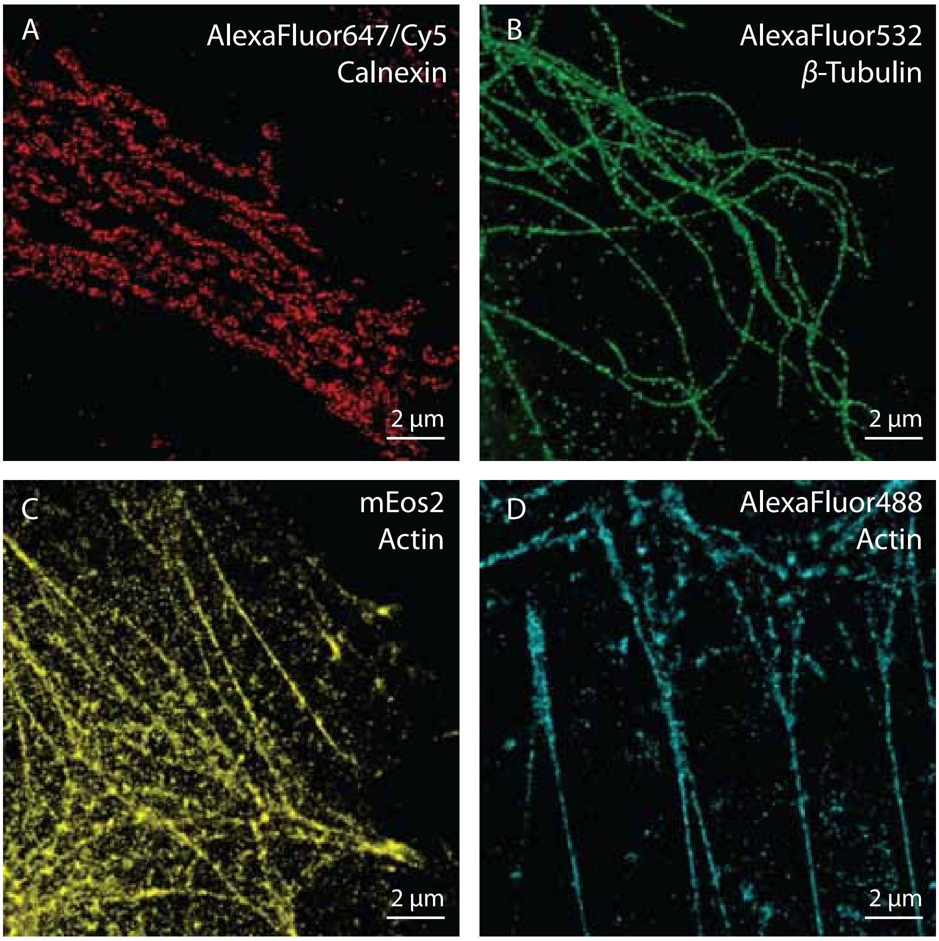

Figure 4.2: (A)-(D) Super-resolution images on various cellular structures in HeLa cells imaged with different fluorescence reporters. (A): Calnexin labelled via antibody staining with Alexa Fluor 647. (B): β-Tubulin labelled via antibody staining with Alexa Fluor 532. (C): Actin labelled via transfection with fusion protein actin-mEos2. (D): Actin labelled via phalloidin-Alexa Fluor488.

4.2.2 Dual-Color Dye Pairs for Super-resolution Microscopy

From these fluorphores, two pairs turned out to be adaptive for dual-color experiments which were Alexa Fluor 647-Alexa Fluor 532 and Alexa Fluor 647-mEos2 (chapter 3.1.4). The combination of Alexa Fluor 647, mEos2 and Alexa Fluor488 was demonstrated in triple-color super-resolution experiments. However, in this combination, Alexa Fluor488 only yielded good quality data when conjugated to phalloidin.

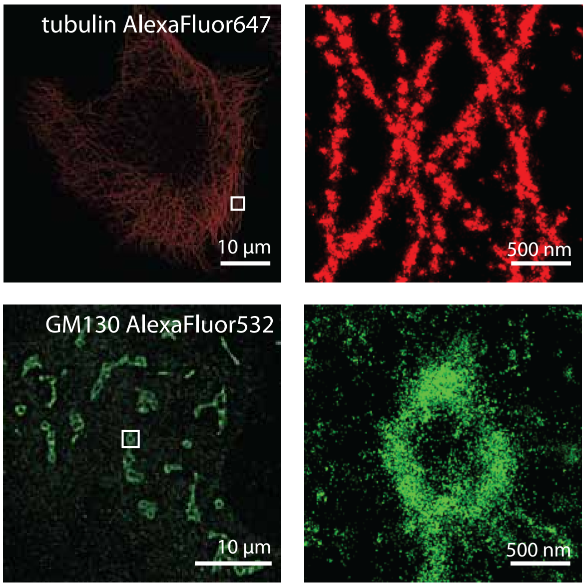

Figure 4.3: Super-resolution images of Alexa Fluor 647 and Alexa Fluor 532 on which the resolution was determined to be $\sigma_{\mathrm{SMLM}} = 7.0\,\mathrm{nm}$ and $\sigma_{\mathrm{SMLM}} = 12.5\,\mathrm{nm}$, respectively.

4.2.3 Correction of Chromatic Aberration

The acquisition of subdiffractional data sets in different color channels is prone to errors arising from chromatic aberration. To correct therefore, fluorescent microspheres (Tetraspeck, Invitrogen, USA) were used as fiducial markers, added into the sample (chapter 3.2.1) and imaged simultaneously.

In collaboration with *Ullrich Köthe*, the software *Color-Composer*[126] was developed to correct super-resolution data for chromatic aberration by fiducial markers. Localizations were detected from the raw images using either the software rapidSTORM or *SimpleSTORM*. If localizations were detected in more than 90% of the frames within a radius of 200 nm, these were assigned to the fiducial markers. This recognition is performed for both of the imaged channels. The centers are determined by averaging over all detected localizations for each marker. From the positions of the assigned fiducial markers of one channel, an affine linear transformation matrix was generated and used for alignment[126]. The alignment can be carried out with a precision up to 10 nm by using a minimum of 9 fiducial markers (see chapter 4.2.3).

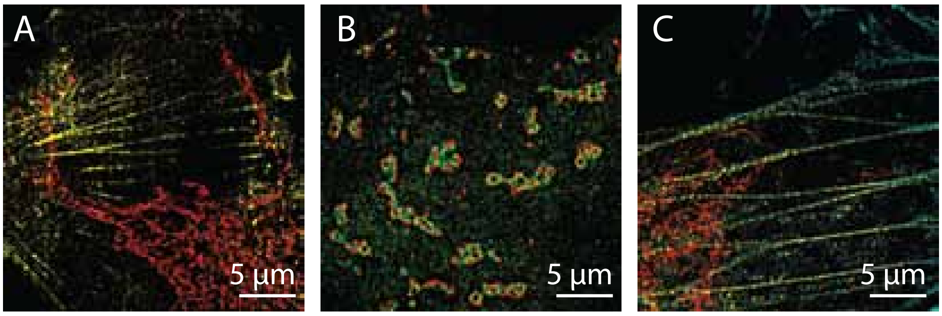

Figure 4.4: Two color super-resolution images of (A) calnexin-Alexa Fluor 647 (red) and actin-mEos2 (yellow), (B) GalT-Alexa Fluor 647 (red) and GM130-Alexa Fluor 532 (green). Three-color super-resolution image of (C) calnexin-Alexa Fluor 647 (red), actin-mEos2 (yellow) and actin-Alexa Fluor488 (cyan).

4.2.4 Relocalization of a Single Identified Cell

To relocate single cells between experiments and on different microscopes, a relocalization routine was developed in close collaboration with the group of *Holger Erfle*[116][129]. In total, two different approaches have been used. In the first approach, three reference structures, being small pieces of titan coated glass with a central circular hole of 400 µm in diameter, were fixed on the sample and imaged in brightfield mode. The central positions in x and y of these holes were determined by applying an automated *Otsu* threshold[130] and calculating the centroid of the resulting area. The z position was taken by the position of the piezo of the objective after applying the autofocus routine. Based on this reference points, an orthonormal basis was generated with one defined reference point as origin. Low-magnification widefield images and their positions on the stage in x, y and z were recorded. Individual cells of interest were selected for further analysis. The absolute position of the cells (position of the stage + position within the image) was calculated and transformed into the reference coordinate system. By repeating the referencing routine on a different microscope and stage, the reference coordinate system can be transformed and each individual chosen cell can be relocated in the field of view. The repositioning of the sample occurs with a precision down to 4 µm (adopted from *Flottmann et al.*[116]).

In the second approach, the whole area of interest (or sample well) was imaged with low resolution widefield microscopy as an overview image. The sample was transferred to the microscope of choice and three randomly selected cells and their respective positions were recorded. These images were compared to the previously recorded overview image by a scale invariant feature transform (SIFT) registration (figure 4.6)[131].

The actual field of view was found on the overview image and the three randomly

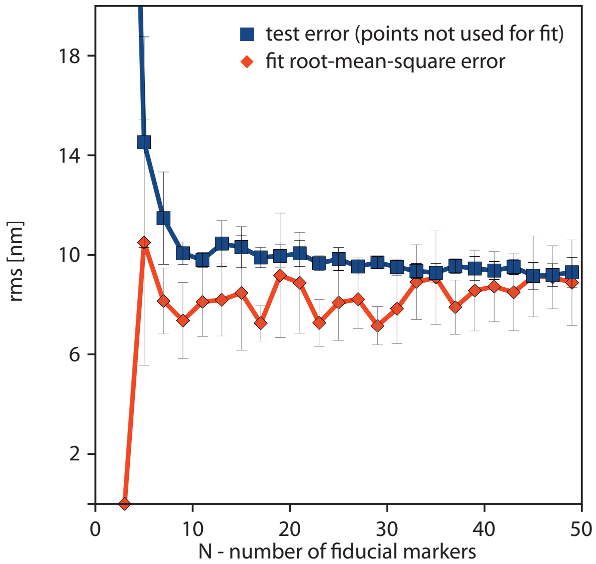

Figure 4.5: Registration of fiducial markers on a surface. The root mean square error does not drop significantly further, if more than 15 beads are used for the linear fit. (adopted from *Schleicher*[126])

chosen cells were used as reference points for a coordinate transformation of the target cell position (figure 4.7)[116][129]. The accuracy of relocalization was 4 µm.

4.3 Verification of the Combined Platform by a Test Sample

To evaluate the microscopy platform, the distribution of two proteins appearing in different cisternae of the Golgi were analyzed after nocodazole and brefeldin A treatment. The samples were prepared as described in chapter 3.2.2. Three different cell treatments were analyzed sequentially by low magnification widefield, confocal and super-resolution microscopy. Individual cells of interest were manually selected out of hundreds of cells from the low magnification images by a biological expert for confocal imaging. The most representative cell was chosen and then imaged by super-resolution microscopy. The three analyzed samples were: 1. control, 2. nocodazole treated cells, 3. Brefeldin A treated cells.

In appendix C, the imaged cells of the widefield low magnification screen and the respective confocal images are shown.

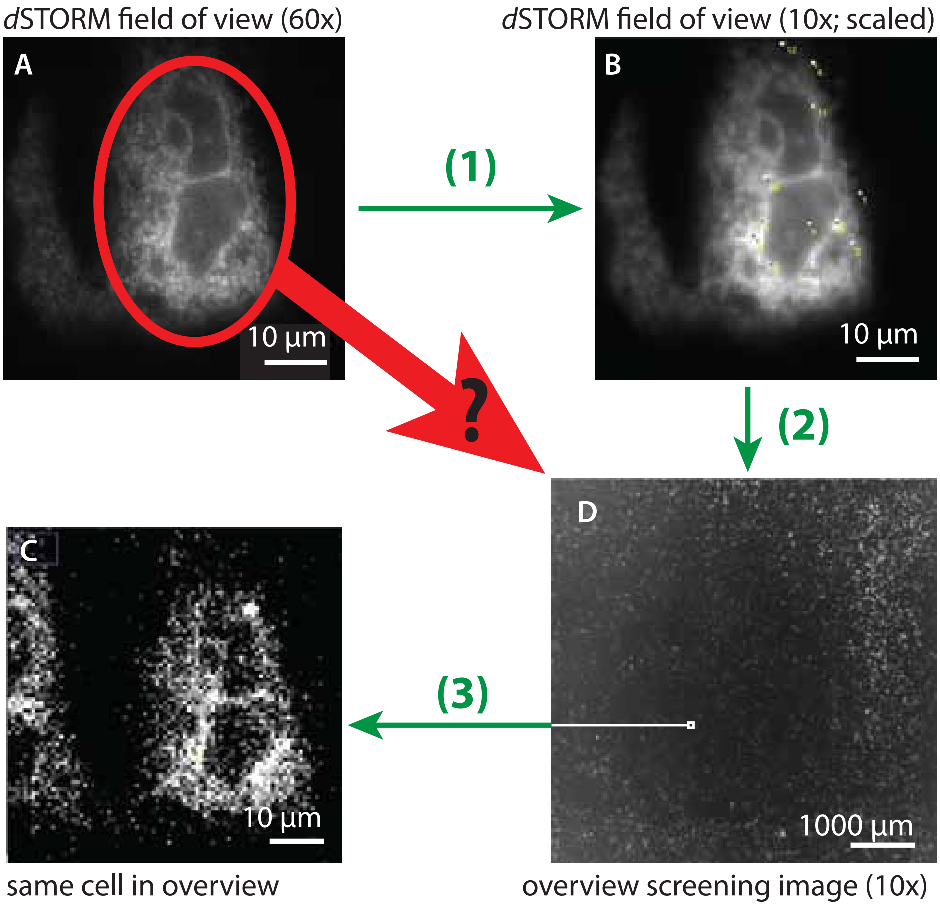

Figure 4.6: SIFT registration for field of view images on an overview image. In the first step, a randomly chosen cell in the field of view of the localization-based microscope (A) is recorded and downscaled to the pixelsize of the overview image (B). The SIFT algorithm locates the downscaled image region in the overview (D) in the second step. (C) shows the enlarged view of the cutout of (D).

One representative cell of each condition was chosen by an expert and imaged in super-resolution microscopy mode. In figure 4.8, a comparison of the confocal and localization-based images is displayed exemplarily, as well as a colocalization analysis of a marked region by ICA.

4.4 Colocalization Analysis

In figure 4.9, the original images and the colocalization analysis of GalT and GM130 in three cells are shown, each treated under a different condition. The distribution of the red and green signal was different for every treatment. In the control (figure 4.9, left

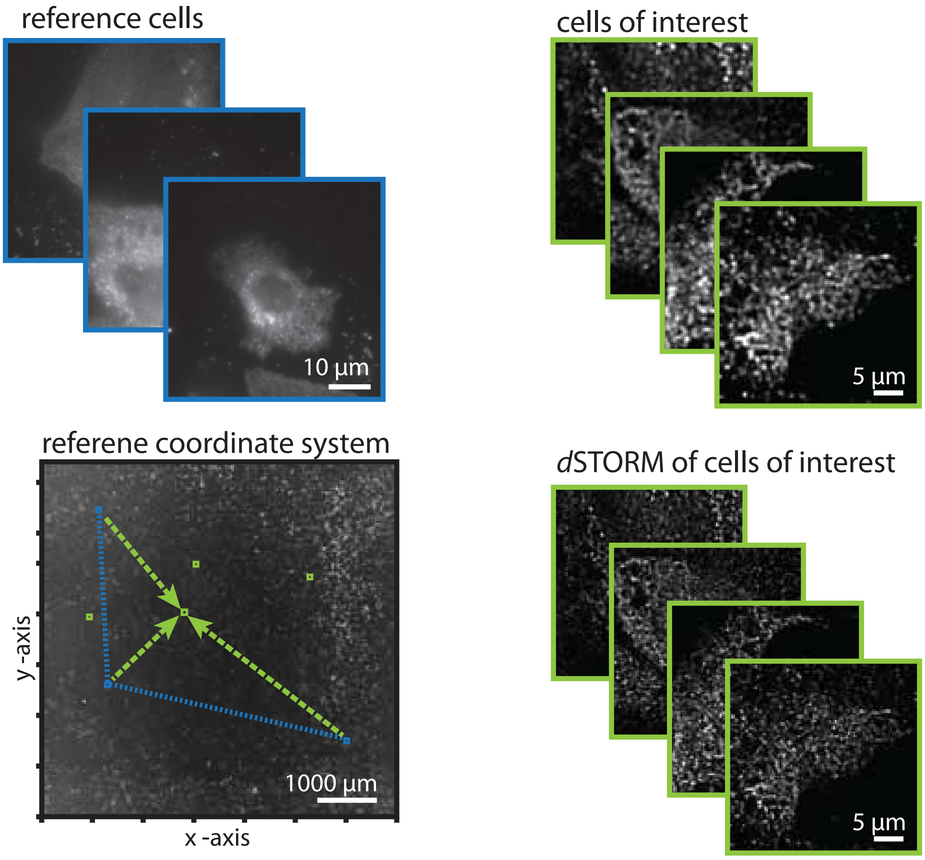

Figure 4.7: Relocalizing of single cells. A set of three randomly chosen cells is imaged on the localization microscope in widefield mode and relocated via SIFT on a previously recorded low magnification overview image. Positions of the stage respective to the cells are used to create a coordinate system. Any selected cell of interest from the overview image can now be moved into the field of view according to the reference coordinate system.

row), large connected areas with rings and holes were visible in the green and the red channel. The structures exhibited comparable distributions, but only small regions of overlap remained. Compared to the confocal image, the super-resolved image showed the same structures but in more detail. For example individual clusters of proteins and smaller holes within the large structures could be recognized.

The treatment of nocodazole changed the distribution of the green and red fluorescence (figure 4.9, right row). Overall more disintegrated and smaller structures of green and red signal with smaller regions of overlap were observed, compared to the control. The fluorescence signal was also recognized at larger distances from the nucleus, compared to the control.

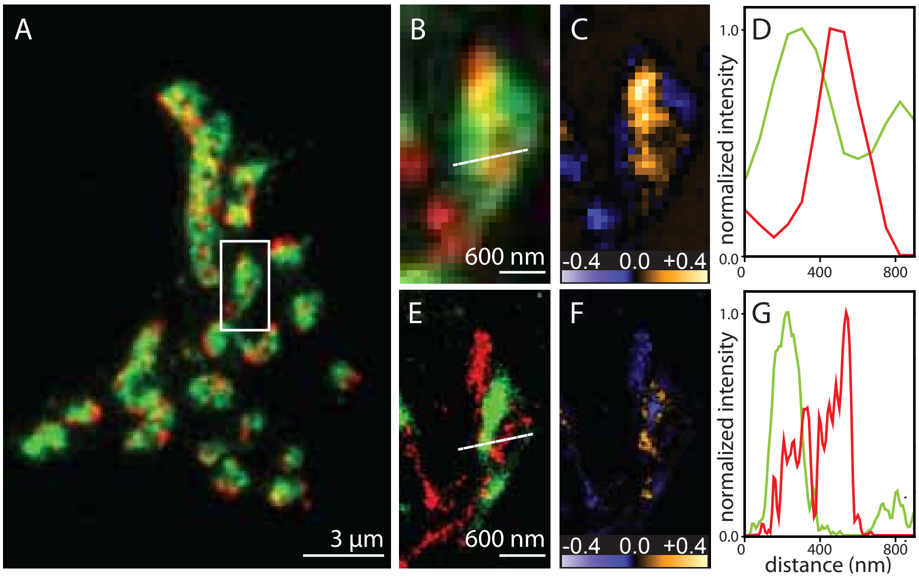

Figure 4.8: (A) Fluorescence images show the distribution of GalT (red) and GM130 (green), recorded on a confocal microscope. The highlighted region is enlarged in (B). (E) displays the same region but recorded on a localization-based microscope. (D) and (G) show the resolution of B and E as line profiles respectively. (C) and (F) display the colocalization pattern of the two proteins, where colocalization is represented by yellow pixels and anticolocalization by blue pixels (see chapter 4.4 for more information). (Extracted from *Flottmann et al.*[116].)

The distribution of the signal of GM130 in brefeldin A treated cells spread over the whole area of the cell. Within the area of the nucleus, the intensity was the lowest. It was strongest at the border to the nucleus and decayed in the direction to the outer cell border. The signal of GalT formed small compartments which were distributed almost randomly within the hole cell but in the nucleus.

4.4.1 Intensity Correlation Analsysis

Colocalization analysis of super-resolution images revealed a higher level of detail in the colocalization. Domains of colocalization (figure 4.9, bottom two rows displayed, in yellow pixels) are smaller as compared to the confocal analysis. The degree of colocalization was measured by the fraction of pixels with positive colocalization values (table 4.1). The control shows higher values for colocalization with 9.6% in the confocal images (5.5% *d*STORM), followed by the Nocodazole treated cell with 7.7% for confocal (4.2% *d*STORM) and brefeldin A at last with 5.5% colocalization in the confocal image (1.6% *d*STORM).

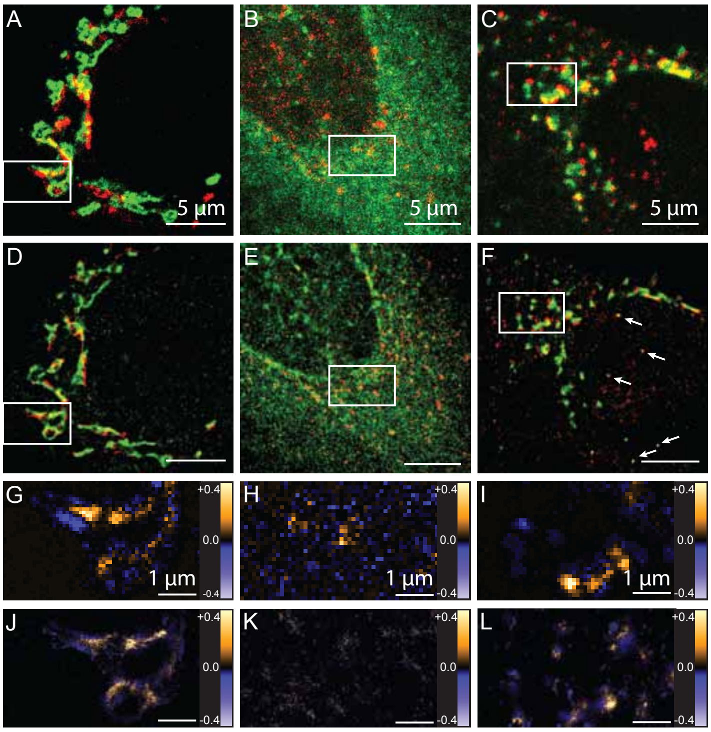

Figure 4.9: Confocal (A - C) and super-resolution (D-F) images of GM130 (red) and GalT (green) in NRK cells (taken from *Flottmann et al.*)[116]. (A, D) control cells, treated with brefeldin A (B, E) and nocodazole (C, F). A small region of these images was analyzed via ICA (see chapter 2.5.5) and is shown in (G) and (J) for the confocal and *d*STORMimage respectively. The chosen cells treated with brefeldin A and nocodazole and their according ICA analysis are shown in (B), (E), (H), (K) and (C), (F), (I) and (L) respectively. Positive values of the ICA images displayed in yellow indicate colocalization. The fraction of pixels showing colocalization for each image is listed in table 4.1. Arrows in (F) point to fluorescent beads used for chromatic aberration correction.

Table 4.1: Colocalization analysis by intensity based correlation analysis (ICA). Values represent the fraction of pixels which contained positive values indicating for colocalization.

	ICA of confocal images (%)	ICA of *d*STORMimages (%)
Control	9.6	5.5
Nocodazole	7.7	4.2
Brefeldin A	5.5	1.6

4.4.2 Coordinate-Based Colocalization Analysis

The same data sets that were investigated with ICA were analyzed with CBC. In contrast to ICA, CBC yields colocalization data for the red and the green channel individually. This gives information whether one protein colocalizes with the second one, whereas the second protein is distributed in another way. This allows conclusions on recruitment dependencies between the two observed proteins. In figure 4.10, the two images obtained by the CBC analysis are shown in comparison to the images analyzed by ICA.

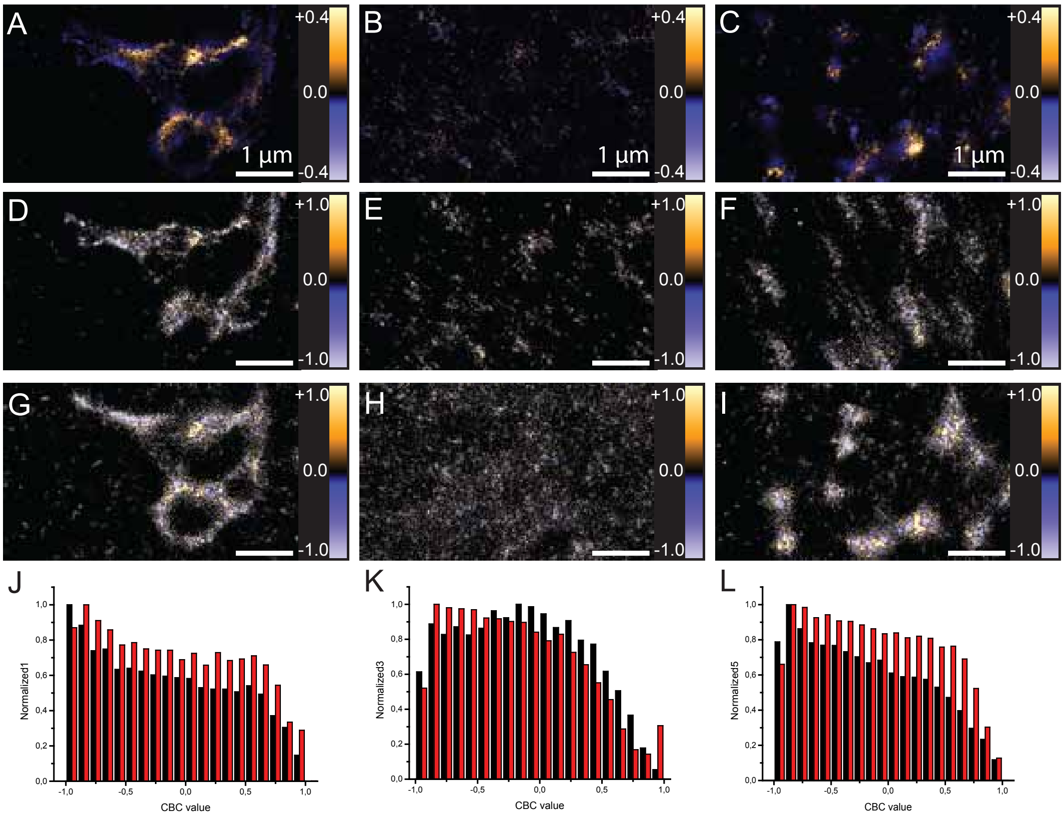

Figure 4.10: Comparison of CBC and ICA analysis of image regions (see figure 4.9). (A) - (C): Region of interest analyzed with ICA for the control (A), brefeldin A (B) and nocodazole (C). (D) - (F): Images of the CBC value distribution of the red channel (control (D), brefeldin A (E), nocodazole (F)). (G) - (I): CBC values of the green channel respectively (control (G), brefeldin A (H), nocodazole (I)). (J) - (L): Histograms of the CBC values of the respective images above (GalT (black bars) and GM130 (red bars); control (J), brefeldin A (K), nocodazole (L)).

The distribution of the calculated CBC values is displayed separately in histograms for each conditions and the two channels. It can be seen, that the colocalization in control cells and nocodozale-treated cells is almost the same. GalT and GM130 do not tend to colocalize. In the case of brefeldin A, the CBC values of GalT are shifted to more positive values whereas the distribution of GM130 is unaffected.

4.5 3D-*d*STORM

A cylindrical lense with a focal length of 1000 mm was placed between the tube lens and the camera of the OlympusIX81 to induce astigmatism for 3D-*d*STORM. A z-stack of fluorescent microspheres was recorded with 10 nm steps. The corresponding PSF widths in x and y were determined by fitting an elliptical Gaussian function (chapter 2.5.3) and were plotted against the z-position (figure 4.11). The ratio of the width in x to the width in y at different z-values yielded a calibration curve(figure 4.11B).

Microtubules were labelled via immunostaining with Alexa Fluor 647 and imaged with localization microscopy. Microtubule structures are well characterized in super-resolution microscopy and are often used to characterize the setup or method. Due to their elongated thin structures, crossings of two tubules exhibit a hint on the quality of the super-resolution raw data: if the crossings show no detection inbetween two tubules, the raw-data are of high quality (appendix A, figure 4.11).
For every detected localization, the z position was determined by fitting an elliptical Gaussian function. The z position was assigned to the respective localization and a 3D-*d*STORMimage was reconstructed with the axial position color-coded for a range of 600 nm (figure 4.11) with a $\sigma_{SMLM} = 63.8$ nm in z.

4.6 Discussion

A microscopy platform combining widefield screening microscopy with confocal and single-molecule localization microscopy for high-throughput experiments was successfully setup and charactarized optically.
A pair of organic dyes was identified, which can be imaged sequentially in widefield screening, confocal and super-resolution imaging by the *d*STORM-method. In collaboration with the group of *Holger Erfle*, a general workflow and relocalization routine to recover the field of view of individual cells of interest on a coveslip sample between different setups and experiments was developed[116][129]. The new software *SimpleSTORM* and *ColorComposer* were implemented in collaboration with the group of *Fred Hamprecht*, and allowed analyzing the *d*STORM raw data and reconstructing super-resolution images, as well as correcting for chromatic aberration[126][127]. Finally, the platform was validated by a small scale screening experiment in collaboration with the groups of *Holger Erfle* and *Vytaute Starkuviene*. Herein, the distribution of a cis- and a trans-Golgi protein GalT and GM130 and their colocalization patterns after treatment with nocodazole and brefeldin A were analyzed[116].

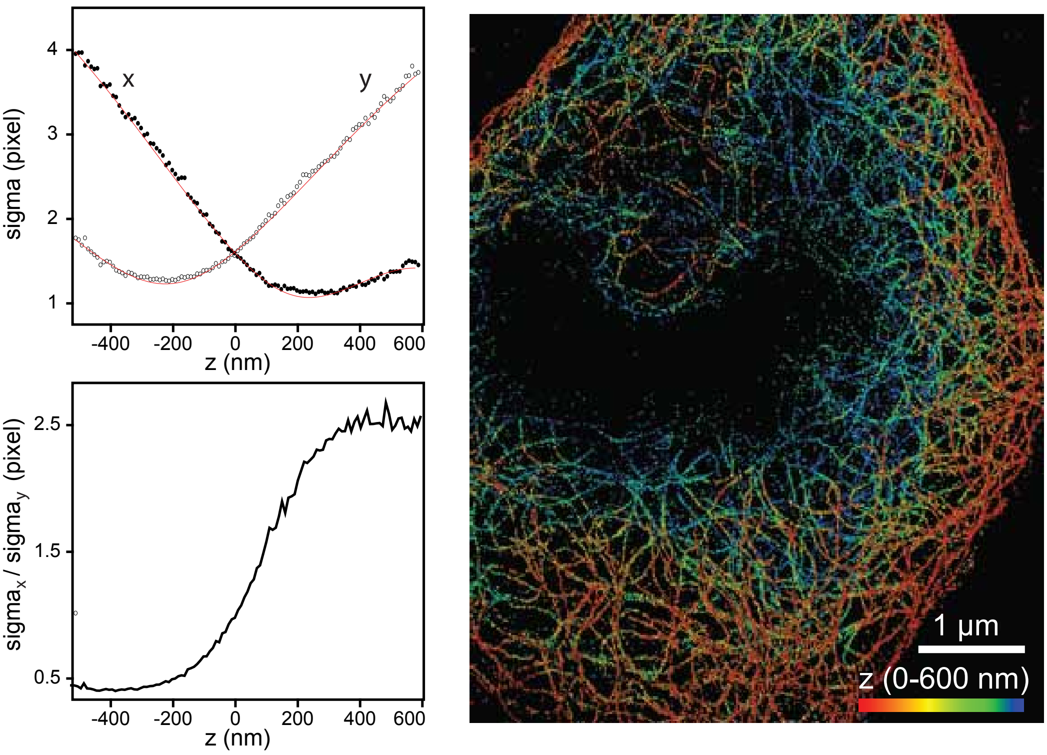

Figure 4.11: 3D-*d*STORM imaging by astigmatism. The PSF width in x and y of fluorescent microspheres are plotted against the z-value (A) and yield a calibration curve for z-position determination (B). Microtubules of HeLa cells were imaged and reconstructed to yield a 3D super-resolution image (C). The image is color-coded at a range of 600 nm along the z-axis.

In the following section, the individual steps of the development of the high-throughput high-resolution microscopy platform are discussed in more detail.

4.6.1 Suitable Dyes for the Combined Platform

In the field of super-resolution microscopy, a large variability of dyes which can be operated in localization-based microscopy mode is described (chapter 2.5.2)[62][63]. However, not all dyes are suitable for consecutive widefield-, confocal- and super-resolution imaging, because some are in a non-fluorescent state. These dyes have to be transformed into the fluorescent form first for conventional microscopy, but then the photoswitching properties cannot be used for localization-based super-resolution microscopy. On the other hand, it is not possible to apply super-resolution microscopy first, because the dyes are usually photobleached after a single-molecule experiment.

Another important demand on the fluorophores used for large screening experiments is their reliability from experiment to experiment. For the platform developed in this work, they also have to be photostable enough to enable data acquisition in sequential widefield, confocal and localization-based microscopy. This includes furthermore, that the dye stays in its bright, fluorescent state before the sample is imaged with localization-based microscopy. By adding the imaging buffer, the dye can then be operated as a photoswitch. The sample preparation of a genome wide screen on a micro-well cell array is relatively expensive. Hence the labelling should be standardized to avoid sources of errors. Commercially available dyes conjugated to secondary antibodies were tested for photoswitching in the same imaging buffer to allow dual-color super-resolution imaging, because immunolabelling is the main staining protocol for the cell arrays (chapter 2.5.6). Due to the nature of the localization-based microscope (chapter 3.3.1), a sequential imaging routine of a red followed by a blue (green) channel has been chosen.

Alexa Fluor 647 and its homolog Cy5 turned out to be the best photoswitching and currently the most heavily used dye for single-molecule localization microscopy (SMLM)[132]. Similarly, these dyes can be used for widefield and confocal microscopy. Therefore, these dyes were chosen for the red color channel in dual-color experiments.

For the green channel, two options were considered. Although mEos2 works nicely in combination with Alexa Fluor 647/Cy5[114] (see also chapter 2.5.7), it was not chosen here. The reason is, that mEos2 has to be transfected into the cell as a plasmid of a fusion protein. This is either a long-term progress (generation of a stable cell line) or a source of artefacts from over-expression. In addition, the transfection efficiency might vary among cells. mEos2 exhibits a lower relative brightness compared to most organic dyes. It also offers advantages, such as that the green fluorescence can be used for widefield/confocal imaging. Also no artefacts from secondary labelling processes occur. However, the protein is not very photostable and it will bleach fast and then cannot be imaged in the super-resolution mode.

Other alternatives for fluorescent labels are ATTO-dyes (ATTO-tec, Germany). They can be purchased with a functional group for coupling and a conjugation kit, but these dyes have not been considered in this study.

Caged dyes conjugated to secondary antibodies (like those of Aberrior, Germany) were tested, but did not show suitable photoswitching behavior in our experiments. The activation rate was hardly manageable and very fast (leading to large r' values; see chapter 2.5.4 and chapter 3.1.3). Additionally the signal-to-noise ratio was very poor compared to other dyes (like Alexa Fluor488, Alexa Fluor 532 or Alexa Fluor 647/Cy5) and even paFPs (like mEos2 or PAmCherry1). They are also not suitable for preliminary screening experiments due to their initial dark state.

The dyes of the Alexa Fluor series (Invitrogen, USA) are available with many different reactive groups for conjugation, as well as conjugated to antibodies. Alexa Fluor dyes are commonly used in SMLM[133] and were also chosen for dual-color imaging. Matching the laser lines of the microscope, three different dyes were selected for dual-color experiments together with Alexa Fluor 647/Cy5: Alexa Fluor488, Alexa Fluor 532 and Alexa Fluor568. The maximum available irradiation intensity of the used setup for Alexa Fluor568 at 568 nm was not sufficient to induce photoswitching. Non-suitable photoswitching was also observed during imaging Alexa Fluor488 conjugated to antibodies. Only Alexa Fluor 532 exhibited photoswitching to enable the data analysis of SMLM. The buffer conditions used for photoswitching also matched those of Alexa Fluor 647/Cy5, which makes these dyes an ideal pair for dual-color super-resolution imaging.

Single and dual-color images were recorded on various samples and the obtained localization precision was determined to $\sigma_{\text{SMLM}} = 12.5\,\text{nm}$ for Alexa Fluor 532 and to $\sigma_{\text{SMLM}} = 7.0\,\text{nm}$ for Alexa Fluor 647/Cy5 (figure 4.3, GM130-Alexa Fluor 532 in NRK cells and α-tubulin-Alexa Fluor 647 in HeLa cells).

It is interesting to note that photoswitching of Alexa Fluor488, when it is conjugated to a heptapeptide (phalloidin) that labels actin, does not require imaging buffers. In addition, lower irradiation densities were sufficient to induce photoswitching, compared to the antibody conjugates. *Nanguneri et al.* demonstrated the underlying mechanism to be based on static quenching of a tryptophan residue within the phalloidin itself[134]. Thus, Alexa Fluor488 can be used in actin associated studies and even allows triple-color super-resolution experiments in combination with Alexa Fluor 647/Cy5 and mEos2 (figure 4.4). In this combination, only the Alexa Fluor 647/Cy5 can be used for widefield/confocal experiments, as the green state of mEos2 and Alexa Fluor488 overlap in their emission spectra.

4.6.2 Correction of Chromatic Aberration

It is crucial to correct for chromatic aberration, if two dyes with different emission spectra are used to discriminate two differently labelled proteins (see chapter 2.5.7). This becomes particularly important when imaging is performed at sub-diffraction resolution. Chromatic aberration not only occurs due to different refraction indices for varying wavelengths. Additionally, the optical elements induce a mismatch in the overlay of two different spectral channels[135]. The method of choice to correct for chromatic aberration was to use fluorescent microspheres (100 nm Tetraspeck, Invitrogen) as fiducial markers. As they do not show blinking during the imaging process and do not change their position within an acquisition, they are constantly fluorescent and are detected as localization in almost every imaging frame.

The *Color-Composer* software, which was developed in collaboration with *Fred Hamprecht* enabled to correct for chromatic aberration with a precision down to 10 nm[126] (figure 4.5). This is below the achieved localization precision and therefore, it is sufficient to correct for chromatic aberration in colocalization analysis.

4.6.3 Relocalizing Cells on Various Microscopes

The reliable relocation of single cells on various microscopes is a crucial step for the high-throughput high-resolution microscopy platform. The approach used in this study relies on a referencing coordinate system. The coordinate system is either based on reference markers derived from external objects next to the sample or on a stitched low-resolution overview image of the entire sample of randomly selected cells.

The external reference markers have to be relocated manually into the field of view. The combination of the position of the stage and the position of the reference structure is taken to generate an arbitrary coordinate system. This coordinate system is accordingly calibrated to the previously generated reference coordinate system.

In case of the low-resolution overview image, this image creates the reference coordinate system. For calibration of a stage, up to three randomly chosen cells are placed into the center of the field of view of the microscope. The position of the stage and the position of the cell in the image are saved and assigned to the position of the cell on the overview reference image.

The achieved relocalization accuracy of a single cell by both methods was determined to be around 4 µm, which is sufficient for cells with an average size of 20-50 µm in diameter and a minimal field of view of roughly 50 x 50 µm^2[116][129].

The second method, where any cell within the overview image can be taken for referencing, is an easy and fast method for calibration of the new microscope, as no specific structure has to be relocated in a manual way. However, sometimes not all areas of the sample are imaged within the low-resolution image, because some areas might be not neseccary for the analysis. In this case, the selected reference cell might not be in the collected data set of the low-resolution images. If the labels in the cells exhibit a weak signal and photobleaching has to be avoided the external referencing is the method of choice.

4.6.4 Small-Scale Screen of Golgi Distribution after Drug Treatment

To verify the performance of the platform, a biological test sample was investigated in a small screen experiment. The distribution of cis- (GM130) and trans- (GalT) Golgi membrane proteins of normal rat kidney cells (NRK) were imaged and analyzed for colocalization. The distribution was checked for changes after treatment with nocodazole and brefeldin A. Colocalization analysis was performed as ICA for confocal and CBC for super-resolution images.

The expected biological phenomen are well described in the literature and were reproduced by the experiments. The Golgi complex itself is a rather compact and highly dynamic system of membrane formed cisternae. Within the secretory pathway, newly synthesized proteins are delivered from the ER to the Golgi complex via vesicles. These vesicles are reorganized within the Golgi complex and prepared for secretion (exocytosis). This function is closely related to the membrane organisation. Perturbations can easily affect the Golgi complex and hinder its natural function. The expected biological phenomena are well described in the literature and were reproduced by the experiments. The Golgi complex itself is a rather compact and highly dynamic system of membrane formed cisternae. Within the secretory pathway, newly synthesized proteins are delivered from the ER to the Golgi complex via vesicles. These vesicles are reorganized within the Golgi complex and prepared for secretion (exocytosis). This function is closely related to the membrane organisation. Perturbations can easily affect the Golgi complex and hinder its natural function. Nocodazole treatment disintegrates the tubulin network. As the Golgi complex is anchored to this network, it will lose its structure. The Golgi complex is expected to fragment into small, circular or spotty structures[136]. Brefeldin A causes a disassembling of the Golgi complex which will then relocate into the ER[137][138][139].

As a future experiment, a large data screen can be performed to observe the same proteins and their colocalization after siRNA-treatment for gene silencing. Some siRNAs are assigned to not show an effect on the protein distributions and act as negative control for gene silencing (for example AllStars). However, these findings have not been analyzed with sub-diffractional resolution, yet. The large screen is supposed to investigate the effects of this control siRNA and several other specific siRNAs on the distribution of the cis- and trans-Golgi proteins.

The known effects of nocodazole and brefeldin A described before, are an ideal control sample to calibrate the platform.

4.6.5 Interpretation

Cells were imaged as described (chapter 3.2.3). Briefly, low resolution widefield images of the three conditions (control, nocodazole and brefeldin A) were recorded for target identification. A subset of 12 cells was chosen for confocal microscopy by a Golgi complex and membrane trafficking expert. Three cells of each condition were imaged with localization-based microscopy. The most representative cell was selected for further investigation by colocalization analysis.

Both treatments (nocodazole and brefeldin A) induced fragmentation of the Golgi Complex (figure 4.9). The individual phenotypes are clearly visible. The control structure forms large and compact membrane layers and cisternae with GM130 and GalT, which occur in close proximity to each other. Both proteins show similar localization patterns. After treatment with brefeldin A, the expected redistribution of the two proteins into the ER is observed. GalT is relocated into the ER and forms a more reticular pattern and GM130 appears at the ER exit sides and occurs as punctuate structures[137][138]. The proteins do not exhibit defined structures and are rather dispersed in the cytosol, where GM130 forms small clusters, whereas GalT does not.
Nocodazole leads to the expected fragmentation of the Golgi complex into smaller compartements. The Golgi complex is anchored to the tubulin network, which gets disrupted when cells are treated with nocodazole. The Golgi then disassembles into smaller fragments[136].
The colocalization measured by ICA decreases from the control over the nocodazole to the brefeldin A treated cells in both, confocal and *d*STORM images. Colocalization occurs at points, where the cis- and trans- membrane of the Golgi are in close distance. When the Golgi disrupts into small structures due to the nocodazol treatment, the continuous structure of this membrane "double layer" becomes smaller and so does the overlap of the two image channels. The colocalization decreases. By disrupting the membrane structure completely, even less colocalization is observed as expected in the case of brefeldin A.

The comparison of the degree of colocalization within one sample but different microscopy techniques shows, that the overlap of fluorescence in both channels is always smaller for the *d*STORM images. This effect can be explained by the higher spatial resolution of the localization-based microscopy. At higher resolution, smaller structures can be resolved. Assuming infinite resolution, no overlap in the two channels would be observed (for two dimensional structures), as the proteins or rather their labels physically cannot be at the same position. In this case the term of colocalization has to be redefined to be independent on pixel intensities. *Gunkel et al.*[76] and *Malkusch et al.*[105] introduced a colocalization definition based on distances between target localizations of two channels (see also chapter 4.4).

ICA analysis is based on intensity distributions, however the *d*STORM images are based on coordinate lists. Depending on the reconstruction method (chapter 3.1.5), the intensity distribution in *d*STORM images varies. However, the coordinates can be analyzed directly by the CBC algorithm. In contrast to ICA, CBC results in two data sets - the first set represents the degree of colocalization of every detected protein A with protein B and the second vice versa. The respective values were plotted in a histogram (figure 4.10).
It turned out that for the control, both GalT and GM130 show mostly anti-correlation. This was identified by more negative CBC values, which means that the two proteins built structures next to each other. This is visible in the similar membrane structures of the respective proteins with always a small distance to each other and hardly any overlap. This matches the fact, that GalT is a trans- and GM130 is a cis-Golgi protein. Partial overlap of the two channels and therefore some colocalization is expected, as the three-dimensional structure of the Golgi is projected onto a two dimensional image.
The addition of nocodazol does not lead to a change in the distribution of histogrammed CBC values. This indicates that, although the Golgi itself is ruptured into smaller individual structures, the original composition of the Golgi membranes is unperturbed. The theory is consistent to this observation, as nocodazol induces the depolimerization of the tubulin network. The Golgi complex is anchored to this network and will lose its structure when detached[136]. The membranes themselves are not affected by nocodazol, and therefore no change in the (co-)localization pattern of GalT and GM130 is expected.
However, adding brefeldin A induces the Golgi to fuse into the ER[138][137]. Within this process, GalT also redistributes into the ER, GM130 relocates at the ER exit sides as being part of the cis Golgi[139]. It was observed to remain in smaller vesicles. The analysis with CBC shows that the CBC values of GalT are shifted to more positive. This change leads to CBC values around 0, which stands for a random distribution. An explanation is, that in the untreated cells, the two proteins are forced to remain at different locations. This driving force is nullified by the treatment, which reassembles the Golgi complex into the ER. Therefore, the remaining proteins diffuse through the cell (and partly build the smaller compartements). Because of this and due to the

projection of a three-dimensional volume onto a two-dimensional image, the two labelled proteins come closer than in their native structure. GalT seems to be evenly distributed within the cytosol, which argues also in favor of the random distribution. In fact, the obtained values for brefeldin A still do not indicate colocalization. Compared to the control and nocodazole treated cells, the Golgi membrane and its cis-trans organization is completely disrupted after brefeldin A treatment.

4.6.6 Super-resolution Imaging in Three Dimensions

3D super-resolution imaging was realized by placing a cylindrical lense into the detection pathway of the OlympusIX81 microscope. The resulting astigmatism was calibrated by recording z-stacks of fiducial markers with a defined axial distance (10 nm). The calibration curve (figure 4.11) shows linearity at a range of 600 nm in z, which corresponds to the observed axial depth of a conventional widefield microscope.

Recording super-resolution microscopy data in 3D (figure 4.11) is more challenging than 2D acquisitions, as the photoswitching kinetics during image acquisition has to be adjusted carefully. In two-dimensional experiments, overlapping PSFs can be excluded depending on their asymmetry to minimize the number of artefacts. Here, the asymmetry accounts for the z-value and cannot be used as a quality feature. In order to image a whole cell in three dimensions, multiple stacks can be recorded. However, the deeper the focal plane is within the sample, the more deforms the PSF due to refractive index changes within the cell and particularly the asymmetric detection of light from just one side of the sample. The usage of an imaging buffer with a higher refractive index such as including glycine is a simple way to enhance the shape of a PSF[140]. Although a microscope using two objectives is ideal to approach an anisotrop data aquisition[52], this setup is sophisticated and the sample preparation is incompatible to the developed microscopy platform.

4.6.7 Perspective

Overall the characterization of the platform and the studies of the distribution of two Golgi marker proteins during a small scale experiment show, that the developed high-throughput high-resolution microscopy platform is fully functional and can be used for the screening of cell arrays.

A disadvantage in super-resolution microscopy is the low throughput as well as the comparable narrow field of view. Therefore, relevant cells might be missed while data acquisition or the imaged cells do not fit the average cell population as the number of observed cells was too low. The combination of screening and super-resolution microscopy allows to comfortably and accurately find the most representing targets in a sample. These targets can then be imaged selectively with super-resolution to yield a characteristic representation of the sample. The microscopy platform allows to perform a highly efficient workflow for the acquisition and characterization of protein distributions and protein-protein interactions on the molecular level for large numbers of various experiments.

5 Single-Molecule Imaging of a Newly Designed Probe for Sequence-Spedific RNA Detection

To understand the life-cycle of a cell and the dynamics within, it is important to know where and when proteins are synthesized. For protein synthesis, DNA is transcribed into mRNA within the nucleus. Most mRNA is then transported into the ER, where it is translated into proteins. The synthesis of proteins is regulated by the concentration of mRNA and varies during a cell cycle. A fast feedback in the up- and down-regulation of protein synthesis is required and therefore, mRNA itself is rather instable and is digested fast by RNAses. As long as the protein is needed, mRNA is continuously produced. When the need of a certain protein runs out, the mRNA synthesis of this protein is stopped. Therefore, the depletion of mRNA has to be efficient and relatively fast, as mentioned above. mRNA depletion is also regulated by certain modifications at the 3' and 5' ends of the mRNA itself by the cell, which extend the lifetime, by the presence of various micro ribonucleid acid (miRNA)s and others.

Several ways of labelling and visualize mRNA distributions within cells were developed. A popular technique is fluorescence in situ hybridization (FISH)[24][25], in which a single-stranded DNA as a probe, is labelled with a fluorophore. The sequence of the DNA is complementary to the sequence of the target (in this case) mRNA, and its length can vary between 20 and several hundreds of nucleotides. The probe will bind to the target mRNA and introduce a fluorophore (figure 5.1, left). A combinatorial labelling of the target sequence by a unique series of individually coloured probe strands leads to a spectral bar-coding of the target sequence and thus enhances specificity in assigning fluorescence signals to the respective mRNA[27].

In order to decrease signals from unbound FISH probes, other structures such as molecular beacons were developed (figure 5.1, middle)[26]. Single-stranded oligodeoxyribonucleotide (ODNs) have one end linked to an oxazine dye and the other end carrying guanosine residues (originally a blackhole quencher (BHQ)). Starting from the dye-labelled end, the sequence of the ODN consists of the recognition sequence, a small sequence for a loop and at last the complementary sequence of the recognition sequence. In its closed loop form, the guanosine residues efficiently quench the fluorophore (oxazine). Upon heating to the melting temperature, the loop will open and the probe binds to existing target sequences. Cooling the system back to room temperature will close all unbound strands. Only probes, that are bound, are fluorescent.

Other labelling techniques rely on adding small sequences into the DNA of the mRNA of interest, which after transcription into mRNA folds into a specific secondary structure. This secondary structure (for example MS2 loops) can be recognized by fluorescently labelled proteins[141][142] or aptamers[143] (figure 5.1, right).

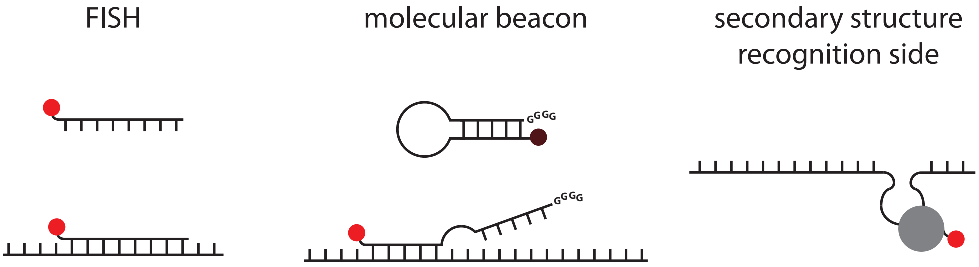

Figure 5.1: Schematics on three ways to label mRNA (from left to right): fluorescence in-situ hybridization (FISH), molecular beacons and label by secondary structure recognition.

Using the described techniques for localization-based microscopy is often challenging, as described in the following.

MS2 loop (secondary structure of mRNA recognized by a labelled protein) based probes are present within the cell at all time and can be distributed in a cellular organelle like the nucleus. However, if the mRNA with MS2 loops is expressed in the nucleus, some of the probes will bind to the recognition sequence of the mRNA, which is then transported out of the nucleus. The fluorescence will accumulate at mRNA localization outside of the nucleus. By using photoswitchable fluorescent proteins this technique could be applied for localization-based microscopy. As the mRNA degrades at a certain point, the MS2 loop binding protein remains and still shows fluorescence. There is no evidence, if the detected signal derives from a probe bound to an mRNA molecule or of a degraded mRNA or unbound protein.

Common FISH probes consist of usually single-stranded DNA and their signals cannot be distinguished between bound and unbound probes. This can be avoided, by using two strands, which bind next to each other on the target mRNA. Each strand is labelled with a dye, and these dyes represent a FRET pair. By exciting the donor dye, the acceptor dye emits light and is detected. The obtained is specific; however it is rather weak and therefore not suitable for super-resolution localization-based microscopy.
The drawback of spectral bar-coding of mRNA is the use of multiple dyes which block channels to label other proteins and molecules of interest. In addition, the mRNA need to be linearized in order to identify the specific bar-code. This can be realized by compressing cells between coverglass slips, but such treatments may destroy spatially complex samples[27].

In a collaboration with *Andriy Mokhir*, a new probe for mRNA detection was developed. This probe consists of two individual oligodeoxyribonucleotide strands (ODN1 and ODN2) binding to the target sequence in close proximity (similar to the FRET probes mentioned above). To combine high specificity and a bright label, one strand is labelled with a fluorescent dye and connected to a quencher via a cleavable linker. The second strand carries a metal complex, which upon radiation with far red light ($<$600 nm) generates singlet oxygen which then cleaves the quencher.
Because of the intrinsic on-switching mechanism, this probe does not need any additional chemicals as used in (d)STORM and it is compatible to localization-based microscopy techniques and can be extended to multi-color experiments.

5.1 Experimental Outline

In a first proof of principle, a simplified version of this probe was designed to investigate the cleaving mechanism. ODN1 was covalently bound to the metal complex (InPPa). On ODN2, the fluorescent dye was attached to the DNA strand via a cleavable linker. As a target, the mRNA was replaced by its respective DNA sequence (see figure 5.2). The target DNA was immobilized to a glass surface via a BSA-Biotin-Streptavidin construct and analyzed on a microscope.

5.1.1 Current State of Research

Subrata Dutta (member of the group of *Andriy Mokhir*) synthesized ODN1 and ODN2 to target a fragment of β-actin. Here, the ODN2 was labelled with fluorescein. Due to internal quenching of fluorescein by nucleobasis (especially guanine), its fluorescence quantum yield was lowered by a factor of 5.4 compared to the free dye. Upon hybridization of ODN1 and ODN2 to the complementary sequence, the fluorescence of fluorescein drops down by another 50%, which results in a 10.7 fold reduction of the quantum yield compared to the free dye.

Illumination of the hybridized probe with red light generates singlet oxygen to cleave the linker. This recovers the fluorescence intensity of the dye. The InPPa complex hereby accelerates the reaction rate of $^1O_2$-induced cleavage by a factor of 7.3 compared to the situation when a probe in which no catalyst is present. The addition of glutathione in physiological concentrations of 5 mM reduces the fluorescence recovery (rate) by a factor of 3.4, as glutathione can act as a $^1O_2$ scavenger. (Adapted from *Dutta et al.*[144].)

Cleaving Mechanism

ODN1 is a short oligodeoxyribonucleotide (ODN), whose 3'-terminus is modified with an In^{3+} (pyropheophorbide-a)-chloride complex[145][146] (InPPa, figure 5.2). Upon illumination with light of 400 nm or 640 nm, this metal complex is an efficient catalyst for singlet oxygen ($^1O_2$) generation. ODN2 is an ODN with its 5'-terminus connected to a fluorophore via a $^1O_2$ sensitive linker (-SCH=CHS-[147], figure 5.2). Both probes bind to the complementary DNA/RNA so that InPPa and the fluorophore are within a short distance. As InPPa acts as a quencher itself, no fluorescence is observed after binding. When InPPa is irradiated with red light, it will catalytically produce $^1O_2$, which then will cleave the linker via a $2 + 2$ addition to -SCH=HCS- (figure 5.3)[148]. This adduct is instable and will decompose to formic acid thioesters, which are (further) hydrolyzed to thiols in the presence of water[149]. After photocleavage, the fluorophore diffuses away from the quencher and starts to fluoresce.

5.1.2 Single-molecule Experiments

Single-molecule experiments on surfaces shall confirm the ensemble findings, and evaluate whether their approach is compatible with *d*STORM[144]. For that purpose, the target sequence (DNA) was immobilized onto a coverslip by BSA-Biotin-Streptavidin, which allows the system to freely rotate in solution[150]. Then the two probe strands were hybridized to the target sequence.

Although the dye is partially quenched when both ODN strands are bound to the mRNA, a weak fluorescence signals was still observed on single-molecule surfaces. Upon TIR illumination, only dyes that are in close proximity to the surface were observed. As soon as a dye is cleaved (off), it will diffuse out of the excitation area.

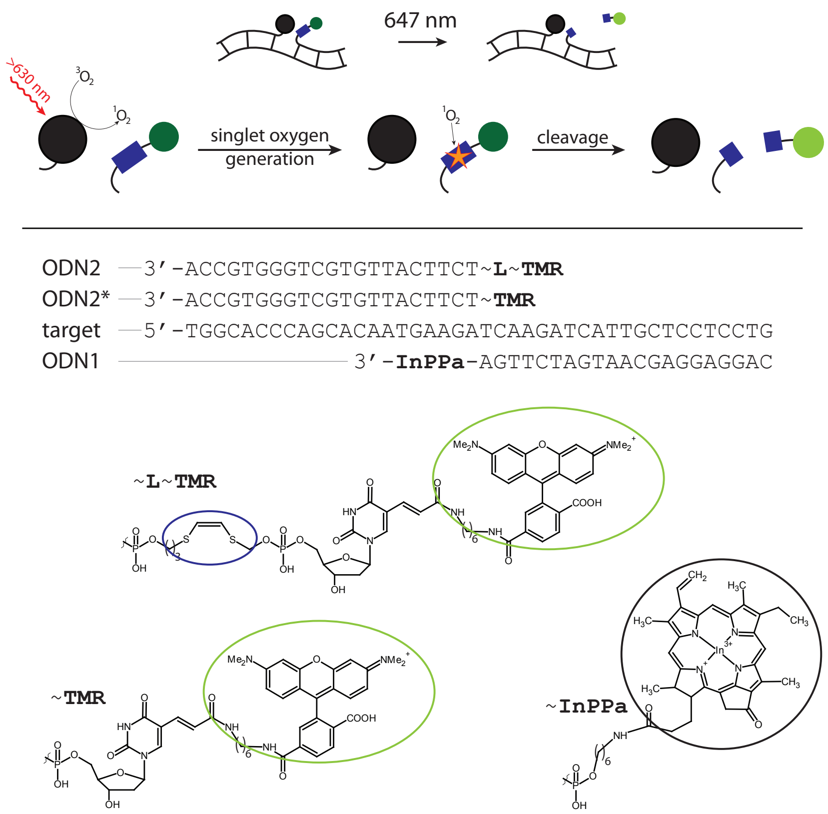

Figure 5.2: Mechanism of the designed RNA-binding probe and chemical structures of individual strands and substituents. Top: Two DNA strands bind to the target RNA within close distance. The fluorophore (green) is conjugated via a cleavable linker (blue) to one strand, the metal complex (black) acts as a quencher and produces singlet oxygen upon red light illumination. Singlet oxygen cleaves the linker and fluorescence is observed. Bottom: Sequences of individual probes and chemical structures of substitutents used to characterize the system within this work (∼L: Linker, ∼TMR: tetramethylrhodamine, ∼InPPa: In^{3+} (pyropheophorbide-a)-chloride complex)[144].

Within this work, the performance for single molecule microscopy experiments was validated. Hereby, fluorescein was replaced by *N*,*N*,*N'*,*N'*-tetramethyl rhodamine (TMR), which exhibits a higher quantum yield and photostability and is more suited for super-resolution imaging.

5.2 Results

The recorded movies have been analyzed with the (open source) software rapidSTORM[123] (see chapter 3.1.5). The number of detected localizations in the field of view was tracked

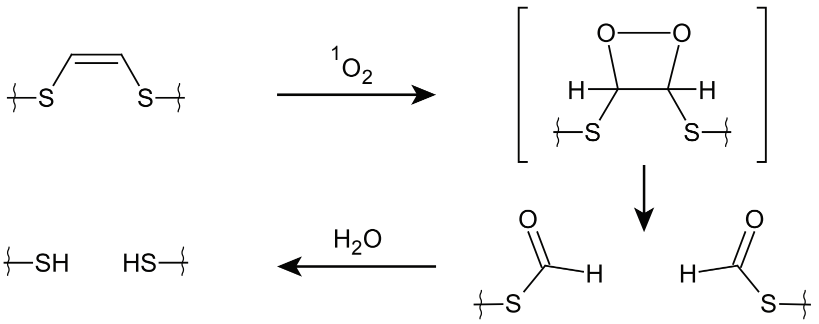

Figure 5.3: Cleavage mechanism of -SCH=HCS- fragment (linker) through singlet oxygen[148]

over time and is displayed in figure 5.4. A total of five different conditions were used to investigate the photocleveage behavior. A control sample consisting of ODN1 and ODN2 without red-light-induced photoactivation shows no photocleveage. In addition, this data exhibits that no major bleaching effects can be estimated within the time of observation. Furthermore, no significant decrease in the number of localization could be observed for the following controls: with ODN2 and no ODN1 with and without red-light photoactivation, ODN1 and ODN2 without cleavable linker (ODN2*), and ODN1 contains a mismatch within the sequence (ODN1*) and ODN2. Only the fully functional pair of ODN1 and ODN2 bound to the target sequence together with red light illumination for photoactivation showed a decrease in the number of detected localizations (all traces are shown in figure 5.4). The recorded movies have been analyzed with the (open source) software rapidSTORM[123] (see chapter 3.1.5). The number of detected localizations in the field of view was tracked over time and is displayed in figure 5.4.

A total of five different conditions were used to investigate the photocleveage behavior. A control sample consisting of ODN1 and ODN2 without red-light-induced photoactivation shows no photocleveage. In addition, this data exhibits that no major bleaching effects can be estimated within the time of observation. Furthermore, no significant decrease in the number of localization could be observed for the following controls: with ODN2 and no ODN1 with and without red-light photoactivation, ODN1 and ODN2 without cleavable linker (ODN2*), and ODN1 contains a mismatch within the sequence (ODN1*) and ODN2. Only the fully functional pair of ODN1 and ODN2 bound to the target sequence together with red light illumination for photoactivation showed a decrease in the number of detected localizations (all traces are shown in figure 5.4).

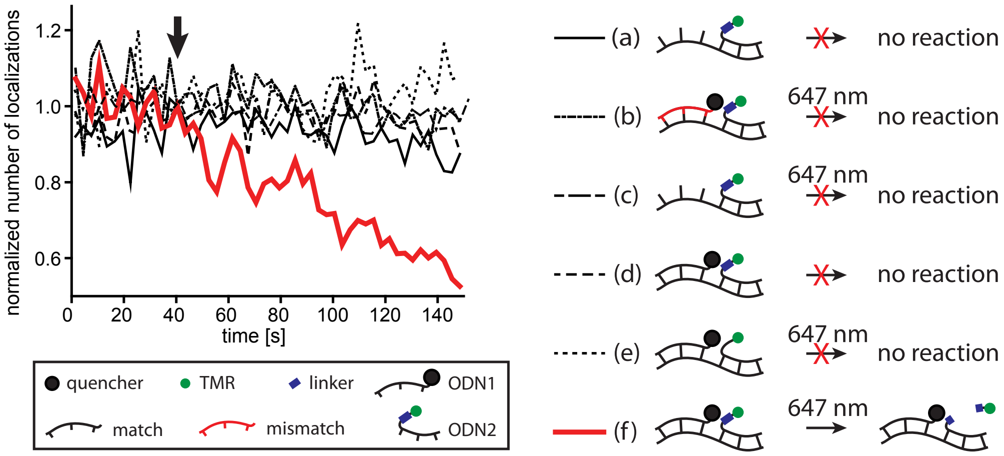

Figure 5.4: Single-molecule imaging of the mRNA probe on a single-molecule surface. The number of detection events is plotted against the time. No decrease in the number of localization was observed for ODN2 only and no red photoactivation (A), mismatch in ODN1 (B), ODN2 only (C), ODN1 and ODN2 without red photoactivation (D) and absence of the cleavable linker (E). A decrease in the number of localizations over time was only seen for the fully functional probe (F). The black arrow indicates the time point, when red-light was applied 40 s after the beginning of the acquisition (adapted from [144]).

5.3 Discussion

Overall, the single-molecule experiments of the designed mRNA probe confirmed the ensemble experiments. To investigate for a selective and specific cleavage of the linker by $^1O_2$, ODN1 and ODN2 were hybridized on the target DNA which was immobilized on a coverslip surface via BSA-Biotin and Streptavidin. Constant excitation of TMR leads to a constant number of detections over time. The excitation power was kept at very low levels to prevent photobleaching (figure 5.4, trace (A)). Keeping this in mind, a decrease in the number of localizations over time is not affected by photobleaching but only by photoactivation, which happens when the fluorophore is released by photocleveage and diffuses away. Due to the TIR illumination, the fluorophore was not observed after release.

In absence of InPPa, the linker remains intact (trace (C)). Also the singlet oxygen generation does not induce any photobleaching of TMR (trace (e)), when no linker is included. Furthermore, no spontaneous activation was observed during a constant excitation of TMR. Only in the complete combination of ODN1 and ODN2 in presence of a matching target sequence and red-light illumination, a release of the fluorophore was observed (trace (F)).

Additionally, the probe is sensitive to a single mutation in the sequence of ODN1 (trace (B), since no reaction in presence of sequence mismatch occurs).

As the fundamental photoswitching mechanism was validated as robust, the probe needs improvement in order to be switching from a dark to a bright state. Therefore, the fluorophore should remain attached to the ODN2, and the quencher should be released. Initial experiments with *Mokhir* and coworkers showed, that the overall cleaving efficiency lies at about 25%, as the linker (-SCH=HCS-) can form a non-cleavable bond (-S(O)CH=HCS-) in a side reaction with $^1O_2$. A more efficient cleavage was observed by using 1,2-dialkoxyanthracene as a cleavable linker[151]. Furthermore, the intensity enhancement between quenched and non-quenched state could be improved by attaching up to three individual fluorophores to ODN2[152]. In a next step, the probe will be investigated in cells.
However, a diffusing fluorophore within the sample cannot be localized due to movement-based asymmetry in the PSF). Additionally, when the fluorophore diffuses away from the labelled mRNA, its localization gives no evidence on the localization of the target DNA/mRNA.
In the end, the novel probe design combines two advantages for localization-based microscopy: first, it shows high specificity due to the two-strand approach; second, it is intrinsically photoactivatable and therefore no redox-buffers are required for imaging. As organic dyes are used as fluorescence reporters, the probe is expected to emit a high number of photons and therefore yield a high localization precision.

6 Conclusion and Outlook

In this work, the single-molecule super-resolution technique *d*STORM was integrated into a high-throughput fluorescence microscopy platform. For this purpose, two microscope setups for single-molecule super-resolution microscopy were set up. A standard protocol for two-color photoswitching of single fluorophores, suitable for single-molecule super-resolution microscopy, was established. Three-dimension super-resolution imaging through astigmatic point-spread functions was set up. A nanometre-precise image registration protocol was established, as well as colocalization analysis based on single-molecule coordinates.

The choice of fluorophores and labelling strategies was optimized for the three imaging techniques. This required that the fluorophores can be used in a regular mode, but also operated in a photoswitching mode by adding redox buffers. In addition, the fluorophores should exhibit a high level of photostability and high molecular brightness. The labelling protocol was optimized for dense labelling, to fulfil the Nyquist-Shannon criterium. Subsequent low-resolution screening, high-resolution confocal and super-resolution *d*STORM imaging was demonstrated. A newly developed position referencing procedure was implemented to relocalize individually selected cells into the field of view on various microscopes. The microscopic platform was validated by the acquisition of a small scale screening experiment of the cis- and trans-Golgi proteins GM130 and GalT. The distribution of the proteins in the different microscopy modes, and the colocalization were analyzed.

The high-throughput high-resolution microscopy platform which was developed in this work is highly modular, which makes the experiment flexible in choosing the desired detection method. The identified combination of dyes and in addition the relocalization procedure allows using any other microscope with a digital position read-out. The initial low-resolution high-throughput screen generates an overview image for target identification, and enables targeted imaging in the confocal and/or super-resolution mode. Targeted imaging - i.e. target identification by low-resolution data for high-resolution data recording - accelerates the acquisition of relevant high-resolution data, and minimizes the generation of "junk-data" data. This is important in case of low transfection rates of cells, or in dense samples with a rare phenotype of interest. In contrast to random imaging of cells, the recorded data of a targeted screen only contain relevant data.

3D-super-resolution was implemented for super-resolution microscopy by placing a cylindrical lens into the detection pathway of the OlympusIX81 TIRF microscope (chapter 3.3.2). The z-level of the detected PSFs can be determined by its asymmetry[55] (figure 4.11). The resolution in z can be assigned to 63.8 nm.

To extend the platform to three-color super-resolution imaging, a combination of the fluorophores Alexa Fluor 647/Cy5, mEos2 and AlexaFluor488 was established. However, AlexaFluor488 did only show suitable photoswitching when attached to phalloidin, which is likely to be related to facilitated electron transfer because of the vicinity to a tryptophan residue (chapter 4.2.1, figure 4.4 and *Nanguneri et al.* 2014[134]). Higher excitation powers than those avaible in this work ($> 5\,\mathrm{kW/cm^2}$) might allow suitable photoswitching of Alexa Fluor 488-antibody conjugates in the *d*STORM imaging mode. As an alternative configuration of fluorophores, Alexa Fluor 647/Cy5 and Alexa Fluor 488 can also be imaged in the low-resolution screening and confocal mode. As a further alternative, the fluorescent protein mEos2 was found to be particularly well suited. Its green-fluorescent, original (non-switched, chapter 2.5.3) form can be recorded in the screening and confocal mode. In the subsequent super-resolution experiment, the mEos2 can be photoconverted with UV light, and fluorescence read-out occurs upon excitation with 568 nm light. As mEos2 is prone to photobleaching and exhibits a lower molecular brightness than many organic dyes, this procedure has to be carried out carefully.

To this point, the target identification during the validation of the integrated platform was performed semi-automatic. A low-resolution image was acquired in a first step and then used for the identification of relevant cells for high-resolution imaging. Target identification was carried out by a biological expert in the small-scale screen, but was also realized automatically by an identification algorithm implemented in *KNIME*[14][129].

Software solutions like *KNIME* or *Micropilot*[16] allow for automated online target identification and subsequent software-controlled image acquisition with for instance higher resolution. To realize a fully automated platform, a confocal microscope (TCS SP5 II, Leica, Germany) was modified to be capable of widefield illumination and detection. This allows low-resolution screening, as well as super-resolution imaging by *d*STORM in one color[129]. Although the individual methods were demonstrated to work on the modular platform, a combined platform simplifies the installation of a fully automated high-throughput high-resolution microscopy platform. The next step is to establish a software-controlled *d*STORMacquisition. However, automated super-resolution imaging is still challenging, because of the heterogeneity in fluorophore densities, illumination

properties and photoswitching kinetics between individual image acquisitions of different cells.
Although the super-resolution imaging method implemented in this platform is not suitable for live-cell imaging, imaging at different time points or end-point analysis can be carried out. For end-point analysis, cells are grown and images are acquired until a phenotype of interest appears. At a specific time, the sample is fixed, eventually stained for proteins of interest, and transferred onto the super-resolution microscope for further analysis of protein distributions at the nanoscale.

The development of a new mRNA probe was advanced by confirming a selective photocleavage at the single-molecule level. The experiment showed that the two-strand approach is highly specific to a single mismatch between target and probe strand. No thermal activation or singlet-oxygen-induced photobleaching of the fluorophore was observed during data acquisition.
The results of the two-strand approach demonstrate the power of this probe compared to common FISH-probes with only one strand directly linked to a fluorophore. The controlled activation by UV light allows a gated read-out of the signal, and similar to single-molecule localization microscopy, the generation of a nano-map of mRNA loci in cells. No special imaging buffer is needed for the temporally confined read-out. Therefore, photoswitchable fluorescent proteins which are affected by these buffers are an option for multi-color experiments. Due to the general quenching mechanism applied, the fluorophorecan be replaced to a variety of others with different fluorescence spectrum. Dual-color mRNA visualization can be realized by using two different fluorophores and the same probe design, i.e. the same activation light. Image acquisition has to be carried out simultaneously, as both probes are activated.
Although the probe is designed to be photoactivatable for single-molecule super-resolution microscopy, it can be used for labeling of mRNA in widefield and confocal studies. In this case, the probe has to be photoactivated quantitatively prior to imaging. This results in a fluorescence intensity distribution which represents the distribution of the targeted mRNA. Although in this case, the intrinsic photoactivation is lost for super-resolution imaging, the fluorophore itself can be chosen to be suitable for subsequent super-resolution microscopy in combination with a switching buffer. Following this strategy, the novel probe can be introduced as a specific marker for mRNA into the microscopy platform.

The demand of systems biology on large amounts of data to describe cellular processes under a holistic point of view can be addressed with a new tool, which is this modular high-throughput high-resolution microscopy platform. This can even be combined with the new type of mRNA probe, to investigate processes involving mRNA at the single-molecule level.

A Photoswitching for Localization-based Microscopy

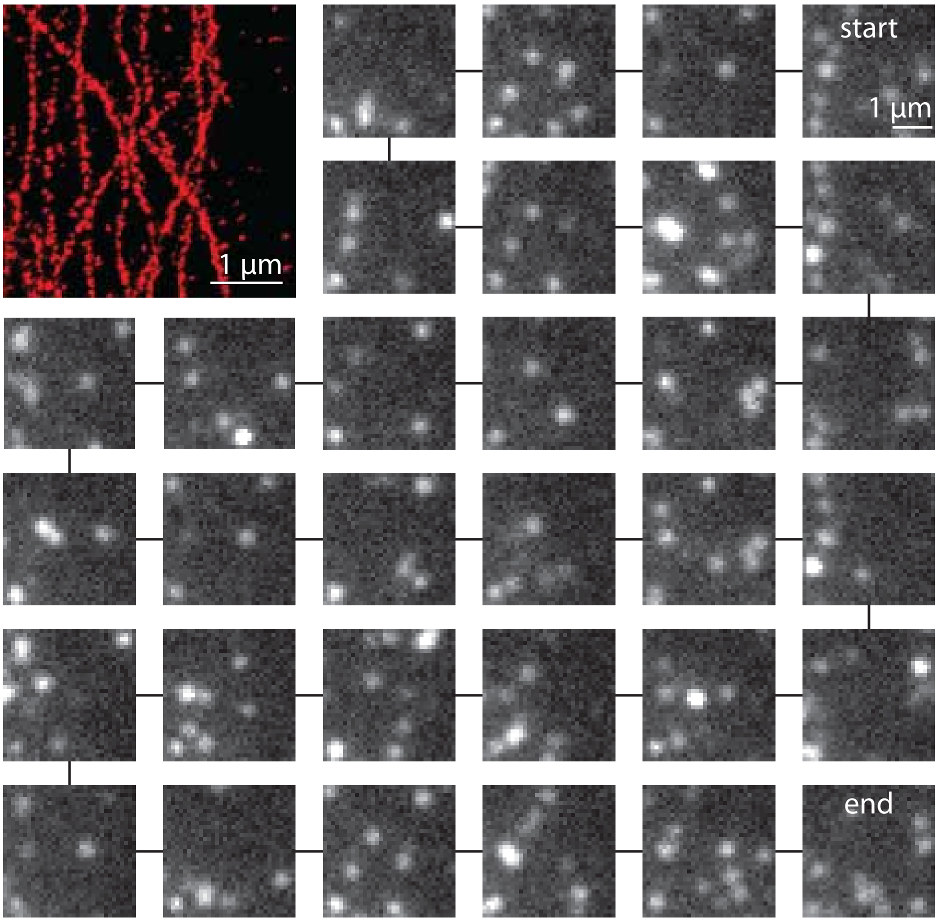

Figure A.1: Optimal photoswitching of the fluorophore AlexaFluor647 in a localization-based microscopy experiment. The PSFs of individual fluorophores have a high signal to noise ratio, are symmetrical and largely do not overlap. The resulting reconstructed image of tubulin structures is shown in the top left, a cut-out of a respective image series is shown in the grey scale images.

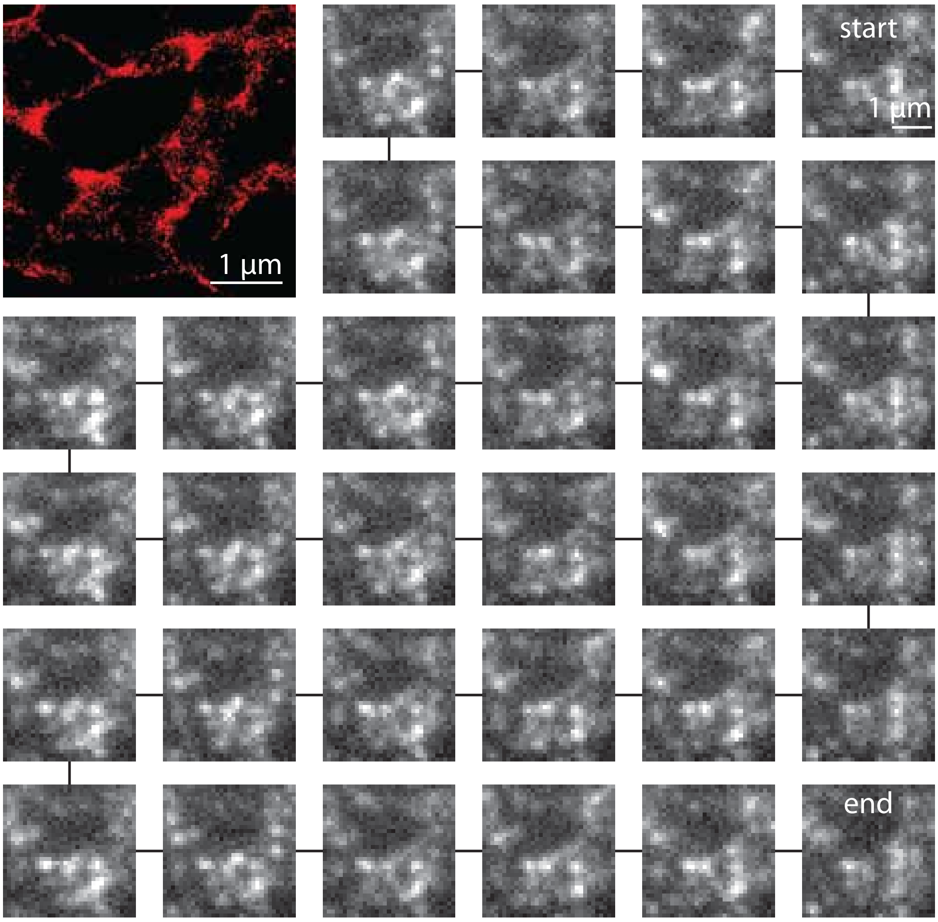

Figure A.2: Non-optimal photoswitching of fluorophores in a localization-based microscopy experiment. Here the PSFs of individual fluorophores have a low contrast, individual signals strongly overlap. As a result the reconstructed image (top left) does not clearly resolve individual tubulin structures but shows webbing at intersections[153]. To enhance acquisition, higher excitation powers and less activation powers might be used. The integration time might be reduced to better separate individual fluorophores by time.

B List of Antibodies

Table B.1: List of antibodies used in this work.

Primary Antibodies	
Antibody Name (Order Number)	Company
α-Tubulin rabbit mAb (2125S)	New England Biolabs GmbH
Rabbit polyclonal to GFP (ab6556)	Abcam
mouse anti-β-tubulin (322600)	Life Technologies
Calnexin pAb, rabbit (ADI-SPA-860-F)	Enzo Life Science
Secondary Antibodies	
Alexa Fluor 647 GaR IgG H+L (A21244)	Life Technologies
Alexa Fluor 532 GaR IgG H+L (A11009)	Life Technologies
Alexa Fluor 647 GaM IgG H+L (A21242)	Life Technologies
Alexa Fluor 532 GaM H+L (A11017)	Life Technologies
AlexaFluor488 phalloidin (A12379)	Life Technologies, Germany

C High-Throughput Images of the Golgi

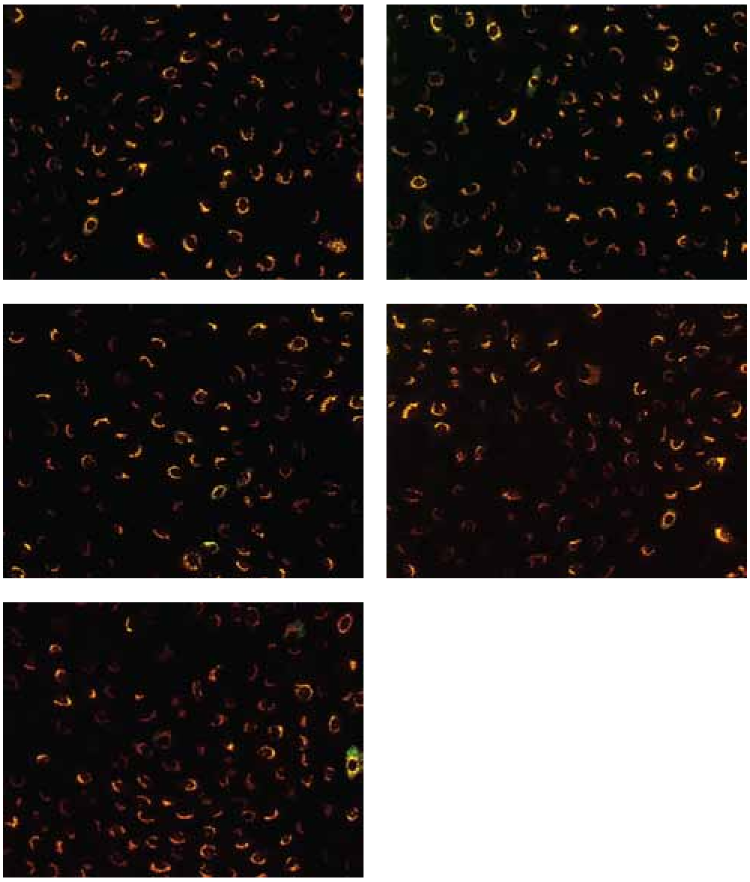

Figure C.1: Low magnification images of non-treated HeLa cells in the control sample. GM130 (red) and GalT (green) in normal rat kidney cells were acquired with an Olympus IX81 microscope with a 10 x objective lens (Olympus UPlanSApo, NA 0.4, Japan) and a field of view of 866 µm x 660 µm. The sample was illuminated by an 150 W Hg/Xe mixed gas arc burner together with appropriate filter combinations for DAPI, Alexa Fluor 532, and Alexa Fluor 647, respectively. Integration times were set to 200 ms (20 ms for DAPI staining), which were the best match to the dynamic range of the CCD camera.

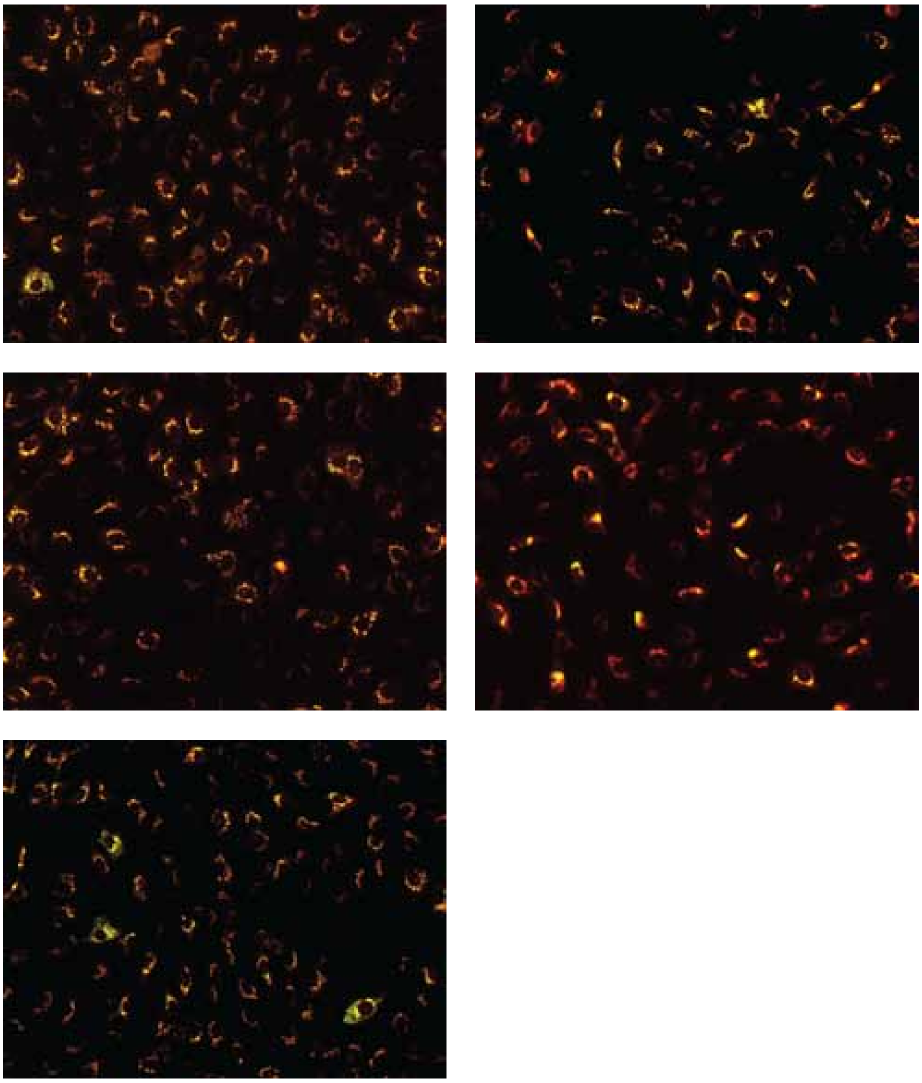

Figure C.2: Low magnification images of nocodazole treated HeLa cells. GM130 (red) and GalT (green) in normal rat kidney cells were acquired with an Olympus IX81 microscope with a 10 x objective lens (Olympus UPlanSApo, NA 0.4, Japan) and a field of view of 866 µm x 660 µm. The sample was illuminated by an 150 W Hg/Xe mixed gas arc burner together with appropriate filter combinations for DAPI, Alexa Fluor 532, and Alexa Fluor 647, respectively. Integration times were set to 200 ms (20 ms for DAPI staining), which were the best match to the dynamic range of the CCD camera.

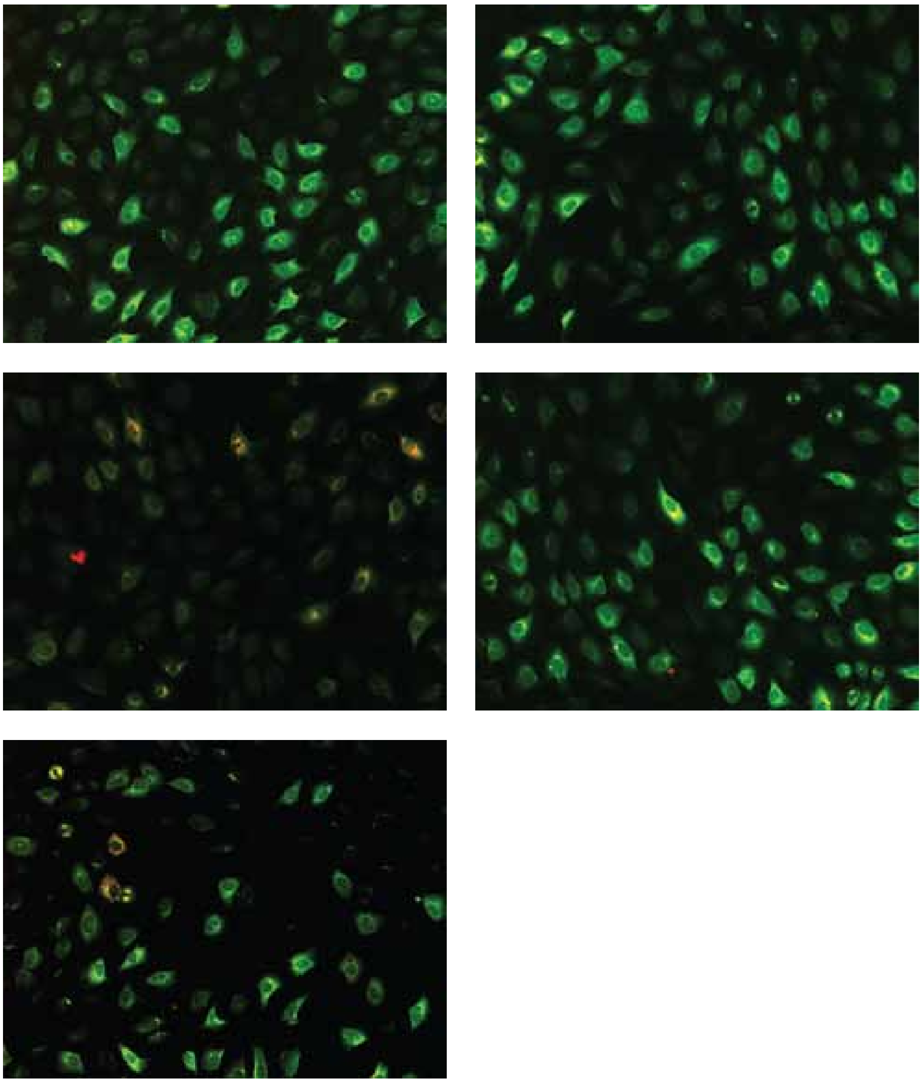

Figure C.3: Low magnification images of brefeldin A treated HeLa cells. GM130 (red) and GalT (green) in normal rat kidney cells were acquired with an Olympus IX81 microscope with a 10 x objective lens (Olympus UPlanSApo, NA 0.4, Japan) and a field of view of 866 µm x 660 µm. The sample was illuminated by an 150 W Hg/Xe mixed gas arc burner together with appropriate filter combinations for DAPI, Alexa Fluor 532, and Alexa Fluor 647, respectively. Integration times were set to 200 ms (20 ms for DAPI staining), which were the best match to the dynamic range of the CCD camera.

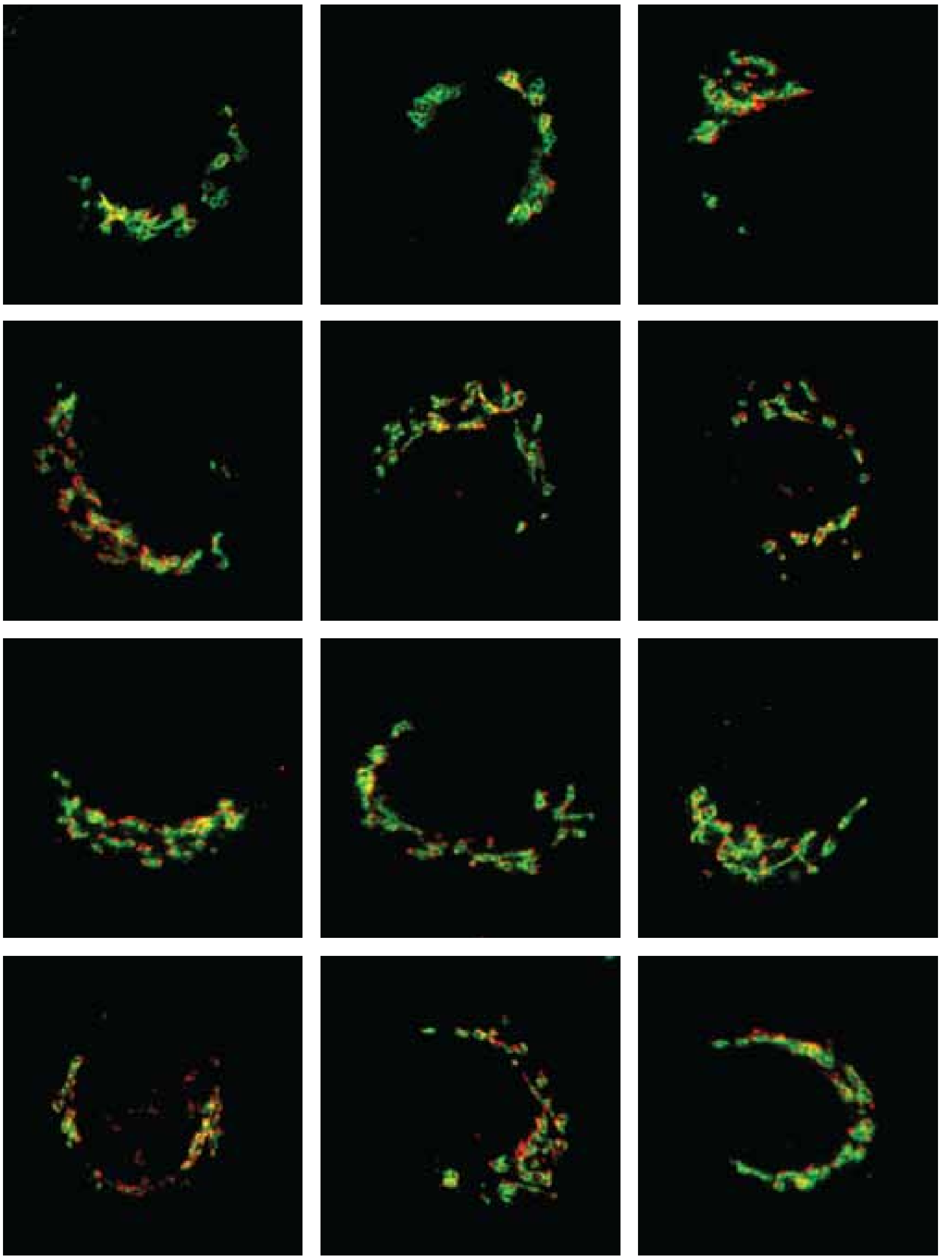

Figure C.4: Confocal images of typical cells of the control sample preselected from the wide-field images. Images of GM130 (red) and GalT (green) in normal rat kidney cells were recorded with the confocal microscope (SP5, Leica, Mannheim, Germany), which is equipped with a 63 x objective lens (Leica HCX PL APO, NA 1.40, Mannheim, Germany). The scanning frequency was set to 400 Hz at 512 x 512 pixels and with a pixel size of 69 nm, resulting in a field of view of 49 µm x 49 µm (pinhole diameter of 96 µm). For each cell, 47 image planes with an axial distance of 0.2 µm were acquired. Selected cells were initially positioned in the center of the z-stack by an autofocus routine before acquisition. Image acquisition took 196 s at each position, subsequent positions could be acquired every 212 s including positioning of the stage and autofocus routines.

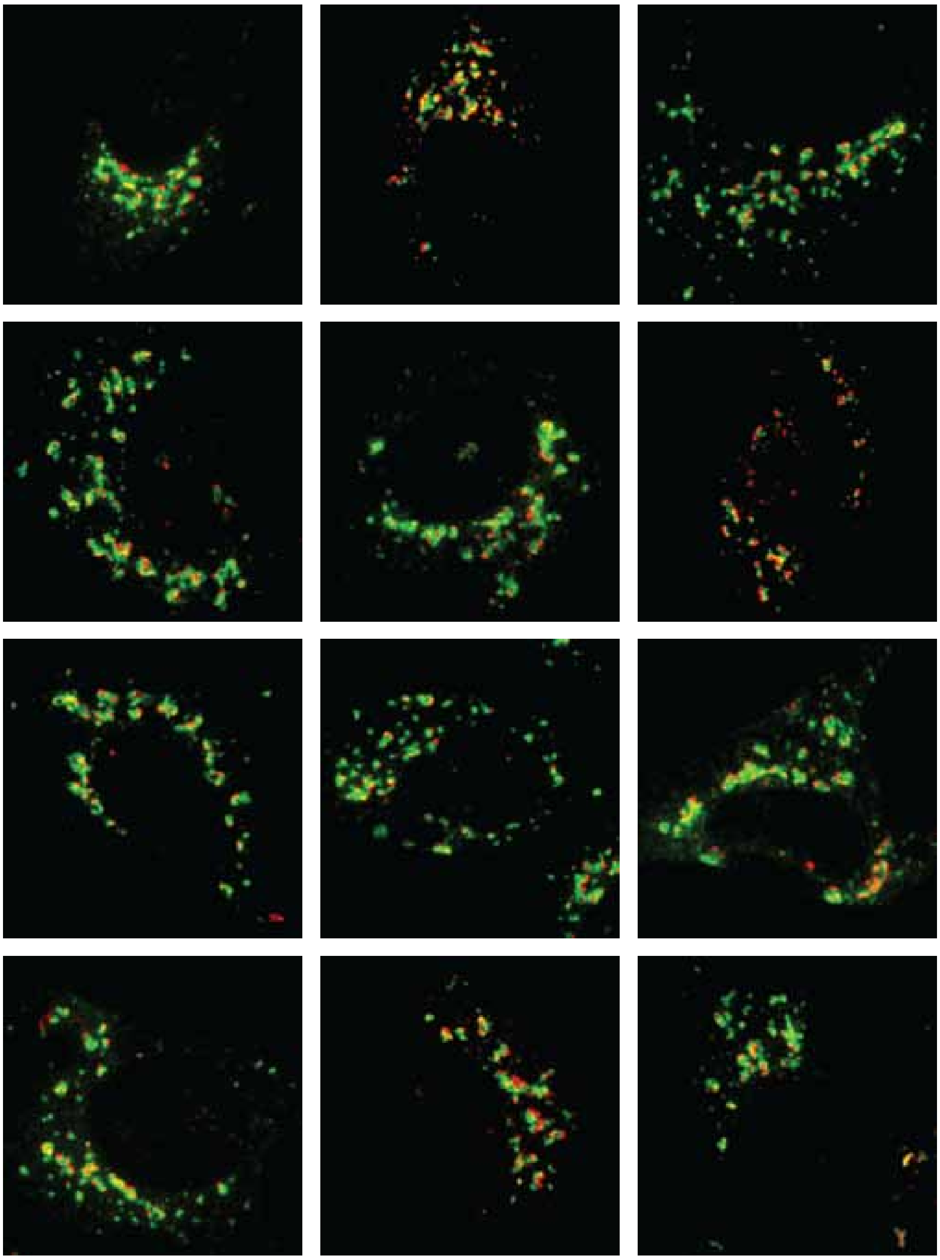

Figure C.5: Confocal images of cells showing the typical phenotype after nocodazole treatment. Images of GM130 (red) and GalT (green) in normal rat kidney cells were recorded with the confocal microscope (SP5, Leica, Mannheim, Germany), which is equipped with a 63 x objective lens (Leica HCX PL APO, NA 1.40, Mannheim, Germany). The scanning frequency was set to 400 Hz at 512 x 512 pixels and with a pixel size of 69 nm, resulting in a field of view of 49 µm x 49 µm (pinhole diameter of 96 µm). For each cell, 47 image planes with an axial distance of 0.2 µm were acquired. Selected cells were initially positioned in the center of the z-stack by an autofocus routine before acquisition. Image acquisition took 196 s at each position, subsequent positions could be acquired every 212 s including positioning of the stage and autofocus routines.

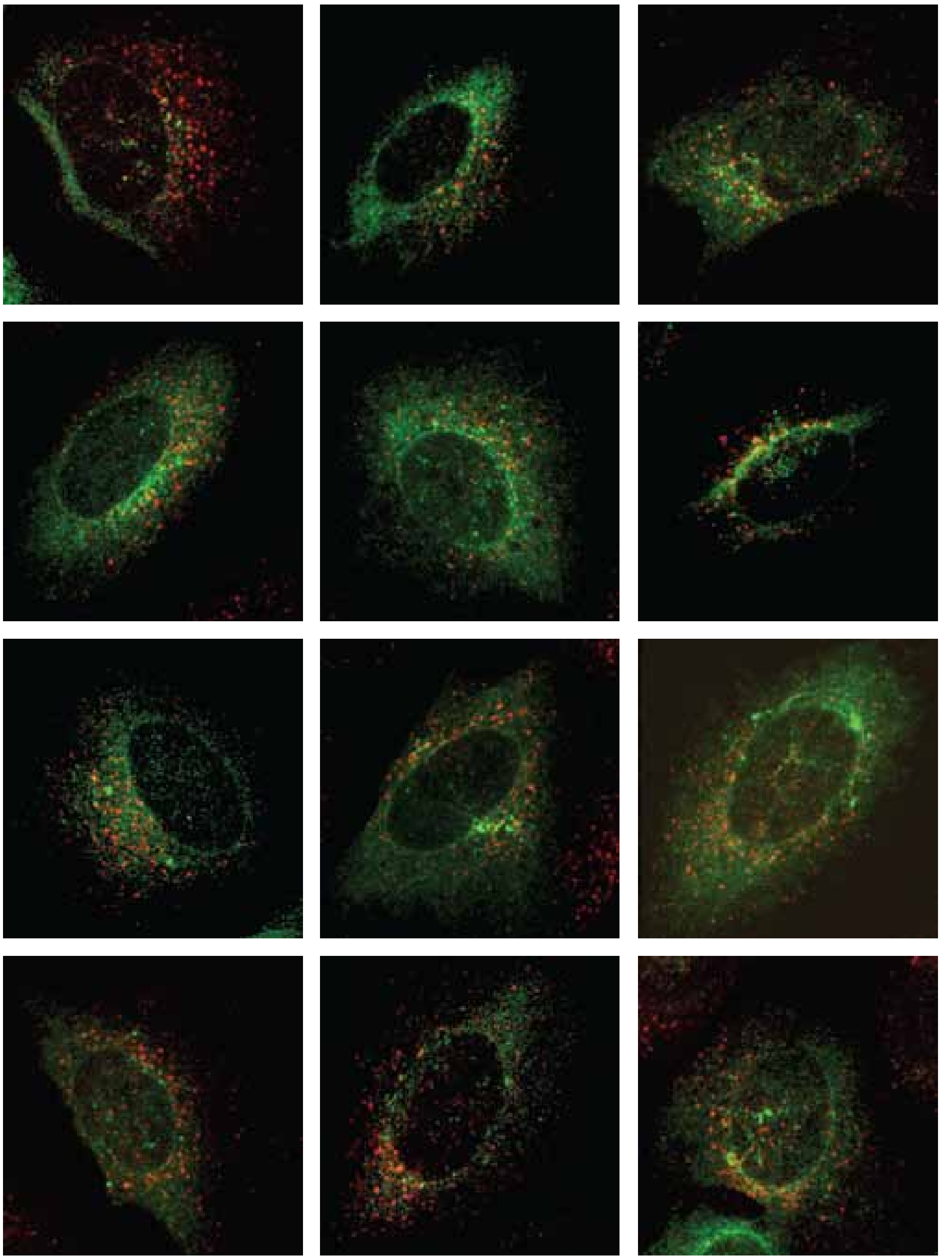

Figure C.6: Confocal images of cells showing the typical phenotype after brefeldin A treatment. Images of GM130 (red) and GalT (green) in normal rat kidney cells were recorded with the confocal microscope (SP5, Leica, Mannheim, Germany), which is equipped with a 63 x objective lens (Leica HCX PL APO, NA 1.40, Mannheim, Germany). The scanning frequency was set to 400 Hz at 512 x 512 pixels and with a pixel size of 69 nm, resulting in a field of view of 49 µm x 49 µm (pinhole diameter of 96 µm). For each cell, 47 image planes with an axial distance of 0.2 µm were acquired. Selected cells were initially positioned in the center of the z-stack by an autofocus routine before acquisition. Image acquisition took 196 s at each position, subsequent positions could be acquired every 212 s including positioning of the stage and autofocus routines.

D Acronyms

AFM	atomic force microscopy
AOTF	acousto-optical tunable filter
AGT	alkyltransferase
APD	avalanche photodiode
BG	benzylguanine
BHQ	blackhole quencher
CBC	coordinate-based colocalization
dSTORM	*direct* stochastic optical reconstruction microscopy
DhlA	dehalogenase
DNA	deoxyribonuleic acid
em	electromagnetic
EMCCD	electron-multiplied charge coupled device
EPR	electron paramagnetic resonance
ER	endosplasmic reticulum
FISH	fluorescence *in-situ* hybridization
FP	fluorescent protein
FPALM	fluorescence photoactivation localization microscopy
GFP	green fluorescent protein
GSDIM	ground state depletion followed by individual molecule return
HILO	highly inclined and laminated optical sheet
HOMO	highest occupied molecular orbital
IC	internal conversion
ICA	intensity-based colocalization analysis

ISC	inter-system crossing
LUMO	lowest unoccupied molecular orbital
ME	β-mercaptoethanol
MEA	β-mercaptoethylamine
miRNA	micro ribonucleid acid
mRNA	messenger ribonulceic acid
NA	numerical aperture
NRK	normal rat kidney
NSOM	nearfield scanning optical microscopy
ODN	oligodeoxyribonucleotide
paFP	photoactivatable fluorescent protein
paGFP	photoactivatable green fluorescent protein
PALM	photoactivated localization microscopy
PALMIRA	PALM with independently running acquisition
PBS	phosphate-buffered saline
PBS*	phosphate-buffered saline; + 1 M NaCl; oxygen removed
PMT	photomultiplier tube
PSF	point-spread function
RNA	ribonucleic acid
sCMOS	scientific complementary metal oxyde semiconductor
SIFT	scale invariant feature transform
SIM	structured illumination microscopy
siRNA	small interfering ribonucleic acid
SMLM	single-molecule localization microscopy
SSIM	saturated structured illumination microscopy
SPDM	spectral precision distance microscopy
STED	stimulated emission depletion
STORM	stochastic optical reconstruction microscopy
TIR	total internal reflection

TMR	tetramethyl rhodamine
UV	ultra violet

Bibliography

[1] J. Lippincott-Schwartz, N. Altan-Bonnet und G. Patterson, Photobleaching and photoactivation: following protein dynamics in living cells, *Nature Cell Biology* **Suppl.** (2003), S7–14.

[2] B. N. G. Giepmans, S. R. Adams, M. H. Ellisman und R. Y. Tsien, The Fluorescent Toolbox for Assessing Protein Location and Function, *Science* **312** (2006)(5771), 217–224.

[3] L. Pelkmans, E. Fava, H. Grabner, M. Hannus, B. Habermann, E. Krausz und M. Zerial, Genome-wide analysis of human kinases in clathrin- and caveolae/raft-mediated endocytosis, *Nature* **436** (2005)(7047), 78–86.

[4] M. N. Krishnan, A. Ng, B. Sukumaran, F. D. Gilfoy, P. D. Uchil, H. Sultana, A. L. Brass, R. Adametz, M. Tsui, F. Qian, R. R. Montgomery, S. Lev, P. W. Mason, R. A. Koski, S. J. Elledge, R. J. Xavier, H. Agaisse und E. Fikrig, RNA interference screen for human genes associated with West Nile virus infection, *Nature* **455** (2008)(7210), 242–245.

[5] F. Bartz, L. Kern, D. Erz, M. Zhu, D. Gilbert, T. Meinhof, U. Wirkner, H. Erfle, M. Muckenthaler, R. Pepperkok und H. Runz, Identification of Cholesterol-Regulating Genes by Targeted {RNAi} Screening, *Cell Metabolism* **10** (2009)(1), 63 – 75.

[6] B. Neumann, M. Held, U. Liebel, H. Erfle, P. Rogers, R. Pepperkok und J. Ellenberg, High-throughput RNAi screening by time-lapse imaging of live human cells, *Nature Methods* **3** (2006)(5), 385–390.

[7] M. Boutros, A. A. Kiger, S. Armknecht, K. Kerr, M. Hild, B. Koch, S. A. Haas, H. F. A. Consortium, R. Paro und N. Perrimon, Genome-Wide RNAi Analysis of Growth and Viability in Drosophila Cells, *Science* **303** (2004)(5659), 832–835.

[8] B. D. Blakeley, A. M. Chapman und B. R. McNaughton, Split-superpositive GFP reassembly is a fast, efficient, and robust method for detecting protein-protein interactions in vivo, *Mol. BioSyst.* **8** (2012), 2036–2040.

[9] R. Pepperkok und J. Ellenberg, High-throughput fluorescence microscopy for systems biology, *Nat Rev Mol Cell Biol* **7** (2006)(9), 690–696.

[10] J. Ziauddin und D. M. Sabatini, Microarrays of cells expressing defined cDNAs, *Nature* **411** (2001)(6833), 107–110.

[11] Reymann, Jürgen and Beil, Nina and Beneke, Jürgen and Kaletta, Peter-Paul and Burkert, Klaus and Erfle, Holger, Next-generation 9216-microwell cell arrays for high-content screening microscopy, *BioTechniques* **47** (2009)(4), 877–878.

[12] B. Neumann, T. Walter, J.-K. Heriche, J. Bulkescher, H. Erfle, C. Conrad, P. Rogers, I. Poser, M. Held, U. Liebel, C. Cetin, F. Sieckmann, G. Pau, R. Kabbe, A. Wunsche, V. Satagopam, M. H. A. Schmitz, C. Chapuis, D. W. Gerlich, R. Schneider, R. Eils, W. Huber, J.-M. Peters, A. A. Hyman, R. Durbin, R. Pepperkok und J. Ellenberg, Phenotypic profiling of the human genome by time-lapse microscopy reveals cell division genes, *Nature* **464** (2010)(7289), 721–727.

[13] C. Conrad, A. Wunsche, T. H. Tan, J. Bulkescher, F. Sieckmann, F. Verissimo, A. Edelstein, T. Walter, U. Liebel, R. Pepperkok und J. Ellenberg, Micropilot: automation of fluorescence microscopy-based imaging for systems biology, *Nat Meth* **8** (2011)(3), 246–249.

[14] KNIME.com AG, *Konstanz Information Miner*, KNIME.com AG, Zurich, Switzerland (http://www.knime.org/) (25.10.2013).

[15] M. V. Boland und R. F. Murphy, A neural network classifier capable of recognizing the patterns of all major subcellular structures in fluorescence microscope images of HeLa cells, *Bioinformatics* **17** (2001)(12), 1213–1223.

[16] C. Conrad, H. Erfle, P. Warnat, N. Daigle, T. Lörch, J. Ellenberg, R. Pepperkok und R. Eils, Automatic Identification of Subcellular Phenotypes on Human Cell Arrays, *Genome Research* **14** (2004)(6), 1130–1136.

[17] P. Ramo, R. Sacher, B. Snijder, B. Begemann und L. Pelkmans, CellClassifier: supervised learning of cellular phenotypes, *Bioinformatics* **25** (2009)(22), 3028–3030.

[18] E. Glory und R. F. Murphy, Automated Subcellular Location Determination and High-Throughput Microscopy, *Developmental Cell* **12** (2007)(1), 7 – 16.

[19] S. Hell und J. Wichmann, Breaking the Diffraction Resolution Limit by Stimulated-Emission - Stimulated-Emission-Depletion Fluorescence Microscopy, *Optics Letters* **19** (1994)(11), 780–782.

[20] T. Mueller, C. Schumann und A. Kraegeloh, STED Microscopy and its Applications: New Insights into Cellular Processes on the Nanoscale, *ChemPhysChem* **13** (2012)(8), 1986–2000.

[21] Betzig, Eric and Patterson, George H. and Sougrat, Rachid and Lindwasser, O. Wolf and Olenych, Scott and Bonifacino, Juan S. and Davidson, Michael W. and Lippincott-Schwartz, Jennifer and Hess, Harald F., Imaging intracellular fluorescent proteins at nanometer resolution, *Science* **313** (2006)(5793), 1642–1645.

[22] Rust, Michael J. and Bates, Mark and Zhuang, Xiaowei, Sub-diffraction-limit imaging by stochastic optical reconstruction microscopy (STORM), *Nature Methods* **3** (2006)(10), 793–795.

[23] M. Heilemann, S. van de Linde, M. Schuttpelz, R. Kasper, B. Seefeldt, A. Mukherjee, P. Tinnefeld und M. Sauer, Subdiffraction-resolution fluorescence imaging with conventional fluorescent probes, *Angewandte Chemie-International Edition* **47** (2008)(33), 6172–6176.

[24] J. B. Lawrence, R. H. Singer und L. M. Marselle, Highly localized tracks of specific transcripts within interphase nuclei visualized by in situ hybridization, *Cell* **57** (1989)(3), 493 – 502.

[25] G. Zhang, K. L. Taneja, R. H. Singer und M. R. Green, Localization of pre-mRNA splicing in mammalian nuclei, *Nature* **372** (1994)(6508), 809–812.

[26] J.-P. Knemeyer, N. Marme und M. Sauer, Probes for Detection of Specific DNA Sequences at the Single-Molecule Level, *Analytical Chemistry* **72** (2000)(16), 3717–3724.

[27] E. Lubeck und L. Cai, Single-cell systems biology by super-resolution imaging and combinatorial labeling, *Nat Meth* **9** (2012)(7), 743–748.

[28] J. R. Lakowicz, *Principles of Fluorescence Spectroscopy*, Springer (2006).

[29] M. Heilemann, *Design of Single-Molecule Optical Devices: Unidirectional Photonic Wires and Digital Photoswitches*, Dissertationsschrift, Universität Bielefeld (2005).

[30] O. Stern und M. Volmer, The fading time of fluorescence, *Physikalische Zeitschrift* **20** (1919), 183–188.

[31] E. Hecht, *Optik*, Oldenbourg Verlag München (2009).

[32] M. Tokunaga, N. Imamoto und K. Sakata-Sogawa, Highly inclined thin illumination enables clear single-molecule imaging in cells, *Nature Methods* **5** (2008)(2), 159–161.

[33] U. Endesfelder, *Quantitative Localization-Based Super-Resolution Microscopy: CConcept and Applications*, Dissertationsschrift, Universität Bielefeld (2012).

[34] E. Abbe, Beiträge zur Theorie des Mikroskops und der mikroskopischen Wahrnehmung, *Arch. Mikroskop. Anat.* **9** (1873), 413–420.

[35] Rayleigh, XV. On the theory of optical images, with special reference to the microscope, *Philosophical Magazine Series 5* **42** (1896)(255), 167–195.

[36] D. B. Murphy, *Fundamentals of Light Microscopy and Electronic Imaging*, Wiley-Liss, Inc. (2001).

[37] A. J. Koster und J. Klumperman, Electron microscopy in cell biology: integrating structure and function, *Nature Reviews Molecular Cell Biology* **Suppl. S** (2003)(Suppl. S), SS6–SS10.

[38] S. W. Hell, Far-field optical nanoscopy, *Science* **316** (2007)(5828), 1153–1158.

[39] E. Betzig, J. K. Trautmann, T. D. Harris, J. S. Weiner und R. L. Kostelak, Breaking the Diffraction Barrier: Optical Microscopy on a Nanometric Scale, *Science* **251** (1991)(5000), 1468–1470.

[40] G. Binnig, C. F. Quate und C. Gerber, Atomic Force Microscope, *Phys. Rev. Lett.* **56** (1986), 930–933.

[41] S. Hell, M. Schrader, K. Bahlman, F. Meinecke, J. Lakowicz und I. Gryczynski, Stimulated-Emission on Microskopic Scale - Light Quenching of Pyridine-2 Using a Ti-Sapphire Laser, *Journal of Microscopy-Oxford* **180** (1995)(Part 2), RP1–RP2.

[42] M. G. L. Gustafsson, Surpassing the lateral resolution limit by a factor of two using structured illumination microscopy, *Journal of Microscopy* **198** (2000)(2), 82–87.

[43] R. Heintzmann, T. Jovin und C. Cremer, Saturated patterned excitation microscopy - a concept for optical resolution improvement, *Journal of the Optical Society of America A-Optics Image Science and Vision* **19** (2002)(8), 1599–1609.

[44] S. T. Hess, T. P. Girirajan und M. D. Mason, Ultra-High Resolution Imaging by Fluorescence Photoactivation Localization Microscopy, *Biophysical Journal* **91** (2006)(11), 4258 – 4272.

[45] A. Egner, C. Geisler, C. von Middendorff, H. Bock, D. Wenzel, R. Medda, M. Andresen, A. C. Stiel, S. Jakobs, C. Eggeling, A. Schönle und S. W. Hell, Fluorescence Nanoscopy in Whole Cells by Asynchronous Localization of Photoswitching Emitters, *Biophysical Journal* **93** (2007)(9), 3285 – 3290.

[46] A. Esa, P. Edelmann, G. Kreth, L. Trakhtenbrot, N. Amariglio, G. Rechavi, M. Hausmann und C. Cremer, Three-dimensional spectral precision distance microscopy of chromatin nanostructures after triple-colour DNA labelling: a study of the BCR region on chromosome 22 and the Philadelphia chromosome, *Journal of Microscopy* **199** (2000)(2), 96–105.

[47] J. Folling, M. Bossi, H. Bock, R. Medda, C. A. Wurm, B. Hein, S. Jakobs, C. Eggeling und S. W. Hell, Fluorescence nanoscopy by ground-state depletion and single-molecule return, *Nat Meth* **5** (2008)(11), 943–945.

[48] S. Hell und E. Stelzer, Fundamental Improvement of Resolution with a 4Pi-Confocal Fluorescence Microscope using 2-Photon Excitation, *Optics Communications* **93** (1992)(5-6), 277–282.

[49] P. Hanninen, S. Hell, J. Salo, E. Soini und C. Cremer, 2-Photon Excitation 4PI Confocal Microscope - Enhanced Axial Resolution Microscope for Biological-Research, *Applied Physics Letters* **66** (1995)(13), 1698–1700.

[50] M. G. L. Gustafsson, D. A. Agard und J. W. Sedat, Sevenfold improvement of axial resolution in 3D widefield microscopy using two objective lenses, *Appl. Phys. Lett.* **66** (1995), 1698–1700.

[51] R. Schmidt, C. A. Wurm, S. Jakobs, J. Engelhardt, A. Egner und S. W. Hell, Spherical nanosized focal spot unravels the interior of cells, *Nat Meth* **5** (2008)(6), 539–544.

[52] K. Xu, H. P. Babcock und X. Zhuang, Dual-objective STORM reveals three-dimensional filament organization in the actin cytoskeleton, *Nat Meth* **9** (2012)(2), 185–188.

[53] G. Shtengel, J. A. Galbraith, C. G. Galbraith, J. Lippincott-Schwartz, J. M. Gillette, S. Manley, R. Sougrat, C. M. Waterman, P. Kanchanawong, M. W.

Davidson, R. D. Fetter und H. F. Hess, Interferometric fluorescent super-resolution microscopy resolves 3D cellular ultrastructure, *Proceedings of the National Academy of Sciences* **106** (2009)(9), 3125–3130.

[54] S. R. P. Pavani, M. A. Thompson, J. S. Biteen, S. J. Lord, N. Liu, R. J. Twieg, R. Piestun und W. E. Moerner, Three-dimensional, single-molecule fluorescence imaging beyond the diffraction limit by using a double-helix point spread function, *Proceedings of the National Academy of Sciences* **106** (2009)(9), 2995–2999.

[55] B. Huang, W. Wang, M. Bates und X. Zhuang, Three-Dimensional Super-Resolution Imaging by Stochastic Optical Reconstruction Microscopy, *Science* **319** (2008)(5864), 810–813.

[56] M. F. Juette, T. J. Gould, M. D. Lessard, M. J. Mlodzianoski, B. S. Nagpure, B. T. Bennett, S. T. Hess und J. Bewersdorf, Three-dimensional sub-100 nm resolution fluorescence microscopy of thick samples, *Nat Meth* **5** (2008)(6), 527–529.

[57] R. Thompson, D. Larson und W. Webb, Precise nanometer localization analysis for individual fluorescent probes, *Biophysical Journal* **82** (2002)(5), 2775–2783.

[58] Basché, T., *Single-Molecule Optical Detection, Imaging and Spectroscopy*, John Wiley & Sons, New York (1997).

[59] U. Endesfelder, S. Malkusch, F. Fricke und M. Heilemann, A simple method to estimate the average localization precision of a single-molecule localization microscopy experiment, *Histochemistry and Cell Biology* (2014), 1–10.

[60] M. Sauer, J. Hofkens und J. Enderlein, *Handbook of Fluresecence Spectroscopy and Imaging: From Single Molecules to Ensemble; From Ensemble to Single Molecules*, Wiley (2011).

[61] H. Kao und A. Verkman, Tracking of single fluorescent particles in three dimensions: use of cylindrical optics to encode particle position, *Biophysical Journal* **67** (1994)(3), 1291 – 1300.

[62] M. Heilemann, S. van de Linde, A. Mukherjee und M. Sauer, Super-Resolution Imaging with Small Organic Fluorophores, *Angewandte Chemie International Edition* **48** (2009)(37), 6903–6908.

[63] G. T. Dempsey, J. C. Vaughan, K. H. Chen, M. Bates und X. Zhuang, Evaluation of fluorophores for optimal performance in localization-based super-resolution imaging, *Nat Meth* **8** (2011)(12), 1027–1036.

[64] G. T. Dempsey, M. Bates, W. E. Kowtoniuk, D. R. Liu, R. Y. Tsien und X. Zhuang, Photoswitching Mechanism of Cyanine Dyes, *Journal of the American Chemical Society* **131** (2009)(51), 18192–18193, pMID: 19961226.

[65] S. van de Linde, I. Krstic, T. Prisner, S. Doose, M. Heilemann und M. Sauer, Photoinduced formation of reversible dye radicals and their impact on super-resolution imaging, *Photochem. Photobiol. Sci.* **10** (2011), 499–506.

[66] T. Kottke, S. van de Linde, M. Sauer, S. Kakorin und M. Heilemann, Identification of the Product of Photoswitching of an Oxazine Fluorophore Using Fourier Transform Infrared Difference Spectroscopy, *The Journal of Physical Chemistry Letters* **1** (2010)(21), 3156–3159.

[67] S. van de Linde, A. Loschberger, T. Klein, M. Heidbreder, S. Wolter, M. Heilemann und M. Sauer, Direct stochastic optical reconstruction microscopy with standard fluorescent probes, *Nat. Protocols* **6** (2011)(7), 991–1009.

[68] S. Doose, H. Neuweiler und M. Sauer, Fluorescence Quenching by Photoinduced Electron Transfer: A Reporter for Conformational Dynamics of Macromolecules, *ChemPhysChem* **10** (2009)(9-10, Sp. Iss. SI), 1389–1398.

[69] O. Shimomura, F. Johnson und Y. Saiga, Extraction, Purification and Properties of Aequorin, a Bioluminescent Protein from Luminous Hydromedusan, Aequorea, *Journal of Cellular and Comparative Physiology* **59** (1962)(3), 223–&.

[70] M. Ormo, A. Cubitt, K. Kallio, L. Gross, R. Tsien und S. Remington, Crystal structure of the Aequorea victoria green fluorescent protein, *Science* **273** (1996)(5280), 1392–1395.

[71] F. Yang, L. Moss und G. Phillips, The molecular structure of green fluorescent protein, *Nature Biotechnology* **14** (1996)(10), 1246–1251.

[72] C. Cody, D. Prasher, W. Westler, F. Prendergast und W. Ward, Chemichal-Structure of the Hexapeptide Chromophore of The Aequorea Green-Fluorescent Protein, *Biochemistry* **32** (1993)(5), 1212–1218.

[73] R. Heim, D. Prasher und R. Tsien, Wavelength Mutations and Posttranslational Autoxidation of Green Fluorescent Protein, *Proceedings of the National Academy of Sciences of the United States of America* **91** (1994)(26), 12501–12504.

[74] A. Cubitt, R. Heim, S. Adams, A. Boyd, L. Gross und R. Tsien, Understanding, Improving and Using Green Fluorescent Proteins, *Trends in Biochemical Science* **20** (1995)(11), 448–455.

[75] P. Dedecker, F. C. De Schryver und J. Hofkens, Fluorescent Proteins: Shine on, You Crazy Diamond, *Journal of the American Chemical Society* **135** (2013)(7), 2387–2402.

[76] M. Gunkel, F. Erdel, K. Rippe, P. Lemmer, R. Kaufmann, C. Hoermann, R. Amberger und C. Cremer, Dual color localization microscopy of cellular nanostructures, *Biotechnology Journal* **4** (2009)(6), 927–938.

[77] P. Lemmer, P., M. Gunkel, Y. Weiland, P. Müller, D. Baddeley, R. Kaufmann, A. Urich, H. Eipel, R. Amberger, M. Hausmann und C. Cremer, Using conventional fluorescent markers for far-field fluorescence localization nanoscopy allows resolution in the 10-nm range, *Journal of Microscopy* **235** (2009)(2), 163–171.

[78] G. H. Patterson und J. Lippincott-Schwartz, A photoactivatable GFP for selective photolabeling of proteins and cells, *Science* **297** (2002)(5588), 1873–1877.

[79] J. N. Henderson, R. Gepshtein, J. R. Heenan, K. Kallio, D. Huppert und S. J. Remington, Structure and Mechanism of the Photoactivatable Green Fluorescent Protein, *Journal of the American Chemical Society* **131** (2009)(12), 4176+.

[80] J. N. Henderson, R. Gepshtein, J. R. Heenan, K. Kallio, D. Huppert und S. J. Remington, Structure and Mechanism of the Photoactivatable Green Fluorescent Protein, *Journal of the American Chemical Society* **131** (2009)(12), 4176+.

[81] K. Nienhaus, U. G. Nienhaus, J. Wiedenmann und H. Nar, Structural basis for photo-induced protein cleavage and green-to-red conversion of fluorescent protein EosFP, *Proceedings of the National Academy of Sciences of the United States of America* **102** (2005), 9156–9159.

[82] F. V. Subach, V. N. Malashkevich, W. D. Zencheck, H. Xiao, G. S. Filonov, S. C. Almo und V. V. Verkhusha, Photoactivation mechanism of PAmCherry based on crystal structures of the protein in the dark and fluorescent states, *Proceedings of the National Academy of Sciences of the United States of America* **106** (2009)(50), 21097–21102.

[83] S. Habuchi, P. Dedecker, J.-i. Hotta, C. Flors, R. Ando, H. Mizuno, A. Miyawaki und J. Hofkens, Photo-induced protonation/deprotonation in the GFP-like fluorescent protein Dronpa: mechanism responsible for the reversible photoswitching, *Photochem. Photobiol. Sci.* **5** (2006), 567–576.

[84] M. Andresen, A. C. Stiel, S. Trowitzsch, G. Weber, C. Eggeling, M. C. Wahl, S. W. Hell und S. Jakobs, Structural basis for reversible photoswitching in Dronpa, *Proceedings of the National Academy of Sciences* **104** (2007)(32), 13005–13009.

[85] S. Habuchi, R. Ando, P. Dedecker, W. Verheijen, H. Mizuno, A. Miyawaki und J. Hofkens, Reversible single-molecule photoswitching in the GFP-like fluorescent protein Dronpa, *Proceedings of the National Academy of Sciences of the United States of America* **102** (2005)(27), 9511–9516.

[86] Ai, Hui-wang and Campbell, Robert E., Teal fluorescent proteins: characterization of a reversibly photoswitchable variant, *Proc. SPIE* **6868** (2008), .

[87] D. M. Chudakov, V. V. Belousov, A. G. Zaraisky, V. V. Novoselov, D. B. Staroverov, D. B. Zorov, S. Lukyanov und K. A. Lukyanov, Kindling fluorescent proteins for precise in vivo photolabeling, *Nat Biotech* **21** (2003)(2), 191–194.

[88] V. Adam, M. Lelimousin, S. Boehme, G. Desfonds, K. Nienhaus, M. J. Field, J. Wiedenmann, S. McSweeney, G. U. Nienhaus und D. Bourgeois, Structural characterization of IrisFP, an optical highlighter undergoing multiple photo-induced transformations, *Proceedings of the National Academy of Sciences of the United States of America* **105** (2008)(47), 18343–18348.

[89] D. Chudakov, V. Verkhusha, D. Staroverov, E. Souslova, S. Lukyanov und K. Lukyanov, Photoswitchable cyan fluorescent protein for protein tracking, *Nature Biotechnology* **22** (2004)(11), 1435–1439.

[90] D. M. Chudakov, S. Lukyanov und K. A. Lukyanov, Tracking intracellular protein movements using photoswitchable fluorescent proteins PS-CFP2 and Dendra2, *Nature Protocols* **2** (2007)(8), 2024–2032.

[91] F. V. Subach, G. H. Patterson, S. Manley, J. M. Gillette, J. Lippincott-Schwartz und V. V. Verkhusha, Photoactivatable mCherry for high-resolution two-color fluorescence microscopy, *Nature Methods* **6** (2009)(2), 153–159.

[92] B. Bevis und B. Glick, Rapidly maturing variants of the Discosoma red fluorescent protein (DsRed), *Nature Biotechnology* **20** (2002)(1), 83–87.

[93] R. Campbell, O. Tour, A. Palmer, P. Steinbach, G. Baird, D. Zacharias und R. Tsien, A monomeric red fluorescent protein, *Proceedings of the National Academy of Sciences of the United States of America* **99** (2002)(12), 7877–7882.

[94] N. Shaner, R. Campbell, P. Steinbach, B. Giepmans, A. Palmer und R. Tsien, Improved monomeric red, orange and yellow fluorescent proteins derived from

Discosoma sp red fluorescent protein, *Nature Biotechnology* **22** (2004)(12), 1567–1572.

[95] S. A. McKinney, C. S. Murphy, K. L. Hazelwood, M. W. Davidson und L. L. Looger, A bright and photostable photoconvertible fluorescent protein, *Nature Methods* **6** (2009)(2), 131–133.

[96] I. Hayashi, H. Mizuno, K. I. Tong, T. Furuta, F. Tanaka, M. Yoshimura, A. Miyawaki und M. Ikura, Crystallographic evidence for water-assisted photo-induced peptide cleavage in the stony coral fluorescent protein kaede, *Journal of Molecular Biology* **372** (2007)(4), 918–926.

[97] H. Tsutsui, S. Karasawa, H. Shimizu, N. Nukina und A. Miyawaki, Semi-rational engineering of a coral fluorescent protein into an efficient highlighter, *EMBO Reports* **6** (2005)(3), 233–238.

[98] V. Adam, K. Nienhaus, D. Bourgeois und G. U. Nienhaus, Structural Basis of Enhanced Photoconversion Yield in Green Fluorescent Protein-like Protein Dendra2, *Biochemistry* **48** (2009)(22), 4905–4915.

[99] H. Mizuno, T. K. Mal, K. I. Tong, R. Ando, T. Furuta, M. Ikura und A. Miyawaki, Photo-Induced Peptide Cleavage in the Green-to-Red Conversion of a Fluorescent Protein, *Molecular Cell* **12** (2003)(4), 1051 – 1058.

[100] T. J. Gould, M. S. Gunewardene, M. V. Gudheti, V. V. Verkhusha, S.-R. Yin, J. A. Gosse und S. T. Hess, Nanoscale imaging of molecular positions and anisotropies, *Nature Methods* **5** (2008)(12), 1027–1030.

[101] V. Adam, B. Moeyaert, C. David, H. Mizuno, M. Lelimousin, P. Dedecker, R. Ando, A. Miyawaki, J. Michiels, Y. Engelborghs und J. Hofkens, Rational Design of Photoconvertible and Biphotochromic Fluorescent Proteins for Advanced Microscopy Applications, *Chemistry & Biology* **18** (2011)(10), 1241 – 1251.

[102] V. Zinchuk, O. Zinchuk und T. Okada, Quantitative Colocalization Analysis of Multicolor Confocal Immunofluorescence Microscopy Images: Pushing Pixels to Explore Biological Phenomena, *ACTA Histochemica et Cytochemica* **40** (2007)(4), 101–111.

[103] Q. Li, A. Lau, T. J. Morris, L. Guo, C. B. Fordyce und E. F. Stanley, A Syntaxin 1, Gao, and N-Type Calcium Channel Complex at a Presynaptic Nerve Terminal: Analysis by Quantitative Immunocolocalization, *The Journal of Neuroscience* **24** (2004)(16), 4070–4081.

[104] D. Baddeley, M. B. Cannell und C. Soeller, Visualization of Localization Microscopy Data, *Microscopy and Microanalysis* **16** (2010), 64–72.

[105] S. Malkusch, U. Endesfelder, J. Mondry, M. Gelleri, P. Verveer und M. Heilemann, Coordinate-based colocalization analysis of single-molecule localization microscopy data, *Histochemistry and Cell Biology* **137** (2012)(1), 1–10.

[106] C. E. Shannon, Communication in the Presence of Noise, *Proc. Institute of Radio Engineers* **37** (1949)(1), 10–21.

[107] A. Keppler, S. Gendreizig, T. Gronemeyer, H. Pick, H. Vogel und K. Johnsson, A general method for the covalent labeling of fusion proteins with small molecules in vivo, *Nat Biotech* **21** (2003)(1), 86–89.

[108] G. V. Los, L. P. Encell, M. G. McDougall, D. D. Hartzell, N. Karassina, C. Zimprich, M. G. Wood, R. Learish, R. F. Ohana, M. Urh, D. Simpson, J. Mendez, K. Zimmerman, P. Otto, G. Vidugiris, J. Zhu, A. Darzins, D. H. Klaubert, R. F. Bulleit und K. V. Wood, HaloTag: A Novel Protein Labeling Technology for Cell Imaging and Protein Analysis, *ACS Chemical Biology* **3** (2008)(6), 373–382, pMID: 18533659.

[109] S. S. Gallagher, J. E. Sable, M. P. Sheetz und V. W. Cornish, An In Vivo Covalent TMP-Tag Based on Proximity-Induced Reactivity, *ACS Chemical Biology* **4** (2009)(7), 547–556, pMID: 19492849.

[110] H. C. Kolb, M. G. Finn und K. B. Sharpless, Click Chemistry: Diverse Chemical Function from a Few Good Reactions, *Angewandte Chemie International Edition* **40** (2001)(11), 2004–2021.

[111] T. Plass, S. Milles, C. Koehler, J. Szymanski, R. Mueller, M. Wiesler, C. Schultz und E. A. Lemke, Amino Acids for Diels-Alder Reactions in Living Cells, *Angewandte Chemie International Edition* **51** (2012)(17), 4166–4170.

[112] A. H. El-Sagheer und T. Brown, Click chemistry with DNA, *Chem. Soc. Rev.* **39** (2010), 1388–1405.

[113] K. Finan, B. Flottmann und M. Heilemann, Photoswitchable Fluorophores for Single-Molecule Localization Microscopy, in A. A. Sousa und M. J. Kruhlak, (Hrsg.), *Nanoimaging*, Band 950 von *Methods in Molecular Biology*, Humana Press (2013), 131–151.

[114] U. Endesfelder, S. Malkusch, B. Flottmann, J. Mondry, P. Liguzinski, P. J. Verveer und M. Heilemann, Chemically Induced Photoswitching of Fluorescent Probe: A

General Concept for Super-Resolution Microscopy, *Molecules* **16** (2011)(4), 3106–3118.

[115] M. Bates, B. Huang, G. T. Dempsey und X. Zhuang, Multicolor Super-Resolution Imaging with Photo-Switchable Fluorescent Probes, *Science* **317** (2007)(5845), 1749–1753.

[116] B. Flottmann, M. Gunkel, T. Lisauskas, M. Heilemann, V. Starkuviene, J. Reymann und H. Erfle, Correlative light microscopy for high-content screening, *Biotechniques* **5** (2013), 243–252.

[117] H. Shroff, C. G. Galbraith, J. A. Galbraith, H. White, J. Gillette, S. Olenych, M. W. Davidson und E. Betzig, Dual-color superresolution imaging of genetically expressed probes within individual adhesion complexes, *Proceedings of the National Academy of Sciences of the United States of America* **104** (2007)(51), 20308–20313.

[118] N. Gurskaya, V. Verkhusha, A. Shcheglov, D. Staroverov, T. Chepurnykh, A. Fradkov, S. Lukyanov und K. Lukyanov, Engineering of a monomeric green-to-red photoactivatable fluorescent protein induced by blue light, *Nature Biotechnology* **24** (2006)(4), 461–465.

[119] A. Lampe, V. Haucke, S. J. Sigrist, M. Heilemann und J. Schmoranzer, Multicolour direct STORM with red emitting carbocyanines, *Biology of the Cell* **104** (2012)(4), 229–237.

[120] C. A. Karatsuba, Fast evaluation of bessel functions, *Integral Transforms and Special Functions* **1** (1993)(4), 269–276.

[121] N. Bobroff, Position Measurement with a Resolution and Noise-Limited Instrument, *Review of Scientific Instruments* **57** (1986)(6), 1152–1157.

[122] A. Santos und I. T. Young, Model-Based Resolution: Applying the Theory in Quantitative Microscopy, *Appl. Opt.* **39** (2000)(17), 2948–2958.

[123] S. Wolter, M. Schuettpelz, M. Tscherepanow, S. Van de Linde, M. Heilemann und M. Sauer, Real-time computation of subdiffraction-resolution fluorescence images, *Journal of Microscopy-Oxford* **237** (2010)(1), 12–22.

[124] R. Henriques, M. Lelek, E. F. Fornasiero, F. Valtorta, C. Zimmer und M. M. Mhlanga, QuickPALM: 3D real-time photoactivation nanoscopy image processing in ImageJ, *Nat Meth* **7** (2010)(5), 339–340.

[125] W. S. Rasband, *ImageJ*, National Institutes of Health, Maryland, USA (http://www.macbiophotonics.ca/imagej/) (12.07.2010).

[126] J. Schleicher, *Image Processing for Super-Resolution Localization Microscopy Utilizing an FPGA Accelerator*, Diplomarbeit, University of Heidelberg (2011).

[127] F. Herrmannsdoerfer, *SimpleSTORM an Efficient Selfcalibrating Reconstruction Algorithm for Single and Multi-Channel Localization Microscopy*, Diplomarbeit, University of Heidelberg (2013).

[128] M. Gunkel, *Lokalisationsmikroskopie mit mehreren Farben und ihre Anwendung in biologischen Präparaten*, Dissertationsschrift, Universität Bielefeld (2011).

[129] M. Gunkel, B. Flottmann, M. Heilemann, J. Reymann und H. Erfle, Integrated and correlative high-throughput and super-resolution microscopy, *Histochemistry and Cell Biology* (2014), 1–7.

[130] N. Otsu, A threshold selection method from gray level histograms, *IEEE Trans. Systems, Man and Cybernetics* **9** (1979), 62–66, minimize inter class variance.

[131] D. G. Lowe, Distinctive Image Features from Scale-Invariant Keypoints, *International Journal of Computer Vision* **452** (2004), 352–355.

[132] H. Taekjip und P. Tinnefeld, Photophysics of Fluorescent Probes for Single-Molecule Biophysics and Super-Resolution Imaging, *Annual Review of Physical Chemistry* **63** (2012), 595–617.

[133] M. Heilemann, S. van de Linde, A. Mukherjee und M. Sauer, Super-Resolution Imaging with Small Organic Fluorophores, *Angewandte Chemie-International Edition* **48** (2009)(37), 6903–6908.

[134] S. Nanguneri, B. Flottmann, F. Herrmannsdoerfer, K. Thomas und M. Heilemann, Single-molecule super-resolution imaging by tryptophan-quenching-induced photoswitching of phalloidin-fluorophore conjugates, *Microscopy Research and Technique* **n/a** (2014), n/a–n/a.

[135] J. Brauers, N. Schulte und T. Aach, Multispectral Filter-Wheel Cameras: Geometric Distortion Model and Compensation Algorithms, *Image Processing, IEEE Transactions on* **17** (2008)(12), 2368–2380.

[136] J. R. Turner und A. M. Tartakoff, The response of the Golgi complex to microtubule alterations: the roles of metabolic energy and membrane traffic in Golgi complex organization., *The Journal of Cell Biology* **109** (1989)(5), 2081–2088.

[137] R. D. Klausner, J. G. Donaldson und J. Lippincott-Schwartz, Brefeldin A: insights into the control of membrane traffic and organelle structure., *The Journal of Cell Biology* **116** (1992)(5), 1071–1080.

[138] J. Lippincott-Schwartz, L. C. Yuan, J. S. Bonifacino und R. D. Klausner, Rapid redistribution of Golgi proteins into the {ER} in cells treated with brefeldin A: Evidence for membrane cycling from Golgi to {ER}, *Cell* **56** (1989)(5), 801 – 813.

[139] N. Nakamura, C. Rabouille, R. Watson, T. Nilsson, N. Hui, P. Slusarewicz, T. E. Kreis und G. Warren, Characterization of a cis-Golgi matrix protein, GM130., *The Journal of Cell Biology* **131** (1995)(6), 1715–1726.

[140] B. Huang, S. A. Jones, B. Brandenburg und X. Zhuang, Whole-cell 3D STORM reveals interactions between cellular structures with nanometer-scale resolution, *Nat Meth* **5** (2008)(12), 1047–1052.

[141] Y. Ben-Ari, Y. Brody, N. Kinor, A. Mor, T. Tsukamoto, D. L. Spector, R. H. Singer und Y. Shav-Tal, The life of an mRNA in space and time, *Journal of Cell Science* **123** (2010)(10), 1761–1774.

[142] N. Daigle und J. Ellenberg, [lambda]N-GFP: an RNA reporter system for live-cell imaging, *Nat Meth* **4** (2007)(8), 633–636.

[143] J. S. Paige, K. Y. Wu und S. R. Jaffrey, RNA Mimics of Green Fluorescent Protein, *Science* **333** (2011)(6042), 642–646.

[144] S. Dutta, B. Flottmann, M. Heilemann und A. Mokhir, Hybridization and reaction-based fluorogenic nucleic acid probes, *Chem. Commun.* **48** (2012), 9664–9666.

[145] D. Arian, E. Clo, K. V. Gothelf und A. Mokhir, A Nucleic Acid Dependent Chemical Photocatalysis in Live Human Cells, *Chemistry A European Journal* **16** (2010)(1), 288–295.

[146] D. Arian, L. Kovbasyuk und A. Mokhir, Control of the Photocatalytic Activity of Bimetallic Complexes of Pyropheophorbide-a by Nucleic Acids, *Inorganic Chemistry* **50** (2011)(23), 12010–12017.

[147] S. D. P. Baugh, Z. Yang, D. K. Leung, D. M. Wilson und R. Breslow, Cyclodextrin Dimers as Cleavable Carriers of Photodynamic Sensitizers, *Journal of the American Chemical Society* **123** (2001)(50), 12488–12494.

[148] A. Rotaru, J. Kovacs und A. Mokhir, Red light-activated phosphorothioate oligodeoxyribonucleotides, *Bioorganic & Medicinal Chemistry Letters* **18** (2008)(15), 4336 – 4338.

[149] A. Rotaru und A. Mokhir, Nucleic Acid Binders Activated by Light of Selectable Wavelength, *Angewandte Chemie International Edition* **46** (2007)(32), 6180–6183.

[150] O. Piestert, H. Barsch, V. Buschmann, T. Heinlein, J. P. Knemeyer, K. D. Weston und M. Sauer, A single-molecule sensitive DNA hairpin system based on intramolecular electron transfer, *Nano Letters* **3** (2003)(7), 979–982.

[151] D. Arian, L. Kovbasyuk und A. Mokhir, 1,9-Dialkoxyanthracene as a 1O2-Sensitive Linker, *Journal of the American Chemical Society* **133** (2011)(11), 3972–3980.

[152] S. Dutta, A. Fulop und A. Mokhir, Fluorogenic, Catalytic, Photochemical Reaction for Amplified Detection of Nucleic Acids, *Bioconjugate Chemistry* **24** (2013)(9), 1533–1542.

[153] S. van de Linde, S. Wolter, M. Heilemann und M. Sauer, The effect of photoswitching kinetics and labeling densities on super-resolution fluorescence imaging, *Journal of Biotechnology* **149** (2010)(4), 260 – 266.

Acknowledgements

At this point I take the opportunity to express my sincere gratitude to all the people that have contributed, supported and helped me with this thesis. Among these, I specifically want to mention:

- Prof. Dr. Mike Heilemann for giving me the opportunity to work on this PhD project here in Heidelberg. I very much appreciated his careful supervision of my work while at the same time giving me free rein in a lot of concerns. He taught me a lot about biophysics and scientific research in general.
- Prof. Dr. Andriy Mokhir for a wonderful and fruitful collaboration and his willingnes to be the first referee of this work.
- Apl. Prof. Dr. Dirk-Peter Herten for making himself available as second referee and for his interest in this work.
- the coordinator of the project on the integrated microscopy platform Dr. Holger Erfle, for his support of this work. I am very thankful, that he offered me a work place within his group at the BioQuant in Heidelberg.
- Dr. Manuel Gunkel for his help for this thesis and for proofreading numerous abstracts. Discussions with him helped me a lot to understand the subtleties of fluorescence microscopy in general.
- Jürgen Beneke, Nina Beil, Ruben Bulkescher and Dr. Jürgen Reymann for their diverse support, an endless supply of HeLa cells and the fascinating lunch-time discussions.
- Siddharth Nanguneri and Walter Muranyi for indispensible discussions and support, especially during the start-up period.
- Dr. Ullrich Köthe, Joachim Schleicher and Frank Herrmannsdörfer for their collaboration, the development of *SimpleSTORM* and *ColorComposer*, and for their excellent help in understanding the computer language.

- Dr. Vytaute Starkuviene and Dr. Tautvydas Lisauskas for their cooperation within the project on the integrated microscopy platform and their help in biological questions regarding the Golgi complex and the secretory pathway.
- the Group of Prof. Dr. Mike Heilemann in Frankfurt for their never-ending hospitality and informative discussions.
- Prof. Dr. Thomas Kuner his interest in the technique *d*STORM, for his cooperativeness and for giving me office space during the last year of my work.
- Barbara Werner for her help with all the bureaucracy while purchasing new equipment and travel expense accounting.
- My parents for their unconditioned support of all my projects.
- Anika for the wonderful time I have with you.

Eidesstattliche Versicherung gemäß § 8 der Promotionsordnung der Universität Heidelberg für die Philosophische Fakultät und die Neuphilologische Fakultät

1. Bei der eingereichten Dissertation zu dem Thema

____

____

____

handelt es sich um meine eigenständig erbrachte Leistung.

2. Ich habe nur die angegebenen Quellen und Hilfsmittel benutzt und mich keiner unzulässigen Hilfe Dritter bedient. Insbesondere habe ich wörtlich oder sinngemäß aus anderen Werken übernommene Inhalte als solche kenntlich gemacht.

3. Die Arbeit oder Teile davon habe ich wie folgt/bislang nicht[1] an einer Hochschule des In- oder Auslands als Bestandteil einer Prüfungs- oder Qualifikationsleistung vorgelegt

Titel der Arbeit:
Hochschule und Jahr:
Art der Prüfungs- oder Qualifikationsleistung:

4. Die Richtigkeit der vorstehenden Erklärungen bestätige ich.

5. Die Bedeutung der eidesstattlichen Versicherung und die strafrechtlichen Folgen einer unrichtigen oder unvollständigen eidesstattlichen Versicherung sind mir bekannt.

Ich versichere an Eides statt, dass ich nach bestem Wissen die reine Wahrheit erklärt und nichts verschwiegen habe.

________________ ____________________
Ort und Datum Unterschrift

---

[1] Nicht Zutreffendes streichen. Bei Bejahung sind anzugeben: der Titel der andernorts vorgelegten Arbeit, die Hochschule, das Jahr der Vorlage und die Art der Prüfungs- oder Qualifikationsleistung.